TRANSFORMATIONS AND DEEP INTRUSIONS OF PARTICLES AND PLANKTON IN THE GLOBAL OCEANS: WHICH PARTICLES SINK DEEPER AND WHY

by

Stephanie Hicks O'Daly

B.S. The University North Carolina Chapel Hill, 2014

M.S. University of Alaska Fairbanks, 2019

A Dissertation submitted in Partial Fulfillment of the Requirements

for the Degree of

Doctor of Philosophy

in

Oceanography

University of Alaska Fairbanks

August 2024

APPROVED:

Gwenn M. M. Hennon, Committee Chair

Thomas B. Kelly, Committee Member

Rainer Kiko, Committee Member

Andrew M.P. McDonnell, Committee Member

Franz Mueter, Committee Member

Suzanne L. Strom, Committee Member

Russell R. Hopcroft, Chair

Department of Oceanography

S. Bradley Moran, Dean

College of Fisheries and Ocean Sciences

Richard Collins, Director

Graduate School

Dedication

To the Inspiring Girls* Expeditions Community:

I am very grateful to the past, present, and future staff, instructors, participants, and the broader community of Inspiring Girls* Expeditions. Inspiring Girls* Expeditions works to empower cisgender girls and transgender, agender, Two Spirit, nonbinary, intersex, and genderqueer youth through science, art, and outdoor exploration. Working with this organization during my PhD has taught me so much and given a lot of meaning to my research. For more information or to support this amazing organization, visit www.inspiringgirls.org/.

Abstract

Sinking marine particles transport carbon from the ocean's surface to the deep ocean, thereby contributing to atmospheric carbon dioxide modulation and benthic food supply. Many studies have shown that particle size is not a good predictor of particle sinking speed or behavior. Thus, the overarching question of this dissertation: *why do certain particles sink faster or deeper than others, and is there a way to predict what depth a particle will reach in the ocean?* Multiple facets of the ocean's biological carbon pump are investigated using a combination of sediment traps, *in situ* particle imaging, and machine learning technology. In the Gulf of Alaska, we find aggregates contributed 61% to total carbon flux, suggesting that aggregation processes, not zooplankton repackaging, played a dominant role in carbon export. The role of the physical environment on the biological carbon pump was investigated in the Southern Ocean. Fluffy aggregates and grazers were most common at the surface during a phytoplankton bloom, whereas 1-3 months after a bloom, grazers are in the mesopelagic and feces and dense aggregates are in high abundance in the bathypelagic. These results shed light on how frontal structures in the Southern Ocean influence patterns of particle export and remineralization in the mesopelagic with implications for how this influences global biogeochemical cycles. Finally, the effect of biogeochemical province and carbonate saturation state was investigated in the tropical and subtropical North Atlantic and Pacific. We find that plankton distribution and marine particle morphology in the Atlantic Ocean are more strongly impacted by aragonite and calcite saturation state, despite much shallower saturation horizons in the Pacific. This research can help better predict how the strength of carbon storage in the ocean may change with climate change, which is critical for climate modelers to predict the effects of climate change more accurately.

Plain Word Summary

The deep ocean stores carbon away from the atmosphere, naturally modulating climate change. The main pathway for deep ocean carbon storage is sinking marine particles, such as aggregated phytoplankton material and zooplankton fecal pellets. The current paradigm is that bigger particles sink faster and contribute more to deep ocean carbon storage. However, some recent studies have shown that particle size does not predict particle sinking speed well. This leads to the overarching question of this dissertation: *why do certain particles sink faster or reach deeper depths than others, and can we predict what depth a particle will reach using these characteristics?* To look beyond particle size, we use cameras to image marine particles both in the ocean and on ships after collecting them from the ocean. In the Gulf of Alaska, most sinking carbon comes from phytoplankton aggregates, not fecal pellets, suggesting that zooplankton do not play a big role in carbon storage in the deep ocean. Secondly, in the Southern Ocean, we find that early in phytoplankton blooms, most marine particles are at the surface and are fluffy aggregates. One to three months after a phytoplankton bloom, there are lots of fecal pellets deep in the ocean, indicating that zooplankton play a major role in repackaging particles to faster sinking, denser fecal pellets. Finally, we find that the color and size of marine particles are more strongly impacted by low carbonate concentration in the Atlantic Ocean than in the Pacific, despite much lower carbonate concentrations. Low carbonate conditions will dissolve calcium carbonate shells, which some phytoplankton and zooplankton grow. This research can help us better predict how carbon storage in the ocean may be impacted by climate change, which could cause positive or negative feedback on climate change. This will help climate modelers better predict the effects of climate change.

Acknowledgments

I live, work, and recreate on the traditional and current unceded lands of the Lower Tanana Dena Peoples. The first chapter of this dissertation was conducted on the current and ancestral lands and waters of the Eyak and Sugpiaq-Alutiiq Peoples. I recognize and appreciate their past, present, and future stewardship of these lands and waters. I am learning to live in better relationships with these Indigenous Peoples and address the destructive impact of colonialism, particularly from the scientific community. One way I do this work is by supporting the First Alaskans Institute (https://www.firstalaskans.org/). I encourage others living or doing science in Alaska to participate in training and dialogues hosted by this institute and to support them financially as well.

I thank the chair of my graduate committee, Gwenn Hennon, for her mentorship, encouragement, creative ideas, and endless feedback. I also thank the members of my graduate committee, Tom Kelly, Rainer Kiko, Andrew McDonnell, Franz Mueter, and Suzanne Strom, for their mentorship, advice on data analysis, and perspectives from inside and outside the field of biogeochemistry. Thanks to Andrew McDonnell for accepting and funding me as his PhD student and supporting me after he transitioned to a full-time entrepreneur.

The National Science Foundation Career Grant, award number OCE-1654663, provided financial support for this research. This grant funded 10 semesters of research assistantships, most of my summer funding, and paid for the fieldwork and conference travel necessary to complete my degree. The first chapter of this dissertation was conducted with the Northern Gulf of Alaska Long-term Ecological Research program, National Science Foundation cooperative agreement #OCE-2322806 and #OCE-1656070. I acknowledge support from the Dissertation Completion Fellowship from the University of Alaska Fairbanks Graduate School for providing summer funding and tuition relief for the summer of 2024.

For my first chapter, I thank the Captain and crew of the R/V *Sikuliaq*, the science party on the 2019 Summer Northern Gulf of Alaska Long Term Ecological Research program (NGA-LTER) Process cruise, and Catherine Fuller, NOAA Teacher at Sea, for assistance with sample collection. I also thank Colleen Durkin for discussing polyacrylamide gel image analyses. This effort was funded by NSF Northern Gulf of Alaska-LTER grant number 1656070 and NSF CAREER Award grant number 1654663.

For my second chapter, I thank the Captain and crew of the R/V *Palmer* and the science party on the 2018 S04P GO-SHIP cruise and the Captain and crew of the R/V *Thompson* and the science party on the 2019 I06S GO-SHIP cruise. Funding for this effort was provided by NSF CAREER Award grant number 1654663.

For my third chapter, I thank the Captain and crew of the R/V *Thompson* and the science party on the 2021 A22 GO-SHIP cruise and the Captain and crew of the R/V *Revelle* and the science party on the 2022 P02 Leg 1 and Leg 2 GO-SHIP cruises. Funding for this effort was provided by NSF CAREER Award grant number 1654663.

Lastly, I would like to thank my parents, grandparents, and sister for supporting me from across the country. Many thanks to Tait, Kenya, and Meeko for providing emotional support and encouragement in our Alaskan home. Lots of love to my old and new friends in Fairbanks and worldwide.

Table of Contents

List of Figures

List of Tables

Chapter 1: General Introduction

The biological carbon pump facilitates the storage of part of the carbon fixed through photosynthesis in the euphotic zone into the deep ocean or seafloor sediments, modulating the global carbon cycle. The biological carbon pump can be broken down into the gravitational particle pump, where particulate organic carbon sinks through the water as portions are consumed by bacteria and zooplankton, physical mixing pumps where carbon is mixed to deeper depths either through eddy subduction or deepening of the mixed layer, as well as active particle pumps associated with the daily migration of zooplankton and fish (Boyd et al., 2019). The depth at which particulate organic carbon is remineralized in the water column significantly controls the carbon dioxide concentration in the atmosphere (Kwon et al., 2009). So, if particulate organic carbon can reach deeper depths in the oceans, this will result in lower atmospheric carbon dioxide concentrations. Therefore, accurately parameterizing processes within the ocean's biological carbon pump is increasingly important as atmospheric carbon dioxide concentration rises. The uncertainty of ocean carbon sequestration due to the biological carbon pump represents an estimated $0.5 trillion of climate damage (Jin et al., 2020). More research is needed to quantify the strength and efficiency of the gravitational and active particle pumps that make up the biological carbon pump in the ocean.

Two aspects of the biological carbon pump that are better described are primary production rates and particulate organic carbon flux rates (i.e., the gravitational particle pump). Process studies such as carbon-13-based primary productivity measurements and carbon flux measured through inline drifting sediment traps have been used for a long time in many geographical locations to measure carbon fixation at the surface of the ocean, carbon export out of the euphotic zone, and POC flux attenuation (Buesseler et al., 2020; Buesseler & Boyd, 2009; Martin et al., 1987; Moran et al., 2012). However, these methods typically only measure bulk processes of particulate organic carbon production and flux, while phytoplankton and zooplankton taxa-specific interactions cannot be tracked. Tools involving particle imaging have been developed to shed more light on potential taxa-specific interactions.

The Underwater Vision Profiler (UVP5) was developed to image the particle structure in situ over a wide range of particle sizes (100 μm to 2.5 cm). This instrument is integrated with the CTD Rosette and does not add to wire time or water budgets. This instrument measures the size and abundance of particles such as marine snow aggregates, phytoplankton, zooplankton, and

fecal pellets that are within the sampling size range (Picheral et al., 2010). It measures undisturbed water during the CTD downcast, unlike other imaging systems such as Flocam that requires water to be collected and then dispensed from a Niskin bottle before being passed through the instrument to be imaged. The UVP samples full-depth profiles. In addition to particle data, the UVP saves a greyscale JPEG image of particles larger than 500 µm. These images can be used to identify particle types through Ecotaxa (Picheral et al., 2017).

Increased sampling with new technologies like the UVP has been identified as an important area to expand in partnering with large-scale oceanographic sampling efforts like the U.S. Global Ocean Ship-based Hydrographic Investigations Program (GO-SHIP) (Lombard et al., 2019; Sloyan et al., 2019). This program, along with the former Repeat Hydrography and WOCE programs, has been sampling ocean-basin-wide transects all over the global oceans, repeating transects about every 10 years. It is through these programs that we have gained insights and tracked changes in the global thermohaline circulation (Wunsch & Ganachaud, 2000), ocean acidification, and anthropogenic carbon uptake (Gruber et al., 2019), deoxygenation of the ocean (Hahn et al., 2017), and persistent deep nepheloid layers (Gardner et al., 2018). More targeted sampling of the biological carbon pump at this scale can help us understand the magnitude of and changes in carbon storage at depth in the ocean. Additionally, it can help us identify and quantify specific mechanisms that control carbon storage at depth in the ocean.

Another relatively recent development in particle imaging is using polyacrylamide gels in sediment traps to identify sinking particle size distribution and type (Durkin et al., 2015, 2021; Ebersbach & Trull, 2008; McDonnell & Buesseler, 2010). In bulk collection sediment traps, particles are disturbed from their sinking state when they reach the bottom of the trap. Sometimes, these bulk-collected particles are imaged or identified, but the in-situ condition of the particle cannot be determined. Polyacrylamide gels have been used in sediment traps to preserve the sinking particles. These gels can then be imaged and segmented to determine the sinking particle size structure. More recently, the segmented images are being saved as individual images of particles, where machine learning software can be used to predict particle type.

In this dissertation, I present the results from three regional analyses, one in the Northern Gulf of Alaska, one in the Southern Ocean, and a comparative analysis between the subtropical and tropical North Atlantic and North Pacific. These analyses each investigate the strength,

efficiency, and control mechanisms of the biological carbon pump in the oceans utilizing a combination of bulk chemical measurements and imaging techniques. Details on these three studies are discussed in the following chapters of this dissertation.

1.1 References

Boyd, P. W., Claustre, H., Levy, M., Siegel, D. A., & Weber, T. (2019) Multi-faceted particle pumps drive carbon sequestration in the ocean. *Nature*. 568(7752), 327–335. https://doi.org/10.1038/s41586-019-1098-2

Buesseler, K. O., & Boyd, P. W. (2009) Shedding light on processes that control particle export and flux attenuation in the twilight zone of the open ocean. *Limnology and Oceanography*, 54(4), 1210–1232. https://doi.org/10.4319/lo.2009.54.4.1210

Buesseler, K. O., Boyd, P. W., Black, E. E., & Siegel, D. A. (2020) Metrics that matter for assessing the ocean biological carbon pump. *Proceedings of the National Academy of Sciences of the United States of America*. 117(18), 9679–9687. https://doi.org/10.1073/pnas.1918114117

Durkin, C. A., Estapa, M. L., & Buesseler, K. O. (2015) Observations of carbon export by small sinking particles in the upper mesopelagic. *Marine Chemistry*. 175, 72–81. https://doi.org/10.1016/j.marchem.2015.02.011

Durkin, C. A., Buesseler, K. O., Cetinić, I., Estapa, M. L., Kelly, R. P., & Omand, M. (2021) A visual tour of carbon export by sinking particles. *Global Biogeochemical Cycles*. 35(10), 1–17. https://doi.org/10.1029/2021GB006985

Ebersbach, F., & Trull, T. W. (2008) Sinking particle properties from polyacrylamide gels during the KErguelen Ocean and Plateau compared Study (KEOPS): Zooplankton control of carbon export in an area of persistent natural iron inputs in the Southern Ocean. *Limnology and Oceanography*. 53(1), 212–224. https://doi.org/10.4319/lo.2008.53.1.0212

Gardner, W. D., Mishonov, A. V., & Richardson, M. J. (2018) Decadal comparisons of particulate matter in repeat transects in the Atlantic, Pacific, and Indian Ocean Basins. *Geophysical Research Letters, 45*(1), 277–286. https://doi.org/10.1002/2017GL076571

Gruber, N., Clement, D., Carter, B. R., Feely, R. A., van Heuven, S., Hoppema, M., Ishii, M. Key, R. M., Kozyr, A., Lauvset, S. K., Monaco, C. L., Mathis, J. T., Murata, A., Olsen,

A., Perez, F. F., Sabine, C. L., Tanhua, T., Wanninkhof, R. (2019). The oceanic sink for anthropogenic CO_2 from 1994 to 2007. *Science*. 363(6432), 1193–1199. https://doi.org/10.1126/science.aau5153

Hahn, J., Brandt, P., Schmidtko, S., & Krahmann, G. (2017) Decadal oxygen change in the eastern tropical North Atlantic. *Ocean Science*. 13(4), 551–576. https://doi.org/10.5194/os-13-551-2017

Jin, D., Hoagland, P., & Buesseler, K. O. (2020) The value of scientific research on the ocean's biological carbon pump. *Science of the Total Environment*. 749, 141357. https://doi.org/10.1016/j.scitotenv.2020.141357

Kwon, E. Y., Primeau, F., & Sarmiento, J. L. (2009) The impact of remineralization depth on the air–sea carbon balance. *Nature Geoscience*. 2(9), 630–635. https://doi.org/10.1038/ngeo612

Lombard, F., Boss, E., Waite, A. M., Uitz, J., Stemmann, L., Sosik, H. M., Schultz, J., Romagnan, J. B., Picheral, M., Pearlman, J., Ohman, M. D., Niehoff, B., Möller, K. O., Miloslavich, P., Lara-Lpez, A., Kudela, R., Lopes, R. M., Kiko, R., Karp-Boss, L., Jaffe, J. S., Iversen, M. H., Irisson, J. O., Fennel, K., Hauss, H., Guidi, L., Gorsky, G., Giering, S. L. C., Gaube, P., Gallager, S., Dubelaar, G., Cowen, R. K., Carlotti, F., Briseño-Avena, C., Berline, L., Benoit-Bird, K., Bax, N., Batten, S., Ayata, S. D., Artigas, L. F., & Appeltans, W. (2019) Globally consistent quantitative observations of planktonic ecosystems. *Frontiers in Marine Science*. 6(196), 1-21. Https://doi.org/10.3389/fmars.2019.00196

Martin, J. H., Knauer, G. A., Karl, D. M., & Broenkow, W. W. (1987) VERTEX: carbon cycling in the northeast Pacific. *Deep-Sea Research, 34*(2), 267–285.

McDonnell, A. M. P., & Buesseler, K. O. (2010) Variability in the average sinking velocity of marine particles. *Limnology and Oceanography*. 55(5), 2085–2096. https://doi.org/10.4319/lo.2010.55.5.2085

Moran, S. B., Kelly, R. P., Iken, K., Mathis, J. T., Lomas, M. W., & Gradinger, R. (2012) Seasonal succession of net primary productivity, particulate organic carbon export, and autotrophic community composition in the eastern Bering Sea. *Deep Sea Research Part II: Topical Studies in Oceanography*. 65–70, 84–97. https://doi.org/10.1016/j.dsr2.2012.02.011

Picheral, M., Colin, S., & Irisson, J. (2017) EcoTaxa, a tool for the taxonomic classification of images. Retrieved from http://ecotaxa.obs-vlfr.fr

Picheral, M., Guidi, L., Stemmann, L., Karl, D. M., Iddaoud, G., & Gorsky, G. (2010) The underwater vision profiler 5: An advanced instrument for high spatial resolution studies of particle size spectra and zooplankton. *Limnology and Oceanography: Methods*. 8, 462–473. https://doi.org/10.4319/lom.2010.8.462

Sloyan, B. M., Wanninkhof, R., Kramp, M., Johnson, G. C., Talley, L., Tanhua, T., McDonagh, E., Cusack, C., O'Rourke, E. A., McGovern, E., Katsumata, K., Diggs, S., Hummon, J., Ishii, M., Azetsu-Scott, K., Boss, E., Ansorge, I., Pérez, F. F., Mercier, H., Williams, M., Anderson, L., Lee, J. H., Murata, A., Kouketsu, S. (2019) The global ocean ship-base hydrographic investigations program (GO-SHIP): A platform for integrated multidisciplinary ocean science. *Frontiers in Marine Science*. 6, 1–21. https://doi.org/10.3389/fmars.2019.00445

Wunsch, C., & Ganachaud, A. (2000) Improved estimates of global ocean circulation, heat transport and mixing from hydrographic data. *Nature*. 408, 453–456.

Chapter 2: Strong and efficient summertime carbon export driven by aggregation processes in a subarctic coastal ecosystem

2.1 Abstract

Sinking marine particles, one pathway of the biological carbon pump, transport carbon to the deep ocean from the surface, thereby modulating atmospheric carbon dioxide and supplying benthic food. Few in-situ measurements exist of sinking particles in the Northern Gulf of Alaska; therefore, regional carbon flux prediction is poorly constrained. In this study, we (1) characterize the strength and efficiency of the biological carbon pump and (2) identify drivers of carbon flux in the Northern Gulf of Alaska. We deployed up to five inline drifting sediment traps in the upper 150 m to simultaneously collect bulk carbon and intact sinking particles in polyacrylamide gels and measured net primary productivity from deck-board incubations during the summer of 2019. We found high carbon flux magnitude, low attenuation with depth, and high export efficiency. We quantified carbon flux for ten particle types, including various fecal pellet categories, dense detritus, and aggregates using polyacrylamide gels. The contribution of aggregates to total carbon flux (41 - 93%) and variability of total carbon flux from aggregate carbon flux (95%) suggest that aggregation processes, not zooplankton repackaging, played a dominant role in carbon export. Furthermore, export efficiency correlated significantly with the proportion of chlorophyll-A in the large size fraction (> 20 μm), total aggregate carbon flux, and contribution of aggregates to total carbon flux. These results suggest that this stratified, small-cell-dominated ecosystem can have sufficient aggregation to allow for a strong and efficient biological carbon pump. This is the first integrative description of the biological carbon pump in this region.

2.2 Introduction

Gravitationally sinking marine particles transport photosynthetically fixed carbon from the euphotic zone to the ocean's interior and benthos. Such flux is an important biological carbon pump component, contributing to the global carbon cycle (Kwon et al. 2009; Le Moigne 2019). Despite many decades of studies, there are large uncertainties in our understanding of the biological carbon pump due partly to large temporal and spatial heterogeneity in export flux (Buesseler et al. 2007; Henson et al. 2011; Laufkötter et al. 2016; Kelly et al. 2018). While global biological carbon pump estimates vary by nearly 50%, ranging between 7 – 16 Pg C $year^{-1}$

(Dunne et al. 2007; Henson et al. 2012; Laufkötter et al. 2016), regional estimates under a changing climate are often even more uncertain. For example, under warming ocean conditions some models predict more efficient carbon export in high-latitude regions (Weber et al. 2016), such as the Northern Gulf of Alaska, while others predict less efficient carbon export (Henson et al. 2012; Marsay et al. 2015).

The composition of sinking marine particles affects the overall net carbon flux (Turner 2015); therefore, accurately parameterizing rates based on this composition is an important way to improve climate model accuracy (Siegel et al. 2014; Laufkötter et al. 2016). Sinking marine particles can be broadly organized into three functional types: (1) phytoplankton cells, (2) zooplankton fecal pellets, and (3) aggregates of detrital material (Turner 2015). These different types of particles overlap in size, but exist in distinct ranges in composition, density, shape, porosity, and ecological sources (Alldredge 1998; Buesseler et al. 2007; Iversen and Ploug 2010; Turner 2015). These distinctive properties result in different sinking speeds (Armstrong et al. 2002; De La Rocha and Passow 2007; Iversen and Lampitt 2020) and remineralization rates (Ploug et al. 2008b; Kobari et al. 2013). Marine particle size has been used to calculate carbon content and to predict sinking speed (Stemmann et al. 2004; Guidi et al. 2008); however, considering only particle size masks potential differences in export among particle types. Understanding the role of particle type in addition to size will help reduce uncertainty in the ocean's biological carbon pump.

In contrast to the biological carbon pump, primary productivity and phytoplankton community composition have been well studied in the northern Gulf of Alaska. Summers are often characterized by a nutrient-limited community of small-celled nanoflagellates and picoplankton (Strom et al. 2006). Stations closer to the coast are often nitrogen-limited while stations on the slope are likely iron-limited (Aguilar-Islas et al. 2016). This results in moderate summertime primary productivity rates, similar to other nutrient-limited regions. In contrast, the springtime community is typically characterized by large diatoms and high rates of primary productivity (Strom et al. 2016). Based on the dominance of small phytoplankton cells, high rates of microzooplankton grazing (Strom et al. 2001, 2007) and high macrozooplankton biomasses (Moriarty et al. 2013), we would expect a weak and inefficient summertime biological carbon pump with sinking material dominated by zooplankton fecal pellets. Indeed, relatively

large contributions of fecal pellets have been measured in the Southern Ocean, another high-latitude system (Ebersbach and Trull 2008; Laurenceau-Cornec et al. 2015).

As a part of the Northern Gulf of Alaska Long Term Ecological Research program, we used PIT-style (Knauer et al. 1979) sediment traps to measure the quantity and quality of sinking particles in the Northern Gulf of Alaska during June and July 2019, along with corresponding measurements of euphotic zone primary production. Additionally, we estimated the contribution of phytoplankton cells, aggregates, and fecal pellets to overall carbon flux using polyacrylamide gel traps. This study characterizes the strength and efficiency of the biological carbon pump across the Northern Gulf of Alaska and the potential drivers of these patterns. This study sets a baseline for the biological carbon pump in the Northern Gulf of Alaska, as these are the first measurements of carbon export in this region of which we are aware, and contributes to our understanding of the broader coastal subarctic.

2.3 Methods

2.3.1 Study Area and Hydrography

The Northern Gulf of Alaska is a productive, high-latitude, coastal ecosystem characterized by a cyclonic sub-Arctic gyre. Prevailing winds from the Aleutian Low and freshwater inputs seasonally force downwelling over the shelf (Royer and Emery 1987) and promote upwelling off the shelf within the Gulf of Alaska sub-Arctic gyre (Muench et al. 1978; Macklin et al. 1990; Ladd et al. 2016). The eastern boundary of this gyre is the slower and wider Alaska Current which turns into the narrower and faster Alaskan Stream near Kodiak Island (Danielson et al. 2022). The Alaska Coastal Current is driven by winds and freshwater inputs and forms a very fast current that hugs the Alaskan coastline on the shelf also in a cyclonic direction (Reed and Schumacher 1986). The upwelling gyre replenishes macronutrients to the surface waters offshore, resulting in high nutrient/low chlorophyll (HNLC) waters that are typically iron-limited (Aguilar-Islas et al. 2016). The Alaska Coastal Current waters have seasonally high iron inputs from glacial runoff; in summer and fall, primary producers are typically macronutrient-limited due to strong stratification from freshwater input and warming. A shelf break front can form in the vicinity of the 300-m isobath, promoting vertical transport of deeper nutrient-rich waters to the surface (Figure 2.1) (Aguilar-Islas et al. 2016; Strom and Fredrickson 2020). As such, productivity can be high along the shelf break where onshore and offshore waters meet (Parsons 1987; Stabeno et al. 2004; Jaeger and Nittrouer 2006). The shelf surrounding Kodiak Island has

banks that are shallow enough that tidal energy can mix bottom water to the surface, providing nutrients and breaking down stratification (Mordy et al. 2019), which leads to higher summertime production. As a high-latitude system, the Northern Gulf of Alaska is known for high seasonal and interannual variability in chlorophyll and primary production (Waite and Mueter 2013; Strom et al. 2016), often experiencing a strong spring bloom of large-celled phytoplankton (e.g., diatoms) and a smaller magnitude fall bloom (Sambrotto and Lorenzen 1987; Napp et al. 1996). Summers are characterized by stratification due to solar radiation and freshwater input resulting in low- to moderate productivity dominated by pico- and nano-phytoplankton (Childers et al. 2005; Weingartner et al. 2005).

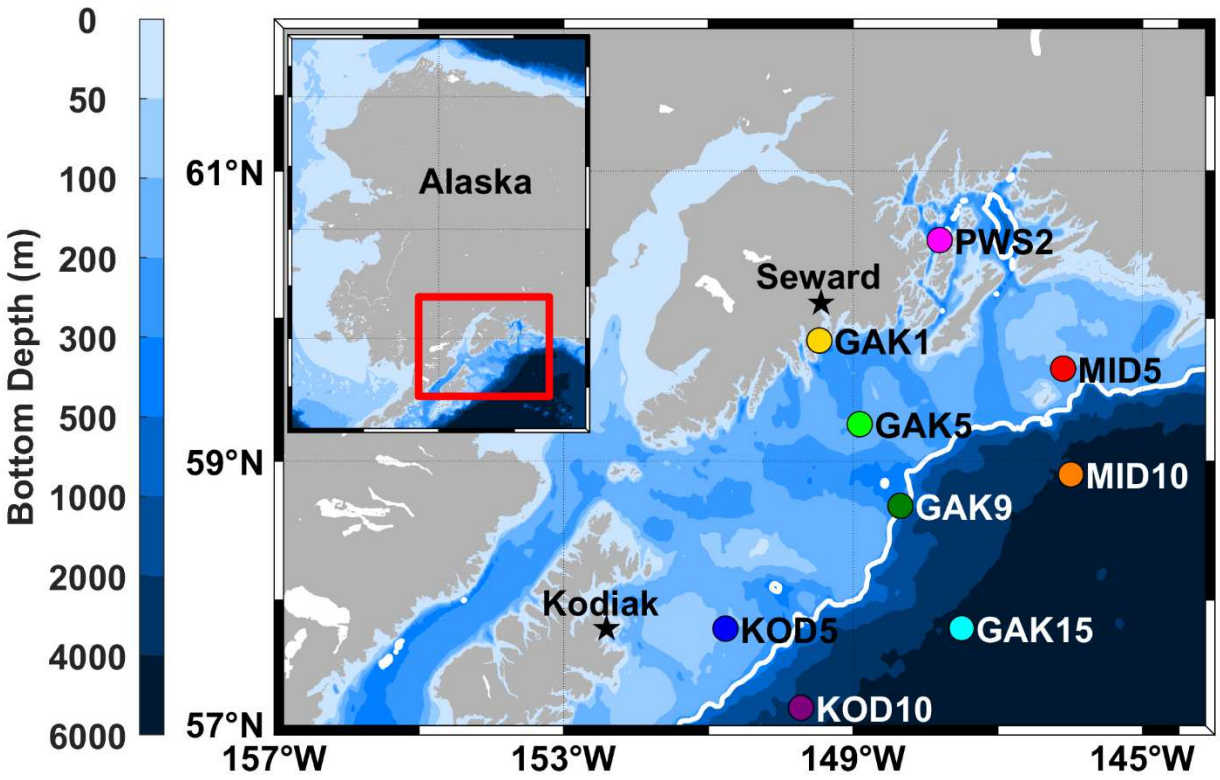

Figure 2.1: Locations of process stations where drifting sediment traps were deployed and net primary productivity (NPP) rates were measured (colored circles). The 300 m isobath, which separates the continental shelf from slope, is shown in white. These stations largely fall on three transect lines, Kodiak Line (KOD), Gulf of Alaska Line (GAK), and Middleton Island Line (MID), as well as a single station in Prince William Sound (PWS).

Data from this study were collected as part of the Northern Gulf of Alaska Long Term Ecological Research program during the SKQ2019-15S cruise from June 30 until July 17 of 2019 on the R/V Sikuliaq. Three transects were sampled including the Gulf of Alaska line

(GAK), the Kodiak Island line (KOD), and the Middleton Island line (MID), as well as stations in Prince William Sound (PWS) (Figure 2.1, Table 2.1). Shelf station GAK1 is located near shore and within the Alaska Coastal Current. The rest of the shelf stations (GAK5, MID5, and KOD5) and the shelf break station (GAK9) are not located in a major current, although they may experience advective processes due to mesoscale eddies and episodic wind events. MID10, GAK15, and KOD10 are slope stations located within the Alaska Current/Alaska Stream. PWS2 is located within Prince William Sound and is categorized as a sound station.

Table 2.1: Location, duration, and depth of drifting sediment trap deployments in the Northern Gulf of Alaska.

Station	Category	Seafloor depth (m)	Depth of traps (m)	Deploy time (UTC)	Deloy latitude	Deploy longitude	Duration (h)
GAK1	Shelf	269	27, 53, 78, 103, 128	7/13/19 13:00	59.829	-149.453	7.8
GAK5	Shelf	173	27, 53, 78, 103	7/12/19 12:47	59.245	-148.898	8.5
GAK9	Shelf	270	27, 53, 78, 103, 128	7/10/19 14:07	58.662	-148.342	17.0
GAK15	Slope	4400	27, 53, 78, 103, 128	7/9/19 6:32	57.780	-147.476	18.4
KOD5	Shelf	86	27, 53	7/15/19 14:58	57.780	-150.760	6.3
KOD10	Slope	2501	27, 53, 78, 103, 128	7/17/19 0:21	57.203	-149.721	15.5
MID5	Shelf	93	25, 50	7/2/19 7:31	59.65	-146.095	14.7
MID10	Slope	4464	25, 50, 75, 100, 125	7/3/19 13:26	58.909	-145.997	7.9
PWS2	Sound	731	80, 105, 130, 155	6/30/19 17:31	60.554	-147.793	10.1

Sediment trap, 13C net primary productivity (NPP), and CTD data from this study come from intensive stations (Figure 2.1). The CTD unit consisted of a Seabird SBE16plus unit coupled with a WetLabs fluorometer and transmissometer. An Underwater Vision Profiler 5 Standard Definition (UVP5; Hydroptic) unit was mounted to the frame, measured in situ particles from 102 μm to 26 mm, and was deployed with every CTD cast.

2.3.2 Sediment Trap Sampling and Analysis

Lagrangian surface-tethered drifting sediment traps (PITs; KC Denmark model number 28.2000) were deployed to collect sinking particles (Moran et al. 2012; O'Daly et al. 2020). Nine stations were sampled with durations between 6 - 19 h (median: ~10 h) depending on other cruise operations (Table 2.1). The shallowest crossframe was deployed at approximately 27 m, our best estimate of the base of the euphotic zone (1% light level) in this region during the summer based on previous observations, with each subsequent crossframe tethered in 25 m increments. We sampled between two and five depths depending on the local bathymetry at each deployment (Table 2.1). The deepest trap for each deployment was positioned at least 20 m above the seafloor to reduce the impacts of benthic resuspension. The depth of the euphotic zone during this cruise averaged 28 m. For export flux estimates, we selected the trap that was closest in depth to the base of the euphotic zone (± 9 m) or the trap immediately below the euphotic zone. All mixed layer depths, as identified by a density offset of 0.125 kg m^{-3} (Williams et al. 2006), were less than 20 m, consistent with summer conditions in this region (Sarkar et al. 2005). As such, all traps at each station were deployed below the mixed layer.

Each inline crossframe consisted of four tubes on beveled hinges. Two of the four tubes collected sinking particles in bulk and were partially filled with filtered seawater brine (i.e., 0.22 μm + NaCl, salinity > 50) that was poisoned (i.e., 1% formalin, final concentration, buffered to saturation with borax) and chilled (4˚C). The remaining two tubes in each trap array had a removable clear-bottomed cup filled with clear viscous polyacrylamide gel (50 mL). The cups were fitted with a thin sloping ramp, which created a seal on the inside of the tube walls and funneled sinking particles into the cup. All four tubes were then filled carefully to the top with chilled (4˚C) and filtered (0.22 μm millipore sterivex filter cartridges) seawater.

We measured sinking particulate organic carbon (POC) from the bulk trap material as follows. After recovery, each trap tube was covered and left to rest for about two hours until all sinking particles reached the bottom, then overlying water was removed from all tubes down to a

boundary layer of the brine for the bulk tubes or as close to the surface of the gel as possible without disturbing the gel. Gel cups were removed, covered, and stored in the dark until they could be imaged, which occurred < 6 h after recovering the drifting sediment trap (see "Gel trap imaging and image processing" for more details). Sinking particles in the two bulk collection tubes at each depth were quantitatively split into 10 subsamples each using a McLane rotary splitter. All subsamples were passed through a 500 μm mesh to remove swimmers (Owens et al. 2013; Baker et al. 2020). Three subsamples were combined for POC and filtered onto precombusted, preweighed 25-mm Whatman GF/F filters. All filters were dried in a dehydrator at 60°C for 12 h and sealed in Petri dishes until further analysis. This resulted in two POC flux values per trap depth (i.e., one per bulk collection tube).

Carbon samples were processed in the Alaska Stable Isotope Facility at the University of Alaska Fairbanks Water and Environmental Research Center according to O'Daly et al. (2020). POC/PN filters were acidified with 10% hydrochloric acid for 24 h (fumigation method) to remove inorganic carbon. All sample filters were pelletized in tin cups and processed by CHN elemental analyzer. POC values were converted to daily fluxes (i.e., g C m^{-2} d^{-1}) based on deployment duration and trap area.

An average chemically derived POC flux error (found to be 14%) was calculated as the average normalized variation from the mean of duplicate samples at each depth (Appendix A). Chemically derived POC flux attenuation was calculated using a power-law function shown in Equation 2.1 (Buesseler et al. 2007)

$$\frac{\mathrm{F}}{F_0} = \left(\frac{z}{z_0}\right)^{-b} \tag{2.1}$$

where z is the depth of the trap and z0 is the depth of the shallowest trap (m for both), F is the flux at depth z, F_0 is the flux at the shallowest trap depth, and b is a unitless exponent that is the best-fit attenuation coefficient. The attenuation coefficient, b, was found by fitting Equation 1 and minimizing the sum of squared residuals between measured and modeled POC flux using fminsearch in Matlab 2019B.

2.3.3 Net Primary Productivity Rate and Chlorophyll-*a* Measurements

Rates of NPP were measured at 6 depths spanning the euphotic zone using 24 h on-deck incubations (Hama et al. 1983). Water was collected by Niskin rosette, spiked with $H^{13}CO_3^-$ and incubated in screened bags corresponding to in situ temperature and collection irradiance (range

100 to 1% of surface irradiance as estimated from the PAR attenuation coefficient determined during the downcast). After 24 h, each incubation was filtered onto pre-combusted GF/F filters and frozen at -80°C. Back in the lab, samples were acidified (fumed) with 10% hydrochloric acid for 24 h to remove PIC, pelletized, and sent to the UC Davis Stable Isotope Facility for determination of carbon content and 13C isotopic abundance. Rates were integrated over the depth of the euphotic zone to determine integrated NPP (i.e., mg C m^{-2} d^{-1}). Total integrated and size-fractionated chlorophyll-a (chlA) was measured as in Strom et al. (2016) and integrated to 75 m, which has been shown to include the bulk of the chlorophyll in the water column in this region during all seasons.

2.3.4 Gel Trap Imaging and Image Processing

Polyacrylamide gels containing intact sinking particles were imaged in darkfield illumination with oblique lighting from multiple angles according to O'Daly et al. (2020). A ruler positioned at the same height as the surface of the gel was imaged using the same settings for each gel to calculate pixels per centimeter for each imaged gel. Gel images were cropped to remove lighting artifacts and jar edges before being processed to detect particles according to Durkin et al. (Durkin et al. 2021) with a few modifications (Figure 2.2, panel A). Image processing methods were modified to better select particles and minimize false-positive selections. Background determination followed the regional maxima method using the *skimage.morphology.reconstruction* function in Python to create a background image, which was subtracted from the original image. Edge detection was used before thresholding to identify and label in-focus particle edges. In the brightness threshold step, the triangle method was used to select the best thresholding value for each image, rather than a fixed thresholding value, by using the *skimage.filters.threshold_triangle* function. Binary processed images were saved as JPEGs (Figure 2.2, panel B) and loaded into Adobe Photoshop CS6 for manual validation. Particles that were incorrectly segmented were manually corrected. The image was then saved and reloaded into the Python routine. A one-pixel erosion step was added before identifying and matching in-focus particle edges to remove a halo effect around particles. Finally, particles were counted and measured (Figure 2.2, panel C). Calculating particle fluxes in units of # m^{-2} d^{-1} occurred by grouping particles by their equivalent spherical diameter (ESD) into logarithmically spaced size

bins with edges at $\left(2^{\frac{k}{3}}\right)|_{k=10}^{43}$ µm (Durkin et al. 2021). Uncertainty was calculated assuming a Poisson distribution in particle counts.

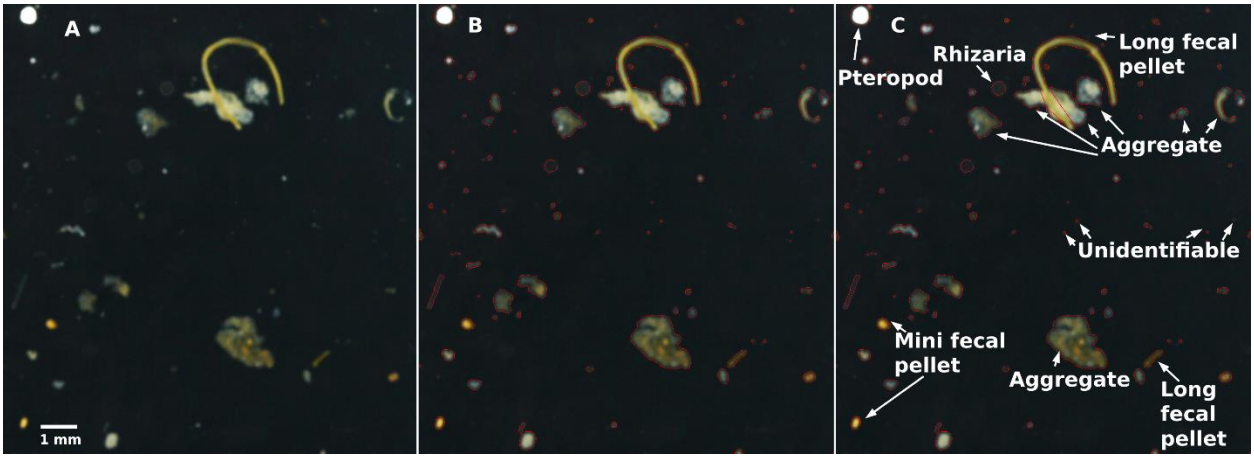

Figure 2.2: Particle segmentation and identification. (A) Sinking particle in polyacrylamide gel imaging, (B) automatic segmentation, (C) manual correction to segmentation, and classification. Particles identified as pteropods and other living zooplankton except for rhizaria were removed from carbon calculation. Image enhanced for clarity.

2.3.5 Gel Trap Carbon Content by Particle Type

Particles were categorized into ten different particle types (Figure 2.2, panel C): aggregates, dense detritus, long fecal pellet, large loose fecal pellet, short fecal pellet, salp fecal pellet, mini fecal pellet, rhizaria, phytoplankton, and unidentifiable as in Durkin et al. (Durkin et al. 2021). Rhizaria were included in the carbon flux modeling because most rhizaria can be considered part of the gravitational flux (Bernstein et al. 1987; Michaels et al. 1995; Lampitt et al. 2009). All mesozooplankton were identified in images but removed from consideration when modeling carbon flux from the identified particles because they were assumed not to be part of the gravitational sinking flux. Particles manually identified from GAK15 were used as a training set in a model to predict the type of the remaining particles using high-level Keras preprocessing utilities from the Tensorflow package in Python to speed up the manual validation of all particles. Identification becomes more challenging as particle size decreases. More than 90% of particles smaller than 100 µm were unidentifiable while only ~23% of particles larger than 100 µm were unidentifiable.

We calculated the carbon content for each particle type using a hybrid of inverse modeling and published values depending on particle type. Particle volume was calculated from ESD using

type-specific ESD to volume relationships (Appendix A) (Durkin et al. 2021). Then particle volumes were converted to carbon using Equation 2.2 where C is the calculated carbon content per particle (mg C), A is a scaling coefficient (mg C μm^{-3}), V is the calculated particle volume (μm^3), and B is a unitless exponent parameter.

$$C = A \times V^B \tag{2.2}$$

Aggregates and unidentifiable particles were assumed to have the same A (A_{agg}) and B (0.8) values (Menden-Deuer and Lessard 2000; Durkin et al. 2021). Dense detritus, large loose fecal pellets, long fecal pellets, short fecal pellets, and mini fecal pellets were assumed to have the same A value (A¬FP) and a B value of 1 (Wilson et al. 2008; Durkin et al. 2021). Ideally, each particle type would be fit with an individual particle-type specific scaling coefficient, A, and exponent parameter, B, in the model. However, there was not enough data to accurately constrain the model with the increased degrees of freedom, which decreased the overall model certainty. Therefore, we combined particle types to share a scaling coefficient and exponent parameter that we believed would have similar carbon content per unit volume. We grouped unidentifiable particles with aggregates because unidentifiable particles are most likely to be small aggregates. After all, fecal pellets have a biological creation mechanism that prevents them from being infinitely small (likely having a right-skewed relationship with ESD), whereas aggregates are created physically and therefore are more likely to have a log-linear relationship with ESD. Additionally, unidentifiable particles are unlikely to substantially influence the overall carbon distributions by type regardless of the scaling coefficients used because they make up a small percentage of total particle volume (0.5 – 37.5%, averaging 6.4%). Using the same A and B values as aggregates, these values were scaled slightly up when converted to units of carbon where the total percent unidentified carbon flux ranged from 2 – 27% and averaged 8%. Additionally, we grouped all the fecal pellets with dense detritus, as has been done in previous studies (Durkin et al., 2021). Dense detritus would have different scaling coefficients than aggregates because they are more tightly packed than aggregates. Again, this choice likely had little outcome on the overall carbon distributions by type because dense detritus made up a small percentage of the total particle volume (0 – 6.4%, averaging 1.1%). In future studies, having more bulk chemical carbon flux and gel-estimated carbon flux pairs would allow for more individualized scaling values for more particle types.

B values less than one are consistent with less efficient packaging of larger particles (Alldredge 1998). This pattern is more pronounced for aggregates and unidentifiable particles than fecal pellets since aggregate formation allows for large, loosely-packed particles (Johnson et al. 1996) while fecal pellets exhibit a more uniform carbon density (Bishop et al. 1980, 1986). Empirically derived or modeled A and B values were used for salp fecal pellets (Silver and Bruland 1981; Iversen et al. 2017), rhizaria (Menden-Deuer and Lessard 2000; Stukel et al. 2018), and phytoplankton (Menden-Deuer and Lessard 2000). Two parameters (i.e., A_{agg} and A_{FP}) were fit to 26 observations.

A maximum likelihood approach (i.e., Markov chain Monte Carlo) was used to fit the log-transformed carbon fluxes to the image-based analysis yielding both best-fit values and uncertainty (van Oevelen et al. 2010; Yingling et al. 2022). The *optimize.fmin* function in Python was used to determine starting values for the Markov chain Monte Carlo. A stepping scale value of 1e-11 and an exponent scale of 5 were used for both A_{agg} and A_{FP}, resulting in a reasonable percent acceptance rate of 65.7%. After burn-in, a final solution set containing 100,000 parameterizations was analyzed. The median of these values is considered the best-fit value. Uncertainty is reported as the 95% confidence interval around the median value (Appendix A).

Images of twenty-six gels were analyzed to identify particles and calculate gel-derived carbon flux estimates. Due to time restrictions, not every gel image could be analyzed. Priority was given to the GAK line as it is the most well studied portion of our study area. Gel images from each depth at GAK15 were analyzed in duplicate to determine the amount of variance between tubes. We determined variation was low and only one image per depth was analyzed for the rest of the station-depth pairs. One gel image was analyzed from each depth for the rest of the GAK line. To get a good representation of chemically-derived POC flux endmembers, one gel image from KOD5 at 27 m and one gel image from KOD10 at 53 m were analyzed, as these were the samples with the highest chemically-derived POC flux without particle overloading in the gel image. Additionally, stations MID5 and PWS2 had POC flux that increased with depth, which may be a sign of non-steady state conditions: high lateral advection or resuspension from the seafloor. These stations were excluded from image processing for these reasons. The gel-derived carbon flux estimates were within the expected uncertainty of the chemically derived carbon flux values, as most of the spread in the data is within the 2:1 and 1:2 lines (Appendix A) (Durkin et al. 2021).

2.3.6 Particle Concentration Size Distribution and Sinking Velocity

The UVP was used to calculate particle concentrations and size distributions throughout the water column. Particles from 102 µm to 26 mm were grouped into 5 m depth bins and one of 25 logarithmically spaced size bins with edges at $\left(2^{\frac{k}{3}}\right)|_{k=18}^{43}$ µm. We calculated depth-specific particle abundance by dividing the number of particles per depth bin by the volume of water imaged per depth bin (#/L).

Size-specific average sinking velocity was calculated by dividing the flux of particles in each overlapping size bin by the concentration of particles in each overlapping size bin (Equation 2.3)

$$\mathrm{v} = \frac{N_{flux}}{N_{conc}} \tag{2.3}$$

where v is the size-specific sinking velocity (m d-1), N_{flux} is the number flux of particles in a size bin (# particles in a size bin m^{-2} d^{-1}) from the gels, and N_{conc} is the number concentration of particles in a size bin (# particles in a size bin m^{-3}) from the UVP. This method averages the sinking velocity for all particles (sinking and suspended) in each size bin and can be thought of as apparent size-specific sinking velocity. Efforts were made to ensure inter-compatibility between the UVP and gel imaging systems so that a given particle would be assigned the same ESD by the UVP and gel imaging systems. We recognize that each system may have individual biases or offsets relative to the other. We note, however, that the particle size spectra from both systems displayed a high degree of autocorrelation within each sample, giving us confidence that systematic offsets, if present, would not strongly bias our results.

2.3.7 Statistical Analysis

A principal component analysis (PCA) was performed to compare stations by particle abundance and composition. The covariance matrix was calculated using the function PCA in the FactoMineR package in R. Quantitative supplementary variables calculated at each station were plotted in the same space. Variables included gel-estimated carbon flux (Est. C flux), chemically derived carbon flux (Chemical C flux), UVP-derived number concentration averaged from the 50 m above the trap (Total # concen), gel-derived number flux in (Total # flux), average UVP- and gel-derived sinking velocity averaged across sizes (Avg. sinking velocity; Equation 3), relative contribution of fecal pellet carbon flux (% FP flux), chemically-derived carbon to gel-derived volume ratio (C:V Ratio), slope of the gel-derived particle size distribution of sinking particles

(Slope of PSD) calculated as the linear slope of the number flux versus size in each gel trap, depth of the trap (depth), and average sinking particle size (Mean size) calculated as the average particle size from each gel.

2.4 Results and Discussion

2.4.1 Net Production of Carbon in the Euphotic Zone

We measured NPP to determine the near-term input of carbon to the system. NPP was variable, ranging from a low of 240 mg C m^{-2} d^{-1} in Prince William Sound (PWS2) to a high of 946 mg C m^{-2} d^{-1} near the shelf break (GAK9) (Table 2.2). NPP increased with distance from shore on the GAK and MID lines (Table 2.2, Figure 2.3, Figure 2.4). This is expected in summer, as higher rates of NPP are often observed at the shelf break where high iron coastal waters meet high nitrogen offshore waters. Observed NPP values and chlorophyll concentrations were typical for the Northern Gulf of Alaska during summer (Strom and Fredrickson 2020), despite significantly higher sea surface temperatures and greater abundances of small nanoflagellates and picophytoplankton during the summer of 2019 than typically observed (Cohen 2022).

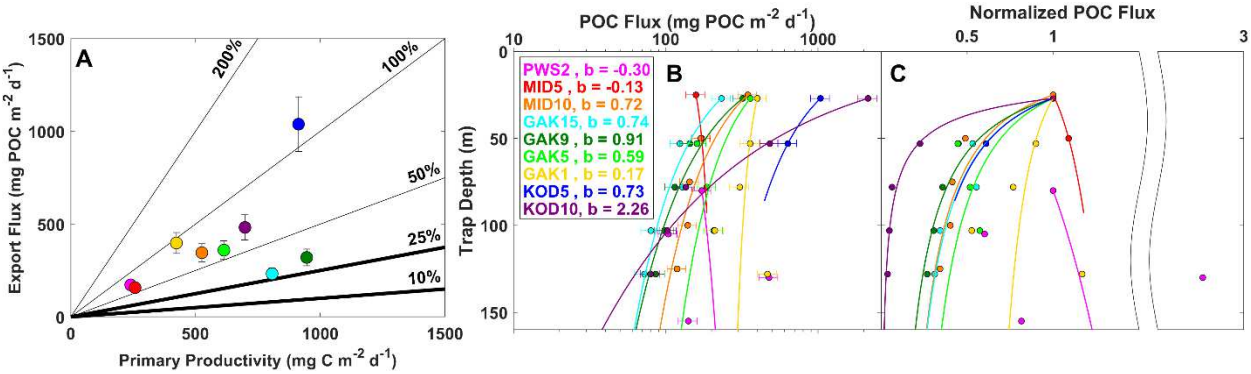

Figure 2.3: Strength and efficiency of the biological carbon pump. (A) Chemically derived bulk sinking particulate organic carbon fluxes from drifting sediment traps versus net primary productivity rates. Vertical error bars represent the average tube-to-tube standard deviation of about 14%. Diagonal lines show constant export ratios. Typical open ocean (10%) and typical shelf (25%) export ratio values are shown in bold (Dunne et al. 2007). (B) Chemically derived bulk sinking particulate organic carbon (POC) fluxes are shown over depth along with the best-fit attenuation curve and coefficient. Horizontal error bars represent the average tube-to-tube standard deviation of about 14%. (C) Normalized chemically derived sinking POC fluxes from drifting sediment traps over depth.

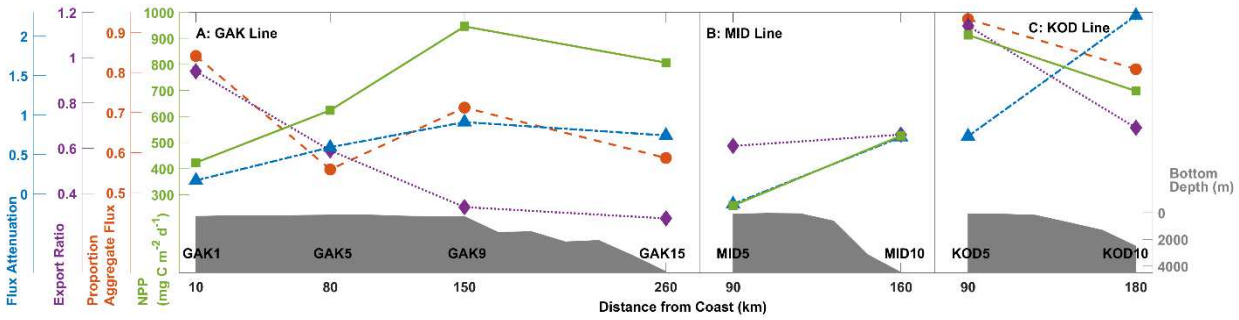

Figure 2.4: Offshore gradient in biological carbon pump properties. Flux attenuation (blue triangles), export ratio (purple diamonds), proportion aggregate flux (orange circles), and net primary productivity (NPP; green squares) along with underlying bathymetry (filled grey patch) are plotted over distance from the coast for the (A) Gulf of Alaska (GAK) line, (B) Middle Island (MID) line, (C) Kodiak (KOD) line.

Table 2.2: Net primary productivity, total integrated chlorophyll-a, fraction of chlorophyll-*a* >20 µm, particulate organic carbon (POC) export flux, and export ratios at nine stations in the Northern Gulf of Alaska.

Station	Euphotic Zone Depth (m)	Export Trap Depth (m)	Net Primary Productivity (mg C m^{-2} d^{-1})	Total integrated chlorophyll-*a* (mg m^{-2})	Fraction of chlorophyll -a > 20 µm	POC Export Flux (mg C m^{-2} d^{-1})	Export Ratio
GAK1	25	27	423	27.4	0.32	398 ± 56	0.94 ± 0.13
GAK5	29	27	614	17.5	0.06	360 ± 50	0.59 ± 0.08
GAK9	25	27	946	16.7	0.04	320 ± 45	0.34 ± 0.05
GAK15	31	27	807	30.1	0.10	232 ± 32	0.29 ± 0.04
KOD5	25	27	913	38.7	0.34	1039 ± 145	1.14 ± 0.16
KOD10	37	53	698	8.9	0.08	482 ± 67	0.69 ± 0.10
MID5	26	25	258	17.5	0.02	158 ± 22	0.61 ± 0.09
MID10	34	25	526	25.2	0.32	346 ± 48	0.66 ± 0.09
PWS2	22	80	240	58.3	0.17	172 ± 24	0.72 ± 0.10

Overall, NPP estimates in the Northern Gulf of Alaska averaged 603 ± 263 mg C m^{-2} d^{-1}, ± 1 SD (Table 2.2, Figure 2.3 panel A). For comparison, summer measurements in the offshore and high nutrient-low chlorophyll (HNLC) North Pacific at Ocean Station Papa (50°N 145°W) were

similar to or less than the Northern Gulf of Alaska: ~160 mg C m^{-2} d^{-1} (Estapa et al. 2021), 700 mg C m^{-2} d^{-1} (Buesseler and Boyd 2009) and 300 – 1500 mg C m^{-2} d^{-1} (Welschmeyer et al. 1993). We would expect similar summertime NPP at Ocean Station Papa and the Northern Gulf of Alaska because both systems are nutrient-limited at this time, the former by dissolved iron and the latter by macronutrients, and both are characterized by communities of pico- and nanophytoplankton (Booth et al. 1993; Welschmeyer et al. 1993; Strom et al. 2006). When compared to a more productive, coastal, upwelling region, the California Current Ecosystem (32 – 35°N, 120 – 124°W) has an average summertime NPP similar to the Northern Gulf of Alaska (747 ± 595 mg C m^{-2} d^{-1}, ± 1 SD) yet with a maximum NPP more than twice that of the maximum measured in the Northern Gulf of Alaska (2333 mg C m^{-2} d^{-1}) (California Current Ecosystem LTER and Goericke 2022). This is indicative of more stable summertime productivity in the Northern Gulf of Alaska than in the California Current Ecosystem. See Appendix A for a description of how the meta-analysis of the California Current Ecosystem data was conducted.

2.4.2 Strength of the Biological Carbon Pump

To determine the strength of the biological carbon pump in the Northern Gulf of Alaska, we deployed sediment traps at nine locations ranging over the continental shelf and slope during the summer of 2019 (Figure 2.1, Table 2.1, Table 2.2). Overall, particulate organic carbon (POC) export flux was high, ranging from 158 to 1039 mg C m^{-2} d^{-1} and averaging 390 ± 265 mg C m^{-2} d^{-1} (± 1 SD) (Table 2.2). The magnitude of POC export flux varied considerably by station but was generally higher near the coast and diminished offshore (Table 2.2). POC export flux at the shelf stations ranged from 158 to 1039 mg C m^{-2} d^{-1} and averaged 408 ± 324 mg C m^{-2} d^{-1} (± 1 SD) (Table 2.2). Meanwhile, POC export flux at the slope stations ranged from 232 to 482 mg C m^{-2} d^{-1} and averaged 353 ± 125 mg C m^{-2} d^{-1} (± 1 SD). Along the GAK and KOD lines at all depths, there was a clear decrease in the magnitude of POC flux progressing offshore.

To put this in context, summertime POC export flux estimates at Ocean Station Papa were 9.5 - 78.2 mg C m^{-2} d^{-1} (Estapa et al. 2021) and 97 mg C m^{-2} d^{-1} (Buesseler and Boyd 2009), about one-fifth and one-third, respectively, of the average POC export flux in the Northern Gulf of Alaska. This difference is much larger than the expected collection bias between surface-tethered and neutrally buoyant sediment traps (Baker et al. 2020; Estapa et al. 2020). In the California Current Ecosystem, POC fluxes ranged from 42 to 437 mg C m^{-2} d^{-1} and averaged

185±121 mg C m^{-2} d^{-1} (± 1 SD), with a median of 149 mg C m^{-2} d^{-1} (California Current Ecosystem LTER et al. 2022). Despite having similar or higher productivity, the average POC flux in the California Current Ecosystem was about half that of the Northern Gulf of Alaska. Additionally, the maximum POC flux measured in the California Current Ecosystem was also about half of the highest POC export flux measured in the Northern Gulf of Alaska. This indicates stronger carbon export in the Northern Gulf of Alaska than at Ocean Station Papa and the California Current Ecosystem, perhaps due to larger or more aggregates forming or less remineralization. One explanation for why aggregates could be larger or more abundant is that the Northern Gulf of Alaska is known to have strong pycnoclines (Sarkar et al. 2005), which are associated with enhanced aggregation processes (MacIntyre et al. 1995; Prairie et al. 2013). See Appendix A for a description of California Current Ecosystem data meta-analysis methods. Overall, we measured a strong biological carbon pump during the summer in the Northern Gulf of Alaska.

While we do not have previous carbon flux measurements from this region, high seasonal variability in carbon fluxes has been measured at Ocean Station Papa (Timothy et al. 2013). Additionally, the Northern Gulf of Alaska is known to have high seasonal (Waite and Mueter 2013) and interannual (Strom et al. 2016) variability in chlorophyll and primary productivity. Therefore, high seasonal and interannual variability in POC flux is likely in the Northern Gulf of Alaska.

2.4.3 Efficiency of the Biological Carbon Pump

The export ratio (i.e., export ratio = export flux / NPP, where export flux equals POC flux out of the euphotic zone) quantifies the efficiency of the biological carbon pump, with higher export ratios indicating a more efficient biological carbon pump. Export ratios ranged from 29 - 114% (average 67%, median 65%), indicating that POC was efficiently transported out of the euphotic zone during the summer of 2019 (Table 2.2, Figure 2.3, panel A). Stations with a high export ratio and relatively low primary productivity (e.g., GAK1 in yellow) can potentially indicate advected material entering the water column, non-steady-state conditions, or a collection bias. Export ratios tended to show a negative relationship with NPP and flux attenuation, being higher on the shelf and decreasing offshore (Figure 2.4), and a positive relationship with export flux (Table 2.2). The MID line showed nearly identical export ratios at MID5 and MID10. We expect stations closer to the coast to exhibit more lateral advection of particles because the Alaska

Coastal Current has a faster current speed than the Alaska Current (Reed and Schumacher 1986) and shallow shelves can allow for more resuspension of sediment from the seafloor. As such, resuspension and lateral advection of particles may cause decoupling between export flux and NPP, and could result in higher export ratios, which we observed on the inner GAK and KOD lines (Figure 2.4).

Overall, observed export ratios in the Northern Gulf of Alaska (67%) were very high compared to the average estimated export ratio in shelf ecosystems worldwide (~ 25%) (Dunne et al. 2007; Henson et al. 2015; Kelly et al. 2018). Global models predict export ratios of 0.1 to 0.15 for the Northern Gulf of Alaska (Henson et al. 2012), comparable to other measurements in the North Pacific. During summer, export ratios measured at Ocean Station Papa ranged from 6 – 18% and averaged 10% (Estapa et al. 2021) and were 14% in a previous study (Buesseler and Boyd 2009), about five times less than the average export ratio observed in the Northern Gulf of Alaska. This pattern is unexpected, as Ocean Station Papa and the Northern Gulf of Alaska share similar summertime nutrient limitation, rates of NPP, and phytoplankton community composition. However, the Northern Gulf of Alaska is closer to the coast and coastal areas generally are more associated with higher carbon flux and export efficiency (Dunne et al. 2007). In the California Current Ecosystem, a productive coastal upwelling system, summer export ratios ranged from 10 – 42% and averaged 30±11% (± 1 SD), with a nearly identical median of 31% (see Appendix A for how these values were calculated). The average export ratio in the California Current Ecosystem was about half of that in the Northern Gulf of Alaska despite the California Current Ecosystem being a high-productivity, high-flux site. Our data suggest that the summertime biological carbon pump in the Northern Gulf of Alaska is more efficient than previously assumed.

We expect that communities dominated by large cells will have higher export efficiency. Pico- and nanoplankton typically dominate the community during summertime, with 2019 as no exception (Cohen 2022). The proportion of chlA > 20 μm (microphytoplankton) ranged from 0.04 at GAK9 to 0.34 at KOD5 and averaged 0.16, generally decreased with distance from shore, and did not correlate with NPP (Table 2.2). From these data, we do not know why GAK1, KOD5, and MID10 had the highest proportions of chlA > 20 μm, however generally larger cells are often found in areas with more nutrient flux (Mousing et al. 2018). Perhaps higher iron availability near the coast allows for larger cells to grow, as diatoms are sensitive to iron

limitation (Strom et al. 2016) or perhaps mesoscale eddies increased nutrient flux at some stations (Crawford et al. 2007). The proportion of chlA > 20 µm positively correlated with export ratios (Pearson correlation coefficient, r(7) = .49, p = .02) (Figure 2.5). This suggests that larger phytoplankton are driving carbon export efficiency, even though they make up a minority of total chlA. Pico and nanoplankton are thought to contribute to less efficient export due to their smaller size and lack of ballasting (Stokes 1851; Michaels and Silver 1988). However, other studies suggest that picoplankton can be exported efficiently if aggregates are formed (Richardson and Jackson 2007; Richardson 2019). Our data support the hypothesis that communities dominated by small cells can have efficient export, but more efficient export is likely when the proportion of large cells is higher.

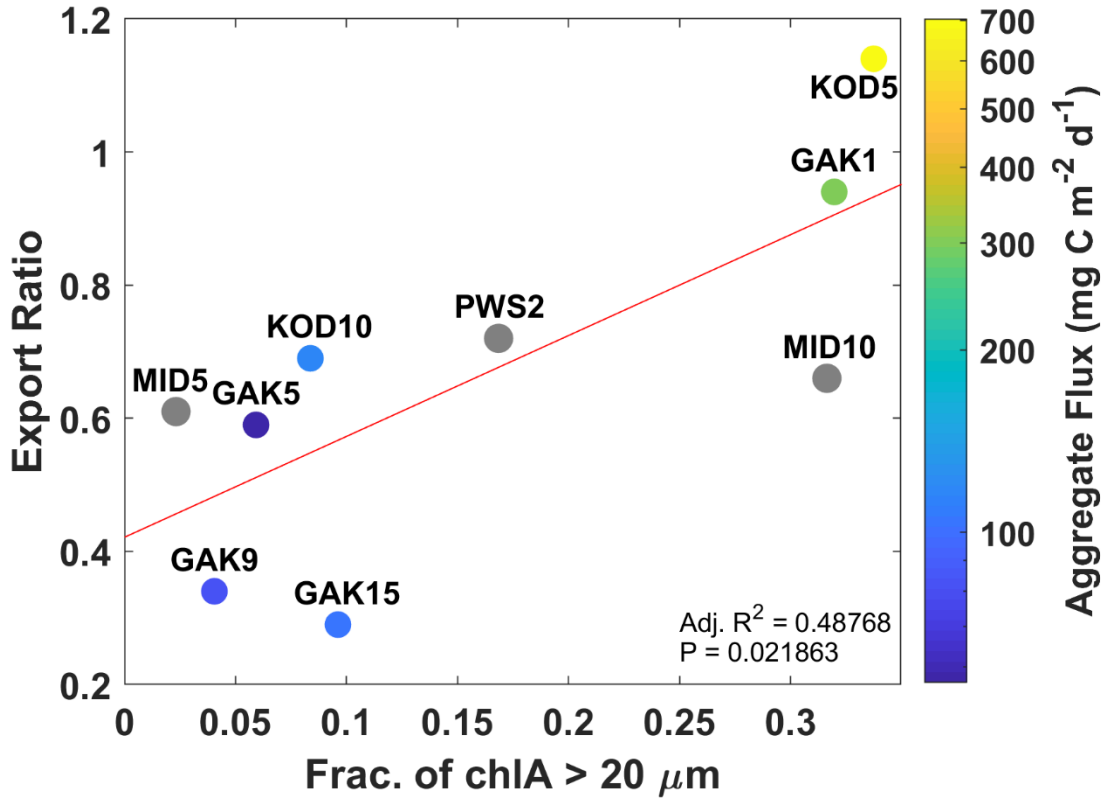

Figure 2.5: Drivers of efficient export. Fraction of chlorophyll-a (chlA) > 20 µm significantly correlates with export ratio (Pearson correlation coefficient, r(7) = .49, p = .02) colored by aggregate flux (in mg C m^{-2} d^{-1}). Linear regression between the fraction of chlA > 20 µm and export ratio is shown as the red line. Grey symbols indicate no associated aggregate flux measurement.

POC fluxes generally decreased over depth consistent with a power-law curve (Figure 2.3, panels B and C), with an exponent (b) describing how efficiently POC is transported from the base of the euphotic zone into the deep ocean (e.g., originally proposed as b = 0.86) (Martin et al. 1987; Buesseler et al. 2007). In our data, b ranged from -0.3 to 2.26, with lower values indicating a more efficient transfer of POC from the euphotic zone into the deep ocean. Our observations were lower (mean: 0.63 ± 0.74, ± 1 SD, reference depth ~25 m) than many typically observed (e.g., 0.86 in the northeast Pacific, reference depth 100 m, (Martin et al. 1987), 1.16 at Ocean Station Papa, reference depth 100 m, (Buesseler and Boyd 2009), 1.33 at station ALOHA, reference depth 150 m, (Buesseler et al. 2007)). When interpreting these comparisons, it should be noted that flux attenuation is dependent on the depth of the upper trap (i.e., the reference depth) (Buesseler et al. 2020). It is somewhat unexpected that we measured such low POC flux attenuation in the Northern Gulf of Alaska, as higher flux areas, i.e., coastal areas and higher latitude systems, often are modeled to have higher POC flux attenuation (Henson et al. 2012; Marsay et al. 2015). However, this topic is still being debated, as other modeling studies find a more efficient biological carbon pump in high-latitude systems (Weber et al. 2016). Our observed, rather than modeled, POC flux attenuation measurements provide important evidence of an efficient biological carbon pump in a subarctic coastal system.

POC flux attenuation also varied spatially in our study. PWS2 and MID5 both had negative attenuation coefficients, indicating an increase in carbon flux with depth. MID5 was the shallowest station (bottom depth ~100 m) and therefore may have been experiencing resuspension from the seafloor or increased lateral transport due to the sharp gradient of bathymetry at nearby Middleton Island. The shallowest trap at PWS2 was 80m, far below the actual euphotic zone depth of 22 m. This substantially increases the uncertainty of the best-fit b value. Overall, carbon flux attenuation increased with distance from shore along all lines and had a similar pattern as NPP (Figure 2.4).

2.4.4 Contribution of Carbon Flux by Particle Types

To calculate the contribution of POC flux by particle type, we imaged the sinking particles, segmented those particles, identified particle types, and calculated particle volume by equivalent spherical diameter (ESD). Finally, we modeled A and B values using Equation 2.2 to find the best fit between the chemically derived POC flux and gel-estimated POC flux. Using this

method, we can determine the contribution of each particle type (i.e., aggregates, fecal pellets, etc.) to the total POC flux.

The best-fit value A_{agg} for aggregates and unidentifiable particles was 1.5 x 10-10 mg C μm^{-3} with a 95% confidence interval of 0.7 – 2.2 x 10-10 mg C μm^{-3} (Appendix A). The best-fit A_{FP} value for dense detritus, long, large loose, short, and mini fecal pellets was smaller than A_{agg} (1.2 x 10-11 mg C μm^{-3} with a 95% confidence interval of 0.1 – 3.8 x 10-11 mg C μm^{-3}). This smaller A value is paired with a larger B value of 1 (as compared to 0.8), such that aggregates and fecal pellets of the same ESD have carbon contents of the same order of magnitude over the size range we analyze from the polyacrylamide gels (~20 – 3000 μm). These values agree well with previous empirically or model-derived values. See Appendix A for a mini-review of these model results compared to empirical values.

The majority of the POC flux at nearly all stations and depths comes from aggregates, ranging from 41 - 93% and averaging 61 ± 13% (± 1 SD) (Figure 2.6, Appendix A). This majority further increases when considering all non-fecal pellet sources, i.e., the combined contribution of aggregates, dense detritus, and unidentifiable particles, ranging from 54 - 96% and averaging 74 ± 11% (± 1 SD). Most particles identified as aggregates and dense detritus appeared to be made up largely of green phytoplankton-derived material. Carbon from fecal pellets made up a small percentage of sinking carbon flux, ranging from 4 - 45% and averaging 25 ± 10% (± 1 SD). Both overall and relative carbon flux from short fecal pellets, likely coming from small copepods (e.g., *Pseudocalanus*) or larvaceans (Wilson et al. 2008), increased with distance from shore. Long fecal pellets, likely from large copepods (e.g., *Calanus marshallae*, *Metridia pacifica*) or euphausiids (Wilson et al. 2008), were the most important fecal pellet type for carbon flux and relative carbon flux at all stations except KOD5 where large loose pellets, mini pellets, and short pellets all contributed higher carbon flux and relative flux than long fecal pellets. Ninety-five percent of the variability in overall gel-derived carbon flux was due to variability in aggregate carbon flux. The relative contribution of aggregates decreased offshore on the KOD line and decreased offshore on the GAK line with some variability (Figure 2.4). Aggregates contributed the most to carbon flux at GAK1, followed by GAK9, GAK15, and GAK5. This indicates that grazing pressure from fecal pellet-producing zooplankton could be relatively higher offshore. Trends in total fecal pellet carbon flux were mostly due to relative and total contributions of short fecal pellets. Therefore, we looked at the distributions of two taxa that

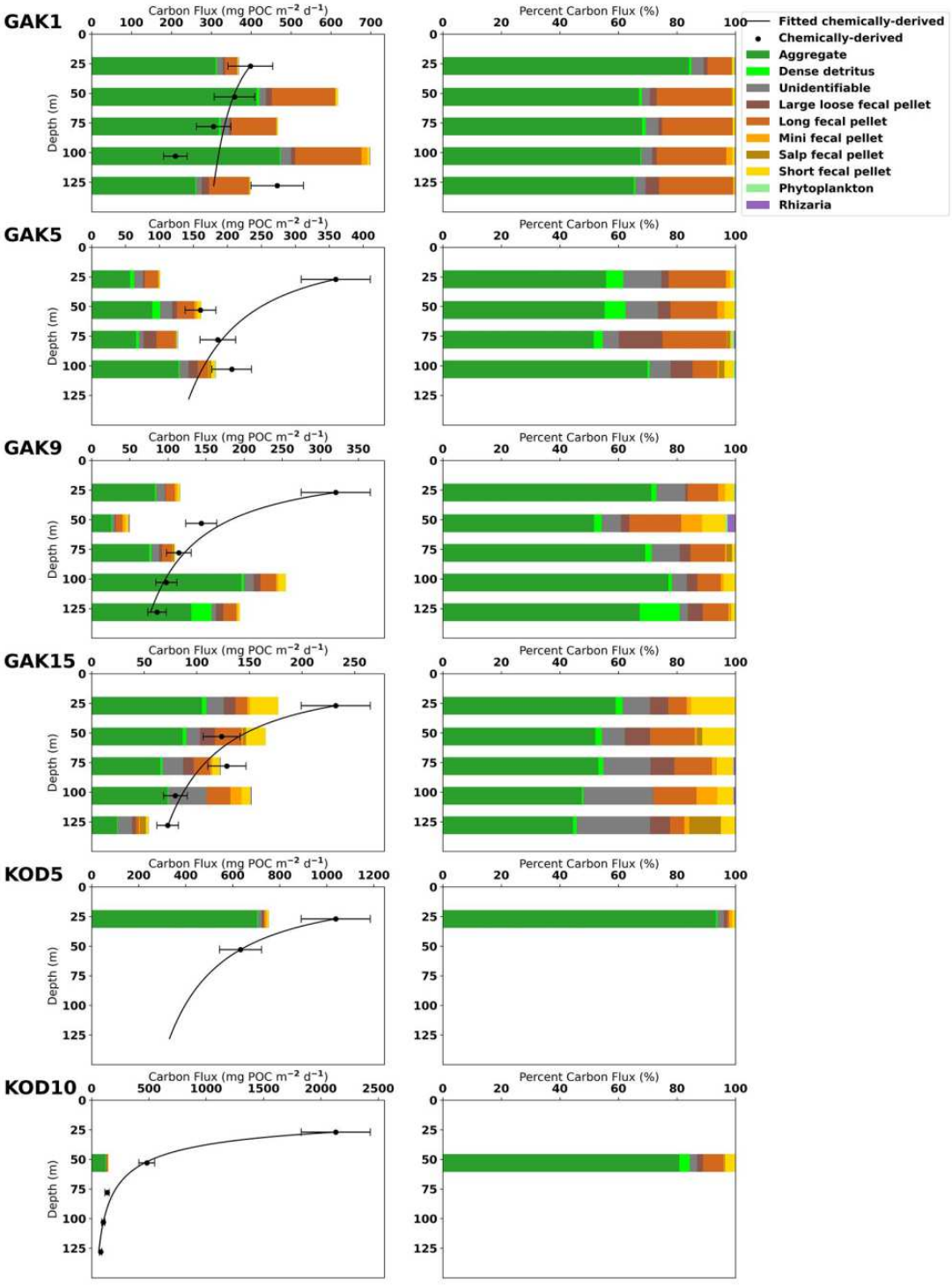

Figure 2.6: Contribution of carbon flux by particle type. Left columns: Depth profiles of gel-derived particulate organic carbon (POC) flux from June and July 2019 in the Northern Gulf of Alaska by each particle type at the indicated locations. Black circles show the corresponding chemically-derived bulk POC fluxes with POC attenuation shown in black. Horizontal error bars indicate an average tube-to-tube error of about 14%. Right columns: Depth profiles of relative POC flux by particle type from gel analysis.

produce short fecal pellets: small copepods (e.g., *Pseudocalanus*) and larvaceans. *Pseudocalanus* have been observed to be in higher abundance on the shelf during summer in the Northern Gulf of Alaska, so they are unlikely to contribute to the pattern we see of increasing flux of short fecal pellets offshore (Napp et al. 2005). Certain species of grazing larvaceans (e.g., *Fritillaria borealis*) have been observed to be in higher abundance offshore during the summer in this region (Doubleday and Hopcroft 2014) and could potentially explain the pattern of short fecal pellets. Another explanation is that the pycnocline is stronger near the coast, which is associated with enhanced aggregation (MacIntyre et al. 1995; Prairie et al. 2013). Coastal stations with the highest export efficiency also had higher proportions of chlorophyll a > 20 μm (Figure 2.5); these patterns may be driven by larger phytoplankton such as diatoms in poor physiological condition due to macronutrient limitation, that are known to sink rapidly (Michaels and Silver 1988). These results are in line with previous observations of marine particles in the Northern Gulf of Alaska where most large particles (> 0.5 mm) were observed to be detrital aggregates (Turner et al. 2017). However, at Ocean Station Papa during the summer, long, mini, and salp fecal pellets have been observed to dominate carbon flux at all depths (~100 m – 500 m) (Durkin et al. 2021). Overall, we observed an efficient biological carbon pump with high export ratios and a predominance of aggregate flux.

GAK1, GAK5, and GAK9 showed some signs of increasing gel-derived POC flux over depth, while the chemically derived POC fluxes decreased with depth at these stations (Figure 2.6). This could be explained by carbon-to-volume ratios that change with depth. As particles sink and undergo remineralization, their mass may decrease while their ESD remains the same. Future studies should explore this idea to determine whether improving the fit between chemically- and gel-derived POC fluxes is possible. Additionally, we are most likely to miss small particles when identifying particles in the gel images, therefore underestimating carbon flux from small particles. The mismatch between chemically-derived and gel-derived carbon flux could also further support the theory that small particles are important to carbon flux (Richardson and Jackson 2007; Durkin et al. 2015; Richardson 2019).

2.4.5 Drivers of Carbon Export

To determine if certain particle types were correlated with higher carbon export, a PCA was performed on the carbon flux by particle type at each station/depth sample (Figure 2.7, panel A). Aggregate carbon flux is strongly associated with total carbon flux, phytoplankton flux, and long

fecal pellet flux (Figure 2.7, panel B). Gel-estimated carbon flux tended to decrease as stations moved offshore (Figure 2.7, panel C). Total number concentration (i.e., ambient particle concentrations) and total number flux are both positively correlated to carbon flux. Interestingly, sinking velocity, mean sinking particle size, and trap depth are poor indicators of total carbon flux. The carbon-to-volume ratio has an inverse relationship with carbon flux. Estimated carbon flux from aggregates, long fecal pellets, and phytoplankton are significantly correlated (linear regression, F-statistic, $p < 0.05$) with the total carbon flux; however, carbon flux from aggregates most strongly correlates with carbon flux.

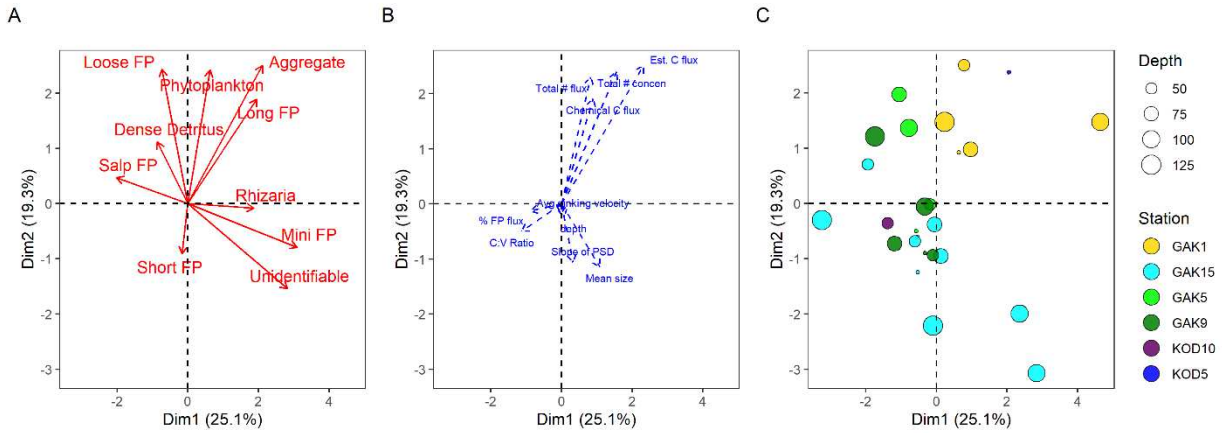

Figure 2.7: (A) PCA on the carbon flux by particle type at each station/depth location, shown in red arrows: FP = Fecal Pellet. (B) Quantitative supplementary variables estimated at each depth/station pair: total gel-estimated carbon flux (Est. C flux), total chemically-derived particulate organic carbon flux (Chemical C flux), total number concentration averaged from the 50 m above the trap depth (Total # concen), gel-derived total number flux (Total # flux), average sinking velocity (Avg. sinking velocity), relative contribution of fecal pellets to carbon flux (% FP flux), calculated carbon to volume ratio (C:V Ratio), slope of the gel-derived particle size distribution of sinking particles (Slope of PSD), depth of the trap (depth), and average sinking particle size (Mean size). (C) Individuals are plotted as colored dots corresponding to a sample (i.e., one depth/station pair). Colors and size correspond with the station and depth at which the sediment trap sampled, respectively.

Efficient export in the Northern Gulf of Alaska during summer is driven by a few parameters. Export ratio correlated significantly with the proportion of chlA > 20 µm, total aggregate flux, export flux, and percent aggregate flux (Pearson, $p \leq .05$) (Figure 2.5). Aggregate flux also significantly correlated with the proportion of chlA > 20 µm (Pearson, $p \leq .05$) (Figure 2.5). Interestingly, NPP does not significantly correlate with any other variable. KOD5 and GAK1, for example, had the highest export ratios, proportion of chlA > 20 µm, and contributions of

aggregate flux. This provides a framework for conditions that allow for efficient export, besides efficient export driven by high fecal pellet flux as previously described (Ebersbach and Trull 2008; Laurenceau-Cornec et al. 2015).

To determine if certain particle types more efficiently transport carbon to depth, we performed linear regressions on carbon flux over depth from different stations and different particle types (Appendix A). Certain particle types are not more likely to reach different depths than others. Only four of these carbon fluxes by station and particle type combinations have significant relationships over depth; at GAK15, aggregates decreased over depth with a slope of -0.67 ($p = 0.025$), dense detritus decreased over depth with a slope of -0.04 ($p = 0.005$), and short fecal pellets decreased over depth with a slope of -0.23 ($p = 0.016$); at GAK9 large loose fecal pellets increased over depth with a slope of 0.10 ($p = 0.011$). Within each particle type, the slopes also have mixed positive and negative relationships depending on the station. Therefore, these data do not strongly support a claim that carbon from certain particle types is more or less likely to reach deeper depths than other particle types.

Debate continues over whether zooplankton fecal pellet production through the consumption of phytoplankton and aggregates results in higher or lower carbon export (Turner 2015). In some studies, systems with less dense, sometimes smaller material that is repackaged into larger, denser fecal pellets result in higher carbon export (Iversen and Lampitt 2020). In other studies, mineral ballasted aggregates exported carbon more effectively than fecal pellets (Armstrong et al. 2002), as fecal pellets can have high rates of particle-associated microbial respiration (Smetacek 1985; Ploug et al. 2008a; Kobari et al. 2013). Our results suggest that particle type did not strongly impact the efficiency at which POC was transferred from the euphotic zone to the deep ocean during summer in the Northern Gulf of Alaska. One caveat is that our deepest trap was around 125 m, relatively shallow. It is possible that the particle type-specific effects only apply to the deeper ocean.

Performing a similar analysis against particle sizes, we found no significant difference in ESDs with depth, station, or type (Appendix A). The absence of relationships between particle size and depth is consistent with three different explanations. First, if particle formation below the euphotic zone is minor compared to flux from the euphotic zone, then consistency of particle sizes would imply similar attenuation length scales across particle classes. Secondly, if particle formation below the euphotic zone is significant relative to euphotic zone export, then it implies

that particles formed in the twilight zone have size spectra similar to those formed in the euphotic zone, and perhaps that similar repackaging processes are dominant. Thirdly, it is possible that the particle size-specific effects are relatively slow compared to the residence time of sinking particles above our traps and that deeper traps may resolve such patterns.

2.4.6 Marine Heatwave

During 2019 sea surface temperatures in the Northern Gulf of Alaska were about 2°C warmer than the long-term mean (Danielson et al. 2022), characteristic of a marine heatwave. The 2019 marine heatwave was associated with higher abundances of picophytoplankton observed during the summer in the Northern Gulf of Alaska (Cohen 2022). Generally, warmer ocean temperatures are thought to increase microbial respiration rates and decrease the sinking speed of particles generated by the food web (Michaels and Silver 1988; Vaqué et al. 2019). However, we measured a strong and efficient biological carbon pump characterized by a high proportion of aggregate flux during the summer in the Northern Gulf of Alaska. If our observations of a strong and efficient biological carbon pump are representative of this system, this might imply that the biological carbon pump in the Northern Gulf of Alaska is even stronger and more efficient in non-heatwave summers.

2.5 Conclusions

This study is the first description of the biological carbon pump in the Northern Gulf of Alaska. The biological carbon pump was strong and efficient during the summer of 2019. Net primary productivity (NPP) was typical of other past measurements in the subarctic and coastal North Pacific; however, particulate organic carbon (POC) fluxes and export ratios were much higher, with lower carbon flux attenuation and higher contributions of aggregates, than prior results from similar regions (Buesseler and Boyd 2009; Durkin et al. 2021; Estapa et al. 2021). By using a comprehensive approach that brings together sediment trap sampling and imaging, optically measured distribution of sinking and suspended particles, and incubations, our data suggest that the main driver of carbon flux in the Northern Gulf of Alaska during summer was aggregation processes and the main drivers of efficient carbon export were the proportion of chlorophyll-a in the large size fraction (>20 μm) and aggregation processes. These results lead us to question our expectations about conditions and processes creating strong and efficient flux events. Clearly strong and efficient flux events can originate from communities dominated by

pico- and nanophytoplankton, with moderate contribution from zooplankton fecal pellets. These results can help improve the climate and ecological models for this region and the broader subarctic coastal region to better predict the fate of organic material produced through photosynthesis.

2.6 References

Aguilar-Islas, A. M., M. J. M. Séguret, R. Rember, K. N. Buck, P. Proctor, C. W. Mordy, and N. B. Kachel. (2016) Temporal variability of reactive iron over the Gulf of Alaska shelf. *Deep-Sea Research II*. 132, 90–106. doi:10.1016/j.dsr2.2015.05.004

Alldredge, A. (1998) The carbon, nitrogen and mass content of marine snow as a function of aggregate size. *Deep-Sea Research I*. 45, 529–541.

Armstrong, R., C. Lee, J. Hedges, S. Honjo, and S. G. Wakeham. (2002) A new, mechanistic model for organic carbon fluxes in the ocean based on the quantitative association of POC with ballast minerals. *Deep-Sea Research II*. 49, 219–236.

Baker, C. A., M. L. Estapa, M. Iversen, R. Lampitt, and K. Buesseler. (2020) Are all sediment traps created equal? An intercomparison study of carbon export methodologies at the PAP-SO site. *Progress in Oceanography*. 184, 102317. doi:10.1016/j.pocean.2020.102317

Bernstein, R. E., P. R. Betzer, R. A. Feely, R. H. Byrne, M. F. Lamb, and A. F. Michaels. (1987) Acantharian fluxes and strontium to chlorinity ratios in the North Pacific Ocean. *Science*. (1979) 237, 1490–1494. doi:10.1126/science.237.4821.1490

Bishop, J. K. B., R. W. Collier, D. R. Kettens, and J. M. Edmond. (1980) The chemistry, biology, and vertical flux of particulate matter from the upper 1500 m of the Panama Basin*. *Deep-Sea Research*. 27, 615–640.

Bishop, J. K., J. C. Stepien, and P. H. Wiebe. (1986) Particulate matter distributions, chemistry and flux in the Panama Basin: Response to environmental forcing. *Progress in Oceanography*. 17: 1–59.

Booth, B. C., J. Lewin, and S. R. Postel. (1993) Temporal variation in the structure of autotrophic and heterotrophic communities in the subarctic Pacific. *Progress in Oceanography*. 32: 57–99.

Buesseler, K. O., and P. W. Boyd. (2009) Shedding light on processes that control particle export and flux attenuation in the twilight zone of the open ocean. *Limnology and Oceanography*. 54: 1210–1232. doi:10.4319/lo.2009.54.4.1210

Buesseler, K. O., P. W. Boyd, E. E. Black, and D. A. Siegel. (2020) Metrics that matter for assessing the ocean biological carbon pump. *Proceedings in the National Academy of Science of the USA.* 117: 9679–9687. doi:10.1073/pnas.1918114117

Buesseler, K. O., C. H. Lamborg, P. W. Boyd, P. J. Lam, T. W. Trull, R. R. Bidigare, J. K. Bishop, K. L. Casciotti, F. Dehairs, M. Elskens, M. Honda, D. M. Karl, D. A. Siegel, M. W. Silver, D. K. Steinberg, J. Valdes, B. V. Mooy, and S. Wilson. (2007) Revisiting carbon flux through the ocean's twilight zone. *Science*. (1979) 316: 567–570. doi:10.1126/science.1137959

California Current Ecosystem LTER, and G. Goericke. (2022) Water column primary production per day integrated over the euphotic zone from CCE LTER process cruises in the California Current System, 2006 - 2019 (ongoing). ver 5. *Environmental Data Initiative*. doi:10.6073/pasta/9dddc0e6ab3c0ac48d41e04811a1870f (Accessed 2023-02-28)

California Current Ecosystem LTER, M. Stukel, and M. Landry. (2022) Exported particulate carbon and nitrogen measurements from 4-day sediment trap deployments in the CCE region, 2007 - 2019 (ongoing). ver 7. *Environmental Data Initiative*. doi:10.6073/pasta/cdee03ef7b17c2a4027a4a8b33c5b09b (Accessed 2023-03-01)

Childers, A. R., T. E. Whitledge, and D. A. Stockwell. (2005) Seasonal and interannual variability in the distribution of nutrients and chlorophyll a across the Gulf of Alaska shelf: 1998-2000. *Deep-Sea Research II*. 52: 193–216. doi:10.1016/j.dsr2.2004.09.018

Cohen, J. (2022) Shifts in microbial community composition during the 2019 Pacific marine heatwave in the northern Gulf of Alaska. MS Thesis, University of Alaska Fairbanks.

Crawford, W. R., P. J. Brickley, and A. C. Thomas. (2007) Mesoscale eddies dominate surface phytoplankton in northern Gulf of Alaska. *Progress in Oceanography*. 75: 287–303. doi:10.1016/j.pocean.2007.08.016

Danielson, S. L., T. D. Hennon, D. H. Monson, R. M. Suryan, R. W. Campbell, S. J. Baird, K. Holderied, and T. J. Weingartner. (2022) Temperature variations in the northern Gulf of Alaska across synoptic to century-long time scales. *Deep-Sea Research II*. doi:10.1016/j.dsr2.2022.105155

Doubleday, A. J., and R. R. Hopcroft. (2014) Interannual patterns during spring and late summer of larvaceans and pteropods in the coastal Gulf of Alaska, and their relationship to pink salmon survival. *Journal of Plankton Research*. 37: 134–150. doi:10.1093/plankt/fbu092

Dunne, J. P., J. L. Sarmiento, and A. Gnanadesikan. (2007) A synthesis of global particle export from the surface ocean and cycling through the ocean interior and on the seafloor. *Global Biogeochemical Cycles*. 21: 1–16. doi:10.1029/2006GB002907

Durkin, C. A., K. O. Buesseler, I. Cetinić, M. L. Estapa, R. P. Kelly, and M. Omand. (2021) A visual tour of carbon export by sinking particles. *Global Biogeochemical Cycles*. 35: 1–17. doi:10.1029/2021GB006985

Durkin, C. A., M. L. Estapa, and K. O. Buesseler. (2015) Observations of carbon export by small sinking particles in the upper mesopelagic. *Marine Chemistry*. 175: 72–81. doi:10.1016/j.marchem.2015.02.011

Ebersbach, F., and T. Trull. (2008) Sinking particle properties from polyacrylamide gels during the KErguelen Ocean and Plateau compared Study (KEOPS): Zooplankton control of carbon export. *Limnology and Oceanography*. 53: 212–224.

Estapa, M., K. Buesseler, C. A. Durkin, M. Omand, C. R. Benitez-Nelson, M. Roca-Martí, E. Breves, R. P. Kelly, and S. Pike. (2021) Biogenic sinking particle fluxes and sediment trap collection efficiency at Ocean Station Papa. *Elementa*. 9. doi:10.1525/elementa.2020.00122

Estapa, M., J. Valdes, K. Tradd, J. Sugar, M. Omand, and K. Buesseler. (2020) The neutrally buoyant sediment trap: Two decades of progress. *Journal of Atmospheric and Ocean Technology*. 37: 957–973. doi:10.1175/JTECH-D-19-0118.1

Guidi, L., G. A. Jackson, L. Stemmann, J. C. Miquel, M. Picheral, and G. Gorsky. (2008) Relationship between particle size distribution and flux in the mesopelagic zone. *Deep-Sea Research I*. 55: 1364–1374. doi:10.1016/j.dsr.2008.05.014

Hama, T., T. Miyazaki, Y. Ogawa, T. Iwakuma, M. Takahashi, A. Otsuki, and S. Ichimura. (1983) Measurement of photosynthetic production of a marine phytoplankton population using a stable 13C isotope. *Marine Biology*. 73: 31–36. doi:10.1007/BF00396282

Henson, S. A., R. Sanders, and E. Madsen. (2012) Global patterns in efficiency of particulate organic carbon export and transfer to the deep ocean. *Global Biogeochemical Cycles*. 26: 1–14. doi:10.1029/2011GB004099

Henson, S. A., R. Sanders, E. Madsen, P. J. Morris, F. Le Moigne, and G. D. Quartly. (2011) A reduced estimate of the strength of the ocean's biological carbon pump. *Geophysical Research Letters*. 38. doi:10.1029/2011GL046735

Henson, S. A., A. Yool, and R. Sanders. (2015) Variability in efficiency of particulate organic carbon export: A model study. *Global Biogeochemical Cycles*. 29: 33–45. doi:10.1002/2014GB004965.Received

Iversen, M. H., and R. S. Lampitt. (2020) Size does not matter after all: No evidence for a size-sinking relationship for marine snow. *Progress in Oceanography*. 189: 102445. doi:10.1016/j.pocean.2020.102445

Iversen, M. H., E. A. Pakhomov, B. P. V. Hunt, H. van der Jagt, D. Wolf-Gladrow, and C. Klaas. (2017) Sinkers or floaters? Contribution from salp pellets to the export flux during a large bloom event in the Southern Ocean. *Deep-Sea Research II*. 138: 116–125. doi:10.1016/j.dsr2.2016.12.004

Iversen, M. H., and H. Ploug. (2010) Ballast minerals and the sinking carbon flux in the ocean: Carbon-specific respiration rates and sinking velocity of marine snow aggregates. *Biogeosciences*. 7: 2613–2624. doi:10.5194/bg-7-2613-2010

Jaeger, J. M., and C. A. Nittrouer. (2006) A quantitative examination of modern sedimentary lithofacies formation on the glacially influenced Gulf of Alaska continental shelf. *Continental Shelf Research*. 26: 2178–2204. doi:10.1016/j.csr.2006.07.014

Johnson, C. P., X. Li, and B. E. Logan. (1996) Settling velocities of fractal aggregates. *Environmental Science Technology*. 30: 1911–1918.

Kelly, T. B., R. Goericke, M. Kahru, H. Song, and M. R. Stukel. (2018) CCE II: Spatial and interannual variability in export efficiency and the biological pump in an eastern boundary current upwelling system with substantial lateral advection. *Deep-Sea Research I*. 140: 14–25. doi:10.1016/j.dsr.2018.08.007

Knauer, G. A., J. H. Martin, and K. W. Bruland. (1979) Fluxes of particulate carbon, nitrogen, and phosphorus in the upper water column of the northeast Pacific. *Deep-Sea Research Part A*. 26: 97–108. doi:10.1016/0198-0149(79)90089-X

Kobari, T., M. Kitamura, M. Minowa, H. Isami, H. Akamatsu, H. Kawakami, K. Matsumoto, M. Wakita, and M. C. Honda. (2013) Impacts of the wintertime mesozooplankton community to downward carbon flux in the subarctic and subtropical Pacific Oceans. *Deep-Sea Research I*. 81: 78–88. doi:10.1016/j.dsr.2013.07.003

De La Rocha, C. L., and U. Passow. (2007) Factors influencing the sinking of POC and the efficiency of the biological carbon pump. *Deep-Sea Research II*. 54: 639–658. doi:10.1016/j.dsr2.2007.01.004

Ladd, C., W. Cheng, and S. Salo. (2016) Gap winds and their effects on regional oceanography Part II: Kodiak Island, Alaska. *Deep-Sea Research II*.132: 54–67. doi:10.1016/j.dsr2.2015.08.005

Lampitt, R. S., I. Salter, and D. Johns. (2009) Radiolaria: Major exporters of organic carbon to the deep ocean. *Global Biogeochemical Cycles*. 23. doi:10.1029/2008GB003221

Laufkötter, C., M. Vogt, N. Gruber, O. Aumont, L. Bopp, S. C. Doney, J. P. Dunne, J. Hauck, J. G. John, I. D. Lima, R. Seferian, and C. Völker. (2016) Projected decreases in future marine export production: The role of the carbon flux through the upper ocean ecosystem. *Biogeosciences*. 13: 4023–4047. doi:10.5194/bg-13-4023-2016

Laurenceau-Cornec, E. C., T. W. Trull, D. M. Davies, S. G. Bray, J. Dorian, F. Planchon, F. Carlotti, M. P. Jouandet, A. J. Cavagna, A. M. Waite, and S. Blain. (2015) The relative importance of phytoplankton aggregates and zooplankton fecal pellets to carbon export: Insights from free-drifting sediment trap deployments in naturally iron-fertilised waters near the Kerguelen Plateau. *Biogeosciences*. 12: 1007–1027. doi:10.5194/bg-12-1007-2015

MacIntyre, S., A. L. Alldredge, and C. C. Gotschalk. (1995) Accumulation of marines now at density discontinuities in the water column. *Limnology and Oceanography*. 40: 449–468. doi:10.4319/lo.1995.40.3.0449

Macklin, S. A., N. A. Bond, and J. P. Walker. (1990) Structure of a low-level jet over lower Cook Inlet, Alaska. *Monthly Weather Review*. 118: 2568–2578.

Marsay, C. M., E. P. Achterberg, K. Pabortsava, S. A. Henson, R. J. Sanders, and R. S. Lampitt. 2015. Attenuation of sinking particulate organic carbon flux through the mesopelagic ocean. *Proceedings of the National Academy of Sciences*. 112: 1089–1094. doi:10.1073/pnas.1415311112

Martin, J. H., G. A. Knauer, D. M. Karl, and W. W. Broenkow. (1987) VERTEX: carbon cycling in the northeast Pacific. *Deep-Sea Research*. 34: 267–285.

Menden-Deuer, S., and E. J. Lessard. (2000) Carbon to volume relationships for dinoflagellates, diatoms, and other protist plankton. *Limnology and Oceanography*. 45: 569–579. doi:10.4319/lo.2000.45.3.0569

Michaels, A. F., D. A. Caron, N. R. Swanberg, F. A. Howse, and C. M. Michaels. (1995) Planktonic sarcodines (Acantharia, Radiolaria, Foraminifera) in surface waters near Bermuda: abundance, biomass and vertical flux. *Journal of Plankton Research*. 17: 131–163. doi:10.1093/plankt/17.1.131

Michaels, A. F., and M. W. Silver. (1988) Primary production, sinking fluxes and the microbial food web. *Deep-Sea Research*. 35: 473–490.

Moran, S. B., R. P. Kelly, K. Iken, J. T. Mathis, M. W. Lomas, and R. Gradinger. (2012) Seasonal succession of net primary productivity, particulate organic carbon export, and autotrophic community composition in the eastern Bering Sea. *Deep-Sea Research II*. 65–70: 84–97. doi:10.1016/j.dsr2.2012.02.011

Mordy, C. W., P. J. Stabeno, N. B. Kachel, C. Ladd, M. Zimmermann, A. J. Hermann, K. O. Coyle, and M. J. Doyle. (2019) Patterns of flow in the canyons of the northern Gulf of Alaska. *Deep-Sea Research II*. 165: 203–220. doi:10.1016/j.dsr2.2019.03.009

Moriarty, R., E. T. Buitenhuis, and C. Le Quéré. (2013) Distribution of known macrozooplankton abundance and biomass in the global ocean. *Earth System Science Data*. 5: 241–257. doi:10.5194/essd-5-241-2013

Mousing, E. A., K. Richardson, and M. Ellegaard. (2018) Global patterns in phytoplankton biomass and community size structure in relation to macronutrients in the open ocean. *Limnology and Oceanography*. 63: 1298–1312. doi:10.1002/lno.10772

Muench, R. D., H. O. Mofjeld, and R. L. Charnell. (1978) Oceanographic conditions in lower cook inlet: spring and summer 1973. *Journal of Geophysical Research*. 83: 5090. doi:10.1029/jc083ic10p05090

Napp, J. M., R. R. Hopcroft, C. T. Baier, and C. Clarke. (2005) Distribution and species-specific egg production of Pseudocalanus in the Gulf of Alaska. *Journal of Plankton Research*. 27: 415–426. doi:10.1093/plankt/fbi015

Napp, J. M., L. S. Incze, P. B. Ortner, D. L. W. Siefert, and L. Britt. (1996) The plankton of Shelikof Strait, Alaska: Standing stock, production, mesoscale variability and their relevance to larval fish survival. *Fisheries Oceanography*. 5: 19–38. doi:10.1111/j.1365-2419.1996.tb00080.x

O'Daly, S. H., S. L. Danielson, S. M. Hardy, R. R. Hopcroft, C. Lalande, D. A. Stockwell, and A. M. P. McDonnell. 2020. Extraordinary carbon fluxes on the shallow pacific arctic shelf during a remarkably warm and low sea ice period. *Frontiers in Marine Science*. 7. doi:10.3389/fmars.2020.548931

van Oevelen, D., K. van den Meersche, F. J. R. Meysman, K. Soetaert, J. J. Middelburg, and A. F. Vézina. (2010) Quantifying food web flows using linear inverse models. *Ecosystems*. 13: 32–45. doi:10.1007/s10021-009-9297-6

Owens, S. A., K. O. Buesseler, C. H. Lamborg, J. Valdes, M. W. Lomas, R. J. Johnson, D. K. Steinberg, and D. A. Siegel. (2013) A new time series of particle export from neutrally buoyant sediments traps at the Bermuda Atlantic Time-series Study site. *Deep-Sea Research I*. 72: 34–47. doi:10.1016/j.dsr.2012.10.011

Parsons, T. R. (1987) Ecological Relations, p. 561–570. In D.W. Hood and S.T. Zimmerman [eds.], The Gulf of Alaska: Physical Environment and Biological Resources. NOAA, U.S. Department of Commerce.

Ploug, H., M. H. Iversen, and G. Fischer. (2008a) Ballast, sinking velocity, and apparent diffusivity within marine snow and zooplankton fecal pellets: Implications for substrate turnover by attached bacteria. *Limnology and Oceanography*. 53: 1878–1886. doi:10.4319/lo.2008.53.5.1878

Ploug, H., M. H. Iversen, M. Koski, and E. T. Buitenhuis. (2008b) Production, oxygen respiration rates, and sinking velocity of copepod fecal pellets: Direct measurements of ballasting by opal and calcite. *Limnology and Oceanography*. 53: 469–476. doi:10.4319/lo.2008.53.2.0469

Prairie, J., K. Ziervogel, C. Arnosti, R. Camassa, C. Falcon, S. Khatri, R. M. McLaughlin, B. L. White, and S. Yu. (2013) Delayed settling of marine snow at sharp density transitions driven by fluid entrainment and diffusion-limited retention. *Marine Ecology Progress Series*. 487: 185–200. doi:10.3354/meps10387

Reed, R. K., and J. D. Schumacher. (1986) Physical oceanography, In D.W. Hood and S.T. Zimmerman [eds.], The Gulf of Alaska: Physical environment and biological resources. NOAA, U.S. Department of Commerce.

Richardson, T. L. (2019) Mechanisms and pathways of small-phytoplankton export from the surface Ocean. *Annual Review of Marine Science*. 11: 57–74. doi:10.1146/annurev-marine-121916-063627

Richardson, T. L., and G. A. Jackson. (2007) Small phytoplankton and carbon export from the surface ocean. *Science*. (1979) 315: 838–840. doi:10.1126/science.ll33417

Royer, T. C., and W. J. Emery. (1987) Circulation in the Gulf of Alaska, 1981. Deep Sea Research 34: 1361–1377.

Sambrotto, R. N., and C. Lorenzen. (1987) Phytoplankton and primary production, p. 249–282. In D.W. Hood and T.S. Zimmerman [eds.], The Gulf of Alaska, physical environmental and biological resources. NOAA, U.S. Department of Commerce.

Sarkar, N., T. C. Royer, and C. E. Grosch. (2005) Hydrographic and mixed layer depth variability on the shelf in the northern Gulf of Alaska, 1974-1998. *Continental Shelf Research*. 25: 2147–2162. doi:10.1016/j.csr.2005.07.006

Siegel, D. A., K. O. Buesseler, S. C. Doney, S. F. Sailley, M. J. Behrenfeld, and P. W. Boyd. (2014) Global assessment of ocean carbon export by combining satellite observations and food-web models. *Global Biogeochemical Cycles*. 28: 181–196. doi:10.1002/2013GB004743

Silver, M. W., and K. W. Bruland. (1981) Differential feeding and fecal pellet composition of salps and pteropods, and the possible origin of the deep-water flora and olive-green "Cells." *Marine Biology*. 62: 263–273. doi:10.1007/BF00397693

Smetacek, V. S. (1985) Role of sinking in diatom life-history cycles: ecological, evolutionary and geological significance. *Marine Biology*. 84: 239–251. doi:10.1007/BF00392493

Stabeno, P. J., N. A. Bond, A. J. Hermann, N. B. Kachel, C. W. Mordy, and J. E. Overland. (2004) Meteorology and oceanography of the Northern Gulf of Alaska. *Continental Shelf Research*. 24: 859–897. doi:10.1016/j.csr.2004.02.007

Stemmann, L., G. A. Jackson, and G. Gorsky. (2004) A vertical model of particle size distributions and fluxes in the midwater column that includes biological and physical processes - Part II: Application to a three year survey in the NW Mediterranean Sea. *Deep-Sea Research I*. 51: 885–908. doi:10.1016/j.dsr.2004.03.002

Stokes, G. G. (1851) On the effect of the internal friction of fluids on the motion of pendulums. *Transactions of the Cambridge Philosophical Society*. Part II: 8–106.

Strom, S., and K. Fredrickson. (2020) Primary productivity estimates from NGA-LTER research cruises in the Gulf of Alaska, 2018-2020. Research Workspace. doi:10.24431/rw1k45b

Strom, S. L., M. A. Brainard, J. L. Holmes, and M. B. Olson. (2001) Phytoplankton blooms are strongly impacted by microzooplankton grazing in coastal North Pacific waters. *Marine Biology*. 138: 355–368.

Strom, S. L., K. A. Fredrickson, and K. J. Bright. (2016) Spring phytoplankton in the eastern coastal Gulf of Alaska: Photosynthesis and production during high and low bloom years. *Deep-Sea Research II*. 132: 107–121. doi:10.1016/j.dsr2.2015.05.003

Strom, S. L., E. L. Macri, and M. B. Olson. (2007) Microzooplankton grazing in the coastal Gulf of Alaska: Variations in top-down control of phytoplankton. *Limnology and Oceanography*. 52: 1480–1494. doi:10.4319/lo.2007.52.4.1480

Strom, S. L., M. B. Olson, E. L. Macri, and C. W. Mordy. (2006) Cross-shelf gradients in phytoplankton community structure, nutrient utilization, and growth rate in the coastal Gulf of Alaska. *Marine Ecology Progress Series*. 328: 75–92. doi:10.3354/meps328075

Stukel, M. R., H. Song, R. Goericke, and A. J. Miller. (2018) The role of subduction and gravitational sinking in particle export, carbon sequestration, and the remineralization length scale in the California Current Ecosystem. *Limnology and Oceanography*. 63: 363–383. doi:10.1002/lno.10636

Timothy, D. A., C. S. Wong, J. E. Barwell-Clarke, J. S. Page, L. A. White, and R. W. Macdonald. (2013) Climatology of sediment flux and composition in the subarctic northeast Pacific Ocean with biogeochemical implications. *Progress in Oceanography*. 116: 95–129. doi:10.1016/j.pocean.2013.06.017

Turner, J. S., J. L. Pretty, and A. M. P. McDonnell. (2017) Marine particles in the Gulf of Alaska shelf system: Spatial patterns and size distributions from in situ optics. *Continental Shelf Research*. 145: 13–20. doi:10.1016/j.csr.2017.07.002

Turner, J. T. (2015) Zooplankton fecal pellets, marine snow, phytodetritus and the ocean's biological pump. *Progress in Oceanography*. 130: 205–248. doi:10.1016/j.pocean.2014.08.005

Vaqué, D., E. Lara, J. M. Arrieta, J. Holding, E. L. Sa, I. E. Hendriks, A. Coello-Camba, M. Alvarez, S. Augsti, P. F. Wassmann, and C. M. Duarte. (2019) Warming and CO2 Enhance Arctic Heterotrophic Microbial Activity. *Frontiers in Microbiology*. 10: 1–13. doi:10.3389/fmicb.2019.00494

Waite, J. N., and F. J. Mueter. (2013) Spatial and temporal variability of chlorophyll-a concentrations in the coastal Gulf of Alaska, 1998-2011, using cloud-free reconstructions of SeaWiFS and MODIS-Aqua data. *Progress in Oceanography*. 116: 179–192. doi:10.1016/j.pocean.2013.07.006

Weber, T., J. A. Cram, S. W. Leung, T. DeVries, and C. Deutsch. (2016) Deep ocean nutrients imply large latitudinal variation in particle transfer efficiency. *Proceedings of the National Academy of Sciences*. 113: 8606–8611. doi:10.1073/pnas.1604414113

Weingartner, T. J., S. L. Danielson, and T. C. Royer. (2005) Freshwater variability and predictability in the Alaska Coastal Current. *Deep-Sea Research II*. 52: 169–191. doi:10.1016/j.dsr2.2004.09.030

Welschmeyer, N. A., S. Strom, R. Goericke, G. DiTullio, M. Belvin, and W. Petersen. (1993) Primary production in the subarctic Pacific Ocean: Project SUPER. *Progress in Oceanography*. 32: 101–135.

Williams, R. G., V. Roussenov, and M. J. Follows. (2006) Nutrient streams and their induction into the mixed layer. *Global Biogeochemical Cycles*. 20. doi:10.1029/2005GB002586

Wilson, S. E., D. K. Steinberg, and K. O. Buesseler. (2008) Changes in fecal pellet characteristics with depth as indicators of zooplankton repackaging of particles in the mesopelagic zone of the subtropical and subarctic North Pacific Ocean. *Deep-Sea Research II*. 55: 1636–1647. doi:10.1016/j.dsr2.2008.04.019

Yingling, N., T. B. Kelly, T. A. Shropshire, M. R. Landry, K. E. Selph, A. N. Knapp, S. A. Kranz, and M. R. Stukel. (2022) Taxon-specific phytoplankton growth, nutrient utilization and light limitation in the oligotrophic Gulf of Mexico. *Journal of Plankton Research*. 44: 656–676. doi:10.1093/plankt/fbab028

Chapter 3: High-resolution particle imaging in the Southern Ocean reveals export pathways

3.1 Abstract

Marine particles transfer carbon, nutrients, and trace elements into the deep ocean and play an essential role in altering the concentrations of these elements at all depths. The Southern Ocean plays a disproportionately large role in global biogeochemical cycles and climate; however, the large-scale, full-depth distributions of marine particles in this region remain poorly described. Using a CTD-mounted underwater imaging system, the Underwater Vision Profiler 5 (UVP5), we observed the depth-resolved concentrations and size distributions of large marine particles (i.e., 0.1 - 2.5 mm equivalent spherical diameter (ESD)) across two large-scale GO-SHIP repeat hydrography transects in the Pacific and African sectors of the Southern Ocean. Utilizing deep learning features and unsupervised clustering, 2.9 million images of particles were classified by type into 46 detrital categories within four super-categories (*i.e.*: fluffy aggregates, dense aggregates, fibers, feces) and 61 living categories within four super-categories (*i.e.:* crustaceans, rhizarians, gelatinous zooplankton, photosynthetic particles). Frontal zones retained particles produced by primary production and grazer distributions. Fluffy aggregates and grazers were most common near the surface during periods of high surface chlorophyll *a*, whereas in the 2-3 months after a bloom, grazers were located primarily in the mesopelagic and feces and dense aggregates were in high abundance in the bathypelagic. These results shed light on how frontal structures in the Southern Ocean influence patterns of particle export and remineralization in the mesopelagic with implications for how this influences global biogeochemical cycles.

3.2 Introduction

The Southern Ocean is an essential region for global carbon cycling in large part due to the unique physical features in this region (Gruber et al., 2019). The Southern Ocean flows clockwise around Antarctica and is characterized by longitudinal climatological fronts (Figure 3.1). Generally, oceanic fronts are known to create biological hot spots or areas with increased primary production, which can attract herbivores and carnivores (Ohman et al., 2012). The increased primary production near fronts is often attributed to increased nutrient flux to the euphotic zone due to the mixing at the front's boundary. Additionally, the Southern Ocean has areas of deep-water formation that can increase the ocean's ability to pump carbon away from

the air-sea interface and out of the mixed layer, i.e., the solubility pump (Sigman et al., 2010). Changes in the strength of the biological carbon pump in the Southern Ocean have been linked with changes in the glacier-interglacial cycle globally (Sarmiento & Gruber, 2006; Sigman & Boyle, 2000). Despite the importance of this region, biological mechanisms of carbon export, particularly into the deep ocean, remain under-sampled (Boyd et al., 2024; Sanders et al., 2016).

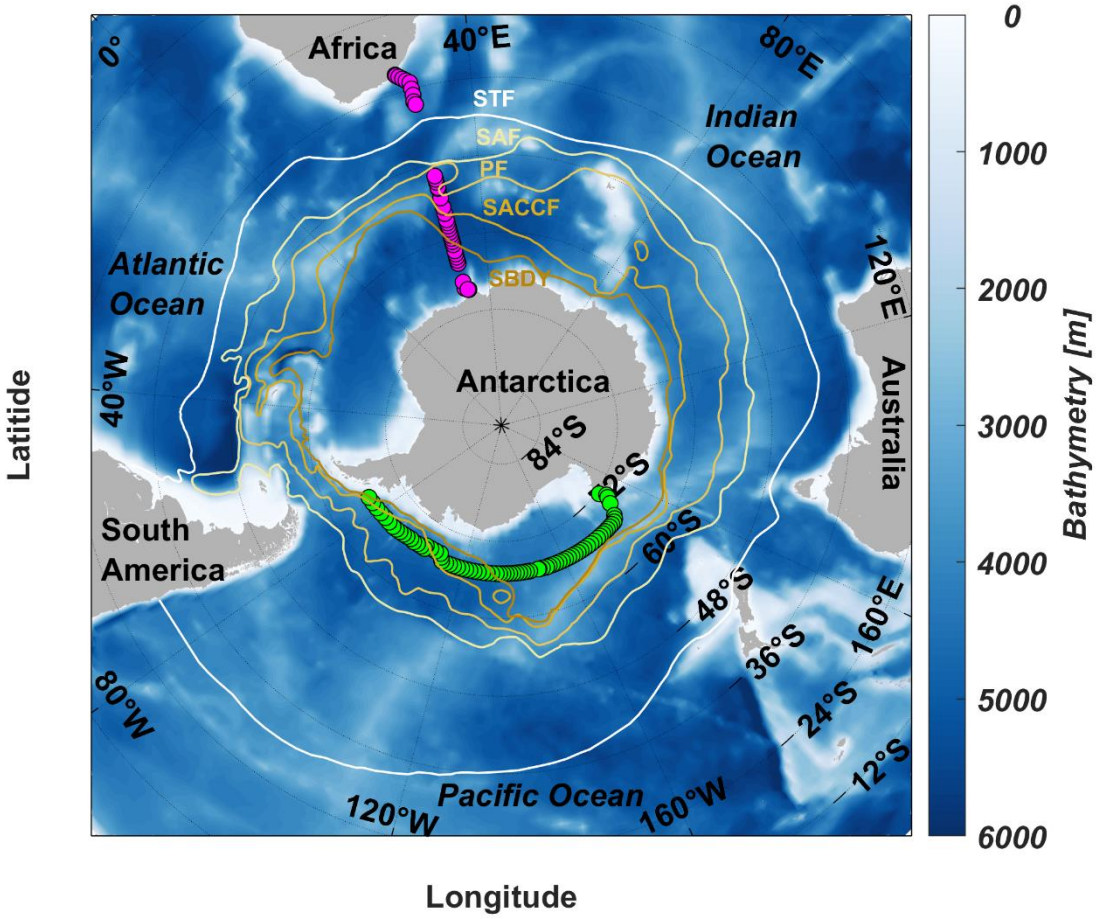

Figure 3.1: Study area. Sampling stations are shown from two U.S. GO-SHIP cruises: S04P (green), a latitudinal cruise (~ 67°S) in the Pacific sector of the Southern Ocean sampled during the austral fall of 2018, and I06S (magenta), a longitudinal cruise (~ 30°E) in the African sector of the Southern Ocean sampled during the austral fall of 2019. Frontal locations indicated (solid lines) are approximate locations from historical data. STF – Subtropical Front; SAF – Subantarctic Front; PF – Polar Front; SACCF – Southern Antarctic Circumpolar Current Front; SBDY – Southern Boundary.

The locations of fronts in the Southern Ocean are determined primarily by global thermohaline circulation and secondarily by bathymetry (Carter et al., 2008; Orsi et al., 1995; Venables et al., 2012). These fronts include the Southern Boundary (SBDY), the Southern Antarctic Circumpolar Current Front (SACCF), the Polar Front (PF), the Subantarctic Front (SAF), and the Subtropical Front (STF). Between the fronts are frontal zones such as the Subpolar Region, Southern Zone, Antarctic Zone, Polar Frontal Zone, and Subtropical Zone. Mixing water masses with different nutrient limitation characteristics at fronts can enhance primary production. High inorganic nitrogen concentration and low silica-to-nitrogen ratios, indicative of HNLC water, usually characterize the Southern and Antarctic Zones. As a result, chlorophyll concentrations and zooplankton biovolume are generally low (Pollard et al., 2002). Chlorophyll concentration and zooplankton biomass have been observed to be relatively higher in the Southern Zone than in the more northern Antarctic Zone. The Polar Frontal Zone is usually characterized by HNLC waters with iron limitation (Mishra et al., 2020). However, iron is more abundant in the Polar Frontal Zone than in the Southern and Antarctic Zones (Mishra et al., 2020), which often results in moderate phytoplankton blooms of coccolithophorids, cyanobacteria, flagellates, and pennate diatoms and low biomass of grazers (i.e., copepods, appendicularians, pteropods, and salps) (Halfter et al., 2020). These conditions often produce high export efficiency (Halfter et al., 2020). Moving north, the Subantarctic Frontal Zone is generally low in phytoplankton and grazer biomass and represents a transition between HNLC water in the Polar Frontal Zone and nitrate-limited water in the Subtropical Frontal Zone. The Subtropical Frontal Zone usually has small-celled flagellates and prokaryotes due to low nitrate, phosphate, and silicate concentrations (Mishra et al., 2020) and a much lower concentration of grazers than the Polar Frontal Zone, mainly consisting of *Calanus* copepods and *Oithona similis* (Mishra et al., 2020). The carbon attenuation processes in the meso- and bathypelagic zones are vital to the fate of particles but have been difficult to sample with traditional tools (Halfter et al., 2020). We need more observations to constrain the extent to which particles are exported deep into the mesopelagic and bathypelagic and the role that physical circulation and biological communities play in controlling this export (Halfter et al., 2020).

Marine particle size has long been used as the primary metric to determine particle carbon content (Alldredge, 1998), sinking velocity (Lerman et al., 1974; Stokes, 1851), and thus, carbon flux (Guidi et al., 2008; Iversen & Ploug, 2010; McDonnell & Buesseler, 2012). However, rather

than size, marine particle morphology is used to determine the particle's type and, thus, its sources and sinks (Iversen, 2023; Turner, 2015). Particle type informs our expectations about the mechanisms by which a particle can move in the ocean; for example, aggregates sink passively, and fecal pellets both sink passively and can be transported actively through diel vertical migration by zooplankton (Bianchi et al., 2013; Boyd et al., 2019). Furthermore, different particle types have distinct mineral content, complexities of shape, densities, and porosities, all of which affect size-specific carbon content (Iversen & Lampitt, 2020; De La Rocha & Passow, 2007), sinking speed (Alldredge & Gotschalk, 1989; Kiørboe, 2001; Ploug et al., 2008), and remineralization rates (Armstrong et al., 2002; Goldthwait et al., 2005; Ploug et al., 2008; Turner, 2015). There is ample evidence that including metrics of marine particle morphology is necessary to reduce the uncertainty around the strength and efficiency of the biological carbon pump (Iversen & Lampitt, 2020; Laurenceau-Cornec et al., 2020). Unfortunately, measuring marine particle morphology over broad spatial scales with traditional tools like backscatter, beam transmission, sediment traps, and bulk POC measurements has been challenging if not impossible.

In-situ imaging technologies, like the Underwater Vision Profiler 5 (UVP5), sample delicate marine snow particles and living zooplankton without damaging them (Lombard et al., 2019; Picheral et al., 2010). Unfortunately, classifying these images is also challenging due to the requirement of detailed taxonomy knowledge and the time associated with sorting millions of images. When classifying living zooplankton images, scientists use standard techniques of morphology and taxonomy (Stemmann & Boss, 2012); yet, detritus makes up most images, often up to 90%, and is difficult to classify into meaningfully different categories. As such, detritus is commonly only sorted into one or two categories. This makes for a poor training set, as detritus has much more morphological diversity than living taxa. Fortunately, the increasing computational power of personal computing devices and improvements in deep learning technology allow particles to be categorized into more morphological categories with greater accuracy and speed than previously possible (Irisson et al., 2022). Using unsupervised clustering within a convolutional neural network framework allows images to be clustered into data-driven categories much more quickly and accurately than traditional random forest prediction and manual validation (Schröder et al., 2020). Schroder and colleagues sorted 1.2 million images into 280 categories, dozens of which are ecologically distinct detritus categories, using the

MorphoCluster technique (2020). In another study conducted as Arctic sea ice retreated, marine snow particles were categorized into five ecologically meaningful functional morphotypes by clustering based on 24 morphological characteristics of each marine snow particle, which were demonstrated to behave differently both spatially and temporally as the sea ice retreated (Trudnowska et al., 2021). These new techniques allow us to quickly and accurately classify marine snow into ecologically meaningful categories. Therefore, these new techniques are critical for understanding the role of particle morphology in the biological carbon pump.

In this study, we used the U.S. Global Ocean Ship-based Hydrographic Investigations Program (GO-SHIP) to sample and classify marine snow and living particles into 105 ecologically meaningful categories on an ocean basin-wide, full-depth scale. We imaged marine particles with a UVP5 High-Definition unit on two U.S. GO-SHIP Cruises in 2018 and 2019 in the Pacific and African sectors of the Southern Ocean, respectively. We aim to characterize the role of climatological fronts and water masses in determining marine particle communities. We also investigate the role of zooplankton in determining marine particle community structure. This study represents the first ocean basin-wide, full-depth classification of marine detrital particles and the first description of living zooplankton abundance along a U.S. GO-SHIP transect.

3.3 Methods

3.3.1 Study System

Data from this study were collected with the U.S. GO-SHIP. They were collected on the S04P cruise from March to May 2018 on the R/V Palmer and the I06S cruise from April to May 2019 on the R/V Thompson (Table 3.1, Figure 3.1). The S04P cruise was a longitudinal cruise from Oates Land to the Western Antarctic Peninsula. I06S was a latitudinal cruise from Port Elizabeth, South Africa, south to Antarctica. A portion of the transect line from 44°S to 53°S went unsampled due to mechanical issues.

The CTD unit consisted of a Seabird SBE911plus coupled with a WetLabs fluorometer. The high-definition UVP5 SN-207 attached to the CTD rosette package sampled the water column down to 6000 m in tandem with the other sensors on the CTD. UVP5 SN-207 images a water volume of ~ 0.88 L at up to 20 Hz, capturing particles 0.06 – 27 mm in ESD within each image (Picheral et al., 2010).

Table 3.1: Cruise and image metadata.

Cruise Name	Date Range	Latitude Range	Longitude Range	Number of Stations	Number of Images
S04P	March 13 – May 9, 2018	59 S – 76 S	159 E – 74 W	113	2,105,986
I06S	April 16 – May 11, 2019	33 S – 69 S	28 E – 32 E	44	774,695

3.3.2 Environmental Conditions

We used the previously defined climatological fronts (Orsi et al., 1995), commonly used in other studies (Sow et al., 2022). It should be noted that the locations of these climatological fronts, as used in this study, are the approximate locations only and that frontal boundaries are often discontinuous and challenging to determine from water mass properties alone (Chapman et al., 2020). From south to north, the fronts are the Southern Boundary (SBDY), the Southern Antarctic Circumpolar Current Front (SACCF), the Polar Front (PF), the Subantarctic Front (SAF), and the Subtropical Front (STF). From south to north, the frontal zones are the Subpolar Region, Southern Zone, Antarctic Zone, Polar Frontal Zone, and Subtropical Zone (Figure 3.1).

Daily sea-surface height anomalies (SSHa) from each cruise midpoint were taken from a 0.25-degree resolution Level 4 reprocessed product (Copernicus Climate Service, 2023). Monthly averaged satellite-derived chlorophyll concentrations were taken from the National Aeronautics and Space Administration (NASA) Aqua-MODIS's Level 3 and Level 4 Browser at a 4 km resolution using the OCI Algorithm in mg m^{-3} (NASA Goddard Space Flight Center, 2014). We selected March 2018 for the Pacific Sector cruise and April 2019 for the African Sector cruise to balance having the most overlapping days with the cruise and the best data coverage.

We used previously defined water mass endmembers (Pardo et al., 2012) that have been commonly used in other studies (Samanta et al., 2023; Sow et al., 2022) to classify the water masses used in this study. See Appendix B for the endmember definitions and water mass classification used in this study (Figure B.1). We classified seven water masses: Shelf Water (SW), Antarctic Bottom Water (AABW), Lower Circumpolar Deep Water (LCDW), Upper Circumpolar Deep Water (UCDW), Antarctic Surface Water (AASW), Subantarctic Mode Water/Antarctic Intermediate Water (SAMW/AAIW), and Subantarctic Surface Water (SASW).

3.3.3 Particle Data Processing

Mixed processing mode was utilized on the UVP5 unit, counting and sizing all identified particles and saving JPEG images of particles larger than 500 µm ESD. Data from the downcasts was processed using the Zooprocess Version 7.39 software and published to the Ecotaxa website (https://ecotaxa.obs-vlfr.fr/prj/9566) (Picheral et al., 2017). We calculated particle concentrations and size distributions throughout the whole water column. A power law function was used to convert pixel area to metric area (see Picheral et al., 2010 for details). The remaining particles were grouped into 5 m depth bins and one of 19 logarithmically spaced size bins based on their ESD. We calculated depth-specific particle abundance by dividing the number of particles per depth bin by the volume of water imaged per depth bin (#/L). We assumed a spherical shape for every particle to convert ESD to biovolume (µl/l). The slope of the particle size distribution was calculated by plotting a histogram of the number of particles in each size bin and performing a linear fit to the number of particles (y-axis) by mid-point of the size bin (x-axis). The slope of this liner fit is the slope of the particle size distribution. Transect plots of particle abundance, biovolume, and slope of particle size distribution were created in Matlab R2019a.

3.3.4 UVP Image Data Processing

The gray-scale JPEG images of particles larger than ~ 1 mm were used to identify the particle's type. We used the Morphocluster protocol to determine particle type for the 2.8 million UVP images that are a part of these two datasets (Schröder et al., 2020). We seeded our first Morphocluster run with previously named clusters (Schröder et al., 2020). After a few rounds of clustering and growing, 91% of the images were classified into 74 hierarchically arranged and named clusters. When possible, these were imported to Ecotaxa using existing categories, and each category was visually inspected. Many new living categories were added to facilitate finer-scale classification of the living particles. Each category was viewed from largest to smallest and then darkest to lightest. Images in the upper and lower size and average grayscale value within each grouping were validated manually or reclassified as necessary until the images had less than 5% error per page. Then, the images were sorted randomly, and a thousand were viewed to determine the overall error. When the overall error was less than 5%, the category was considered "clean." If the misidentifications exceeded 5%, we performed more manual validation and rechecked the category, as described above. Each image was visually inspected for the living categories, and these categories had as close to 0% error as possible. When all

categories were considered clean, we used the random forest classifier on Ecotaxa and the validated images to predict the remaining images (9% of total images) into one of the 61 living and 46 detritus categories. The error of the final predictions of the 9% of total images was not analyzed; however, it is assumed not to contribute substantially to the overall error rate of the classifications because it represents such a small percentage of the images.

We combined many categories into eight super-categories for plotting in this manuscript: fluffy aggregates, dense aggregates, fibers, fecal pellets, photosynthetic particles, crustaceans, rhizarians, and gelatinous zooplankton (Figure 3.2). Every Ecotaxa category and, when relevant, its super-category, is listed (Table B.1).

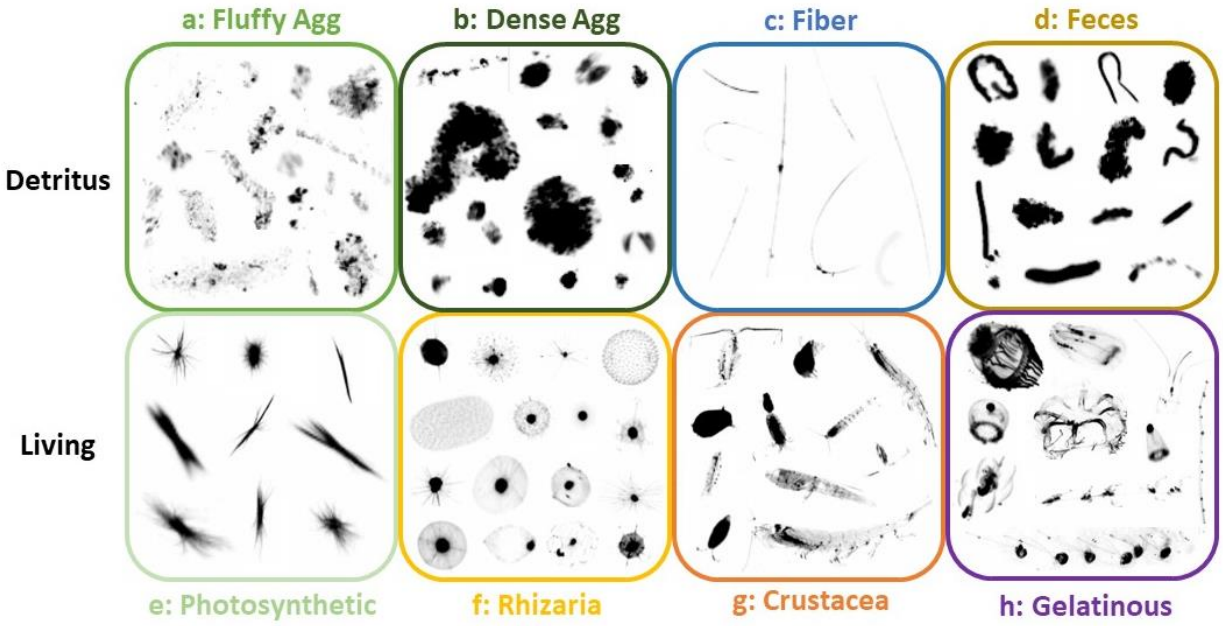

Figure 3.2: Image classification. Example images are classified into eight super-categories, each representing a group of multiple categories of particles. Detritus super-categories include (a) fluffy aggregate: 13 categories, (b) dense aggregate: 8 categories, (c) fiber: 4 categories, and (d) feces: 16 categories. Living super-categories include (e) photosynthetic particles: 4 categories, (f) rhizarians: 25 categories, (g) crustaceans: 8 categories, and (h) gelatinous particles: 11 categories.

3.3.5 Statistical Analysis

A principal component analysis (PCA) was performed to compare marine particle communities in different water masses and frontal zones. The covariance matrix was calculated using the function *PCA* in the FactoMineR package in R using the default setting with variables scaled to unit variance. Each sample in this analysis is a marine particle community that represents the abundance of each of the eight particle super-categories in each CTD cast

averaged over the following depth bins: 0 – 50 m, 50 – 100 m, 100 – 200 m, 200 – 500 m, 500 – 1000 m, 1000 – 2000 m, 2000 – 3000 m, 3000 – 4000 m, 4000 – 5000 m, and 5000 – 6000 m. Depth and latitude or longitude (depending on the ordination of the cruise transect) were plotted as quantitative supplementary variables to see how those variables correlate with the different marine particle types.

3.4 Results and Discussion

3.4.1 Environmental Conditions

Our cruises crossed all five climatological fronts (Figure 3.3). Although the Pacific Sector cruise mainly sampled along latitude 67°S, we did cross a few climatological fronts as they meandered across different latitudes (Figures 3.3a – 3.3b). The western half of the cruise was in the Subpolar Region. At station 81, we crossed the Southern Boundary into the Southern Zone. Between stations 97 and 102, we crossed the Southern Antarctic Circumpolar Front into the Antarctic Zone, then back into the Southern Zone at Station 118. The African Sector cruise was mainly sampled perpendicular to the climatological fronts (Figures 3.3c – 3.3d). The Southern Boundary was located between stations 21 and 23, and the Southern Antarctic Circumpolar Front at station 31. The Polar Front exhibits a meander around our transect line. We reasoned that this front could be located anywhere from the southernmost to the northernmost extent of the meander (at stations 34 and 45, respectively). We compared these locations with in-situ Sigma-t (i.e., potential density anomaly relative to 0 dbar). We found a sharp deepening of isopycnals around the southernmost extent of the Polar Front (Figure 3.4c and 3.4d). As such, we determined the southernmost extent of the Polar Front meander at Station 34 to be the location of the Polar Front for our analyses. The Subantarctic and Subtropical Fronts were located during a section of the transect that was unsampled due to mechanical issues. Station 46 and north were considered within the Subtropical Zone.

The daily SSHa was relatively stable throughout the sampling extent of both cruises (Figures 3.3a and 3.3c). The biggest anticyclonic eddy was located just north of the Subtropical Front during the African Sector cruise, however, this was in the region of the transect that went unsampled (Figure 3.3c). We checked the daily variability of SSHa and found the SSHa from the dates selected in Figures 3.3a and 3.3c were representative of the whole duration of both cruises.

We conclude that mesoscale eddies did not play a substantial role in shaping the physical environment in our study.

In the Pacific Sector, there was elevated surface chlorophyll a in the Southern Zone between the Southern Boundary and the Southern Antarctic Circumpolar Current Front, indicating that a phytoplankton bloom was occurring in this frontal zone at the time of sampling (Figure 3.3b). The rest of the transect had relatively low surface chlorophyll *a* concentrations. In the African Sector, clouds obscured surface chlorophyll a concentrations south of the Southern Antarctic Circumpolar Current Front in April 2019 (Figure 3.3d). There was a consistent band of high surface chlorophyll *a* waters at the Subtropical Front. Unfortunately, this region was unsampled on this cruise due to mechanical issues. The stations sampled on this cruise with corresponding surface chlorophyll *a* data had relatively low concentrations in April 2019. However, January and February 2019 show elevated surface chlorophyll a in the Southern Zone, about 2-3 months before the cruise.

3.4.2 Particle Abundance

In the Pacific Sector (SO4P) cruise, three water masses were identified with a similar pattern across all frontal zones (Figure 3.4a). Antarctic Surface Water was identified from the surface to approximately 250 m depth. The Lower Circumpolar Deep Water was identified from around 250 – 2000 m, deepening slightly on the eastern side of the transect. The Antarctic Bottom Water was identified from around 2000 m to the seafloor. Six water masses were identified in the African Sector cruise (IO6S) (Figure 3.4b). The southern portion of this region in the Subpolar Region, Southern Zone, and Antarctic Zone had a similar pattern in water masses as the Pacific Sector Cruise. However, the lower depth limits of the Antarctic Surface Water and Upper Circumpolar Deep Water are slightly deeper in the southernmost Subpolar Region and gradually shoal in the more northern Antarctic Zone. A small amount of Shelf Water was identified on top of the seafloor at the Southern Boundary. The Polar Frontal Zone had Upper Circumpolar Deep Water from the surface to about 200 m on top of the Antarctic Surface Water, Lower Circumpolar Deep Water, and Antarctic Bottom Water, which all extended down to slightly deeper depths than south of the Polar Frontal Zone. In the Subtropical Zone, we identified Subantarctic Surface Water from the surface to about 300 m, Subantarctic Mode Water/Antarctic Intermediate Water from about 300 – 900 m, Upper Circumpolar Deep Water from about 900 –

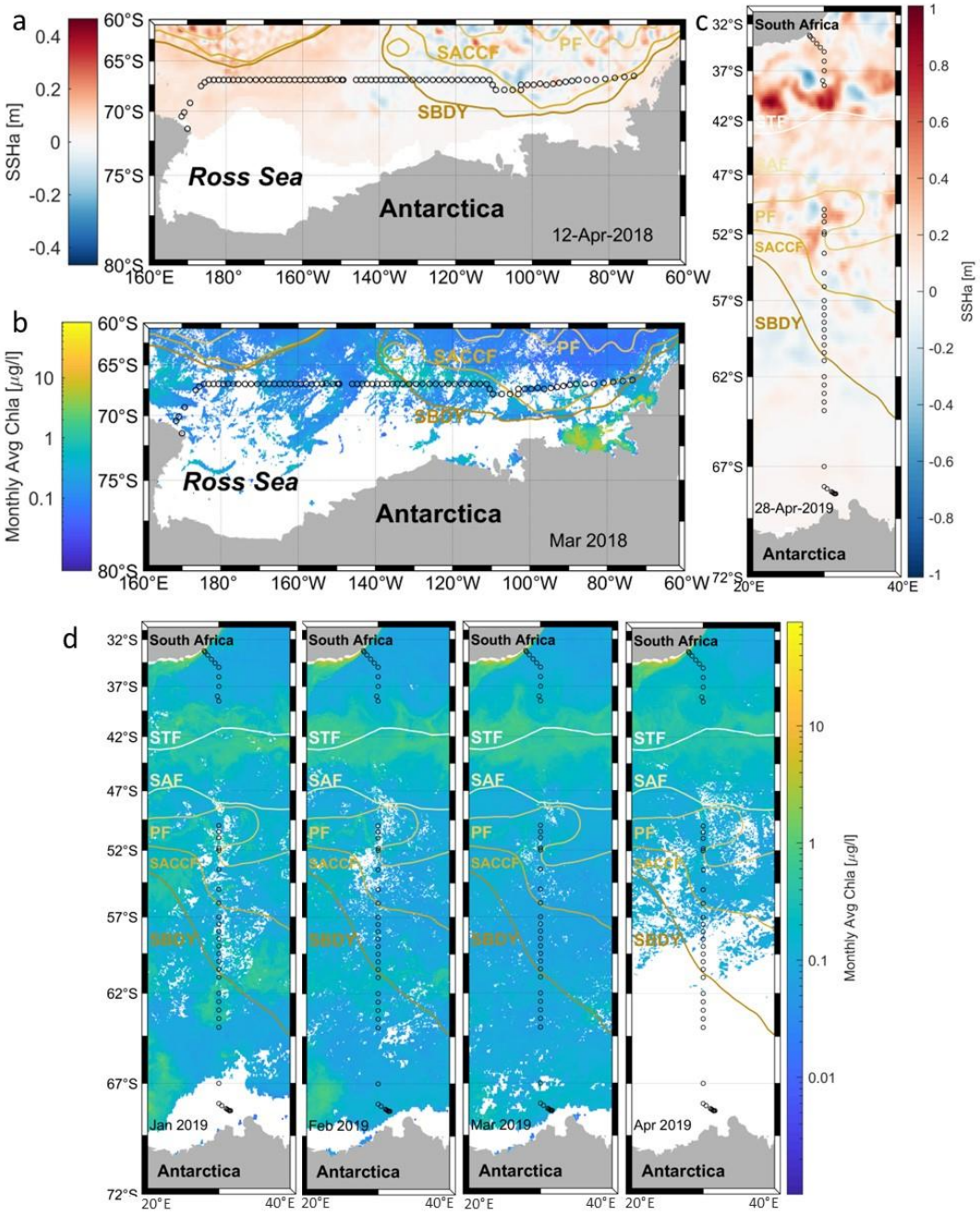

Figure 3.3: Climatology of the study area. Daily sea-surface height anomalies (SSHa) at a 0.25-degree resolution are shown in the shading on (a) 12 April 2018, the cruise midpoint for the transect in the Pacific sector of the Southern Ocean, and on (c) 28 April 2019, the cruise midpoint for the transect in the African sector of the Southern Ocean. The monthly averaged Aqua MODIS SSChl-a concentrations are shown in the shadings (b) for the Pacific sector of the Southern Ocean transect in March 2018 and (d) for the African sector of the Southern Ocean transect in January, February, March, and April 2019. Frontal locations indicated (solid lines) are approximate. STF – Subtropical Front; SAF – Subantarctic Front; PF – Polar Front; SACCF – Southern Antarctic Circumpolar Current Front; SBDY – Southern Boundary.

2000 m, and Lower Circumpolar Deep Water from about 2000 m to the seafloor. These patterns match what has been previously described for these regions (Talley et al., 2011).

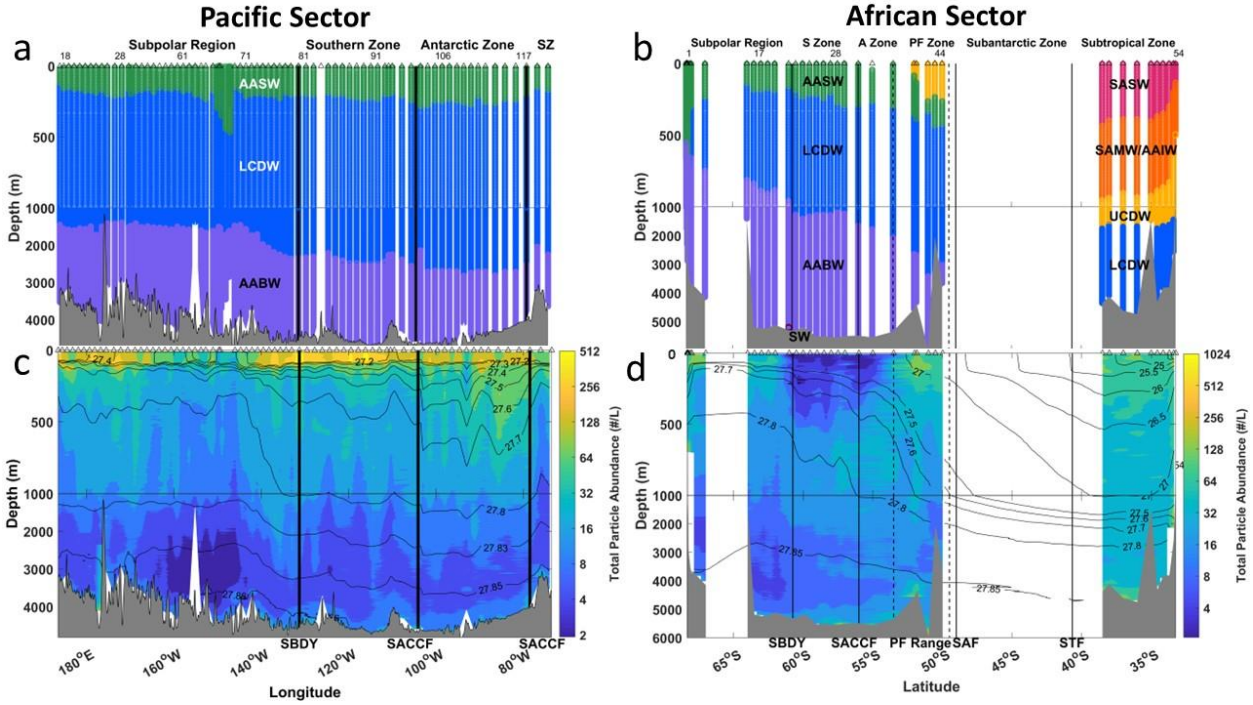

Figure 3.4: Spatial distributions of general water and particle properties. (a) Section plots of water mass for the Pacific Sector cruise (S04P) and (b) African Sector cruise (I06S). (c) Total particle abundance in #/L for the Pacific Sector cruise (S04P) and (d) African Sector cruise (I06S). Water masses and their approximate delineations are labeled in white or black as needed for readability: AASW- Antarctic Surface Water (green); LCDW - Lower Circumpolar Deep Water (blue); AABW - Antarctic Bottom Water (purple); SASW - Subantarctic Surface Water (pink); SAMW - Subantarctic Mode Water (orange); AAIW - Antarctic Intermediate Water (orange); UCDW - Upper Circumpolar Deep Water (yellow); SW - Shelf Water (maroon). Sigma-t is shown in black contour lines on the lower panels. Climatological frontal regions are marked on the top: Subpolar Region; SZ/S Zone – Southern Zone; A Zone – Antarctic Zone; PF Zone – Polar Frontal Zone; Subantarctic Zone; and Subtropical Zone. Climatological frontal zones are marked with vertical black lines and labeled on the bottom, as defined in Figures 3.1 and 3.3.

The location of fronts and patterns in the isopycnals correspond with patterns in total particle abundance in both cruises. Isopycnals generally deepen at fronts moving from south to north in both cruises. Typically, particle abundance was highest at the surface in the Pacific Sector cruise and decreased with depth (Figure 3.4), with a thin nepheloid layer at the seafloor (based on elevated particle abundance). The fronts appeared to separate some distinct patterns in particle abundance. For example, total particle abundance was highest at the surface in the Southern

Zone during this cruise. Patterns in particle abundance also correlated with patterns in isopycnals. Deepening of isopycnals, such as that observed just west of the Southern Boundary, corresponded with elevated particle abundance from 1000 – 3000 m. Additionally, two instances of shoaling deep isopycnals in the Southern Zone correspond with increased particle attenuation and relatively lower particle abundance around 500 – 2000 m. In the African Sector cruise (IO6S), fronts separated distinct patterns in marine particle abundance associated with latitude shifts. The Subpolar Region on IO6S looks very similar to the Subpolar Region on the S04P cruise, with a high abundance at the surface that decreases over depth. This is strongly contrasted with the Southern and Antarctic Zones, which had the lowest particle abundance at the surface and a mesopelagic particle maximum from about 500 – 2000 m, which decreased to an intermediate value below 2000 m and a thick nepheloid layer at the seafloor. The Polar Frontal Zone had a high abundance at the surface with much lower attenuation than found in the Subpolar Region. High particle abundance was observed to the seafloor in the Polar Frontal Zone, potentially indicating high export. The Subtropical Region had the highest abundance of particles with the lowest attenuation rate and the thickest nepheloid layer. Although abundant, the particles in the Subtropical region were smaller than those found to the south (Figure B.2), which is typical for lower latitude regions (Kiko et al., 2022).

3.4.3 Particle Abundance by Type

Large particles greater than about 1 mm were classified by morphology and presented in 8 super-categories. Fluffy aggregates were the most numerous particle type in the Pacific Sector (SO4P) cruise, with the highest observed abundance of 6523 fluffy aggregates m^{-3} (Figure 3.5a). Their distribution was similar to total particle abundance but differed in a few notable areas. The western half of the Subpolar Region had high fluffy aggregate abundance at the surface that decreased slightly over depth; there was higher particle attenuation for total particles (Figure 3.4c). This indicates that fluffy aggregates may be preferentially exported in this sub-region. The eastern half of the Subpolar region showed low fluffy aggregate abundance at the surface and a mesopelagic fluffy aggregate abundance maximum, which decreased in the bathypelagic zone. Fluffy aggregates had the highest abundance at the surface of the Southern Zone, which also had high chlorophyll *a* and the highest total particle abundance. The majority of these particles were fluffy aggregates. Similar to total particle abundance, there was strong attenuation over depth of fluffy aggregates in the Southern Zone, as expected for marine particles that are formed at the

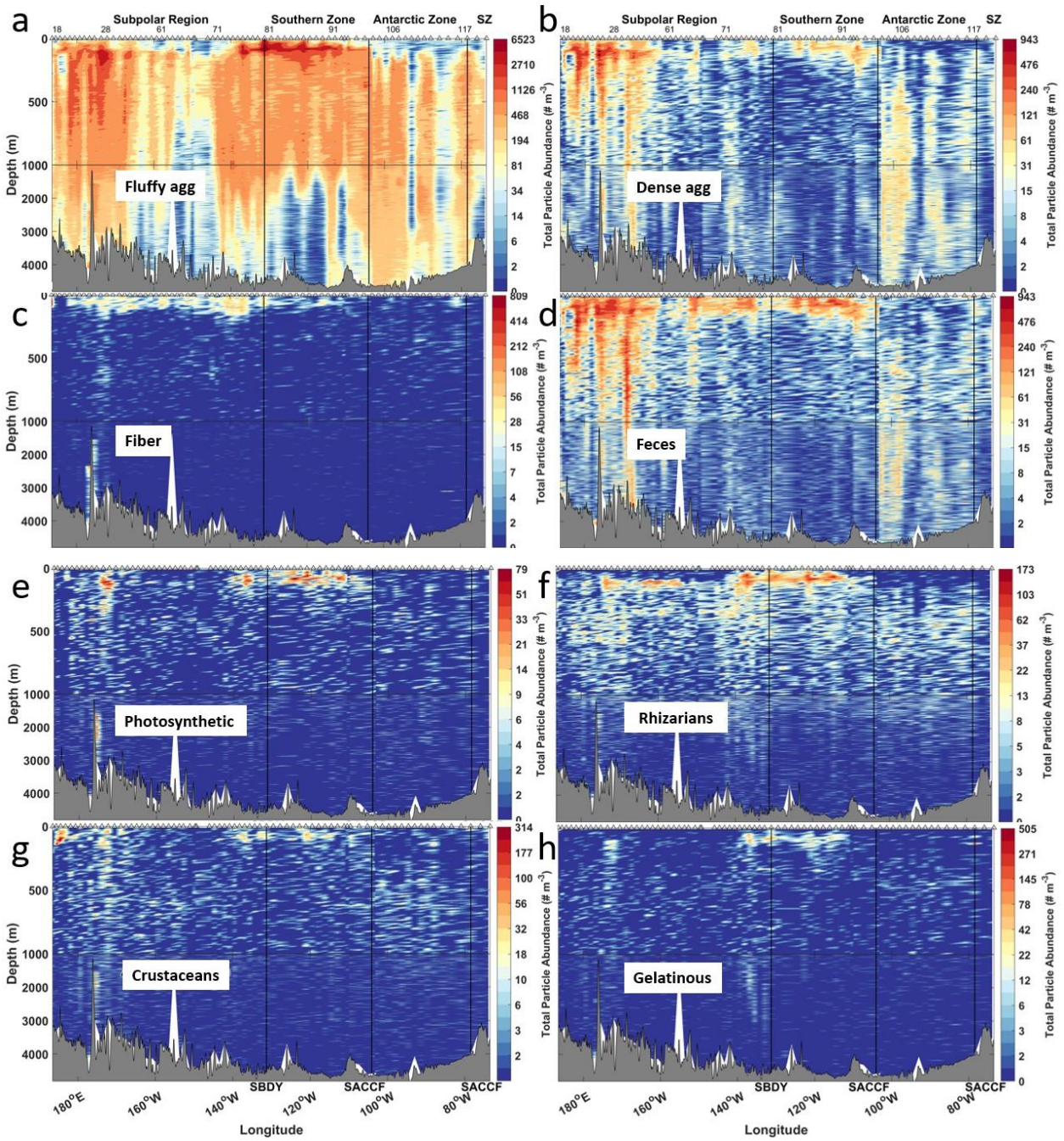

Figure 3.5: Spatial distribution of particles by particle type in the Pacific sector of the Southern Ocean (S04P). Section plots of the concentration of detrital particles over depth: (a) fluffy aggregates, (b) dense aggregates, (c) fibers, and (d) feces. Section plots of the concentration of living (e) photosynthetic particles, (f) rhizarians, (g) crustaceans, and (h) gelatinous zooplankton are shown over depth. Solid and dashed black vertical lines indicate the approximate locations of fronts displayed in Figures 3.1 and 3.3 labeled on the bottom. Locations of samples are marked on the top with black triangles.

surface and then degraded or disaggregated as they sink (Buesseler et al., 2007; Iversen, 2023). The Antarctic Zone had the most substantial difference between patterns in fluffy aggregate abundance and total particle abundance. There was very low abundance of fluffy aggregates in the surface of the Antarctic Zone. There was a strong banding effect where most of the stations in this region had moderate abundance of fluffy aggregate in the mesopelagic, which continued to the seafloor, and a few stations or small groups of stations that created bands of low particle abundance in the mesopelagic, which also continued to the seafloor. These bands of lower fluffy aggregate abundance align with observations of the deepening of isopycnals (Figure 3.4c). The deepening of isopycnals is typically associated with enhanced particle export, as the effects of the biological gravitational pump are enhanced by the physical pumps (i.e., eddy-subduction pump and mixed-layer pump) (Boyd et al., 2019). However, we observed depressed particle export rather than enhanced, suggesting that physical aggregation does not always act as expected. This could be a sign of localized downwelling or subduction and could reduce nutrient introduction at the surface, resulting in lower particle production (Gaube et al., 2014). Overall, there was much higher abundance of fluffy aggregates below 1000 m in the Antarctic Zone than in the Southern Zone.

Dense aggregates and feces had nearly identical overall abundances and patterns over the Pacific Sector cruise (Figures 3.5b and 3.5d). The highest observed abundance of dense aggregates and feces was the same: 943 particles m^{-3}. The patterns of abundance for dense aggregates and feces were similar to fluffy aggregates but at a lower magnitude and with a patchier distribution. Dense aggregates and feces appear to attenuate over depth at a similar rate as fluffy aggregates. Notably, dense aggregates and feces were in high abundance at the surface of the Subpolar Region and Southern Zone. There was low attenuation in the Subpolar Region with areas of relatively high abundance down to the seafloor. There was strong attenuation in the Southern Zone and a generally low abundance of dense aggregates and feces in the mesopelagic and bathypelagic. The Antarctic Zone also had a very low abundance of dense aggregates and feces on the surface with a similar banding pattern of moderate to low abundance through the mesopelagic and bathypelagic zones. The similarities between dense aggregates and feces lead us to question whether we can distinguish these two categories using UVP images. We posit that particles classified as dense aggregates may be partially degraded fecal pellets.

Fibers were primarily located near the surface of the Subpolar Region and Southern Zone in the Pacific Sector with the highest observed abundance of 809 fibers m^{-3} (Figure 3.5c). Homogenously-distributed small patches of fibers were located throughout the mesopelagic and bathypelagic zones in all frontal regions. The high abundance of fibers in the surface water indicates that they may be long chains of living diatoms at the surface, as previously observed with plankton imaging instruments (Ohman & Browman, 2019). The patchy distribution of fibers in the mesopelagic and bathypelagic could be dead or dying diatom chains that have sunk out of the euphotic zone. They also could be, in part, composed of non-organic fibers, such as microplastics or organic fibers (Suaria et al., 2020).

All living plankton super-categories had lower abundances than all detrital particle super-category abundances (Figure 3.5). Images of photosynthetic plankton had highest abundance near the surface, up to 79 m^{-3} (Figure 3.5e), especially in the Subpolar Region and Southern Zone. However, they had the lowest abundance of common particle types. The photosynthetic plankton identified consisted mostly of large colonial cyanobacteria *Trichodesmium* (Figure 3.2e). *Trichodesmium* are mostly present between 20°S and 20°N in the Pacific Ocean and should not be present in this transect or only in very low abundances, as observed (Westberry & Siegel, 2006). The UVP will not image the vast majority of photosynthetic plankton because they are much smaller than the ~1 mm lower limit of particle images saved by the UVP. Patterns in rhizarian distribution (Figure 3.5f) were similar to the patterns observed for fluffy aggregates (Figure 3.5a). For example, similar to fluffy aggregate abundances, rhizarians were in highest abundance at the surface of the Southern Zone, and associated with higher photosynthetic plankton during the likely bloom event. Crustaceans (Figure 3.5g) also had a high abundance at the surface of the Southern Zone but were higher in abundance in the mesopelagic than at the surface in the Antarctic Zone. Crustaceans (Figure 3.5g) and gelatinous zooplankton (Figure 3.5h) had a similar pattern to rhizarians, where the highest abundance was observed at the Southern Zone's surface and the Antarctic Zone's mesopelagic. It is likely we are underestimating the true abundance of larger zooplankton like crustaceans and gelatinous zooplankton. When plankton are in low abundance, we are likely to disproportionately under-sample it because the UVP5 only images about 100 L for each 5 m bin at a typical CTD downcast speed. This is relatively high for imaging systems; however, it is much less than a typical zooplankton net samples (Lombard et al., 2019; Romagnan et al., 2016). Additionally,

relatively mobile zooplankton, like crustaceans, avoid lights, even potentially the red lights used by the UVP5 that are selected to minimize avoidance behavior (Geoffroy et al., 2021). These patterns of living particles show how bloom conditions support the succession of a higher abundance and diversity of planktonic grazers and predators in the surface where numerous particles are being created (Behrenfeld et al., 2021; Romagnan et al., 2015). In non-bloom conditions, those grazers and predators are at lower abundance and are more likely to be deeper in the mesopelagic zone than the surface. Depth-resolved observations of zooplankton are rare, as most zooplankton are sampled with nets and integrated over the upper 200 - 1000 m (Moriarty et al., 2013). Certain rhizarian taxa, such as Tuscaroridae, Cannosphaeridae, Aulacanthidae, and Phaeodaria, have been shown to have a vertical depth niche of 300 – 500 m (Biard & Ohman, 2020; Drago et al., 2022). However, depth niches below 500 m have not been tested (Biard & Ohman, 2020). Another study looked at depth partitioning of various taxa of rhizarians as well as crustaceans, Molluscs, and cnidarians; however, this study only tested depth niches from 0 – 500 m (Drago et al., 2022). In this study, some crustacean and specific rhizarian taxa were more abundant from 200 – 500 m than in the upper 200 m (Figures 3.5f and 3.5g).

A portion of the crustaceans observed in the mesopelagic zone could be inactive. Some high-latitude zooplankton perform seasonal migrations, or diapause, to reserve energy during the food-poor winter season (Baumgartner & Tarrant, 2017). These seasonal migrators store lipid energy reserves during the productive summer, then respire and burn off that energy through respiration at depth during the winter. This is called the “seasonal lipid pump," one of the active carbon pumps in the biological carbon pump (Boyd et al., 2019). This life history strategy is much less common in the Southern Ocean than in the Arctic (Baumgartner & Tarrant, 2017). In the Southern Ocean, the copepods *Calanoids acutus* and possibly *Ctenocalanus citer* undergo seasonal diapause at depth (Atkinson et al., 2012; Atkinson, 1998). They are epipelagic and herbivorous in the summer, reproduce, and then enter diapause around March, migrating to between 500 and 1500 m during the winter until around November (Atkinson et al., 1997). *Calanoids acutus* are commonly observed in the Antarctic Zone and south and generally increase in abundance at higher latitudes (Atkinson et al., 1997). Omnivore and detritivore copepods are much less likely to diapause in the Southern Ocean (Atkinson, 1998). Other taxa of zooplankton also perform diapause in the Southern Ocean. Around March, several species of chaetognaths and salps diapause out of the upper 200 m and overwinter to below 250 m (Atkinson et al.,

2012). This study occurred from March to May, so diapausing taxa are likely to be overwintering in the mesopelagic zone during this study.

The crustaceans and other zooplankton observed in the mesopelagic zone could also be migrating daily to the euphotic zone to eat. The Southern Ocean is not often considered a region with much diel vertical migration, as this type of daily migration is usually tied to a daily light/dark cycle common at lower latitudes (Conroy et al., 2020). Diel migrators come up to the surface at night when it is dark, and there is a lower risk of predation to eat and migrate below the euphotic zone during the day to escape predation and reserve energy by resting in cooler water (Steinberg & Landry, 2017). Despite near or complete 24 hours of daylight in the summer, some zooplankton species perform diel-vertical migration during the Austral Summer in the Southern Ocean (Conroy et al., 2020). South of 65°S, diel vertical migration is less common (Pinkerton et al., 2010). This study occurred in the Austral Fall, so diel vertical migration should be more common and occur to deeper depths (Conroy et al., 2020). Most previously observed daily vertical migration is relatively shallow, mostly occurring within the upper 200 m (Atkinson et al., 1992 and 2012; Nishikawa & Tsuda, 2001; Conroy et al., 2020), though possibly reaching 750 m (Baker, 1959). Most taxa below 200 m are likely either omnivores or detritivores that are active in the mesopelagic zone or inactive diapausing taxa.

The African Sector cruise also occurred in the Subpolar Region, Southern Zone, and Antarctic Zone, as well as in the Polar Frontal Zone and Subtropical Zone. Fluffy aggregates were also the most numerous particle type in the African Sector, with the highest observed abundance of 26,002 fluffy aggregates m^{-3} (Figure 3.6a). However, the distribution of fluffy aggregates in the African Sector (Figure 3.6a) did not mirror the distribution of total particle abundance (Figure 3.4d) as was observed in the Pacific Sector (Figure 3.5a, Figure 3.4c). This is due to the contribution of fluffy aggregates to particle assemblages in subtropics and higher abundance of small particles that were too small to be imaged (Figure B.2). Fluffy aggregates were in low abundance at the surface from the Subpolar Region through the Polar Frontal Region in the African Sector, perhaps reflecting a post-bloom state of the ecosystem. The Subpolar Region had a high abundance of fluffy aggregates in the mesopelagic zone that decreased slightly at depths exceeding 2000 m. This also indicates that fluffy aggregates may be exported in the Subpolar Region, a trend we also observed in the Subpolar Region in the Pacific Sector (Figure 3.5a), as there was high particle attenuation for total particles in this region (Figure 3.4d).

Fluffy aggregates were observed to have relatively low abundances at all depths in the Southern and Antarctic Zones in the African Sector (Figure 3.6a). In contrast, a total particle maximum was observed in the mesopelagic from about 500 m – 2000 m (Figure 3.4d). This particle maximum was not represented in any detrital particle categories, indicating that these particles were too small to be imaged (Figure B.2). The Polar Frontal Zone had a notable increase in the abundance of fluffy aggregates in the mesopelagic (Figure 3.6a) at two separate stations. These fluffy aggregates in the Polar Frontal Zone were observed from 200 m down to the seafloor with relatively low attenuation with depth and at the highest abundances of any observed particle type across both cruises. This abundance increases in fluffy aggregate within the mesopelagic may represent a previous export event, possibly triggered by sporadic iron inputs (Halfter et al., 2020). We also observed a strong shoaling of the deep isopycnals across the Polar Frontal Zone associated with enhanced fluffy aggregate abundances, suggesting that low-density particles may be exported more efficiently through subduction along the isopycnal. The Subtropical Zone had a moderately high abundance of fluffy aggregates at the surface with a strong attenuation to the lowest abundance of fluffy aggregates across the transect through the mesopelagic and bathypelagic zones.

Similar to the Pacific Sector, dense aggregates and feces in the African Sector had nearly identical overall abundances and patterns, with the highest observed abundance of 1,572 dense aggregates m^{-3} and 1,533 feces m^{-3} (Figure 3.6b and 3.6d), suggesting that these particle types have similar sources or drivers. The patterns in abundance for dense aggregates and feces were similar to that of fluffy aggregates, except for in the bathypelagic of the Southern and Antarctic Zones, where dense aggregates and feces were higher in relative abundance. We observed low attenuation of dense aggregates and feces in the Subpolar Region with stations with relatively high abundance down to the seafloor. Dense aggregates and feces were also in relatively high abundance from the surface down to the seafloor in the Subpolar Region. In contrast, the Southern and Antarctic Zones showed low abundances of dense aggregates and feces except for station 28, which had a relatively high abundance of both particle types from the mesopelagic down to the bathypelagic. In the Polar Frontal Zone, we also observed a relatively high abundance of both dense aggregates and feces at all depths. Similar to the fluffy aggregate distributions, the Subtropical Zone had a moderately high abundance of dense aggregates and feces at the surface with a strong attenuation to the lowest abundances of dense aggregates and

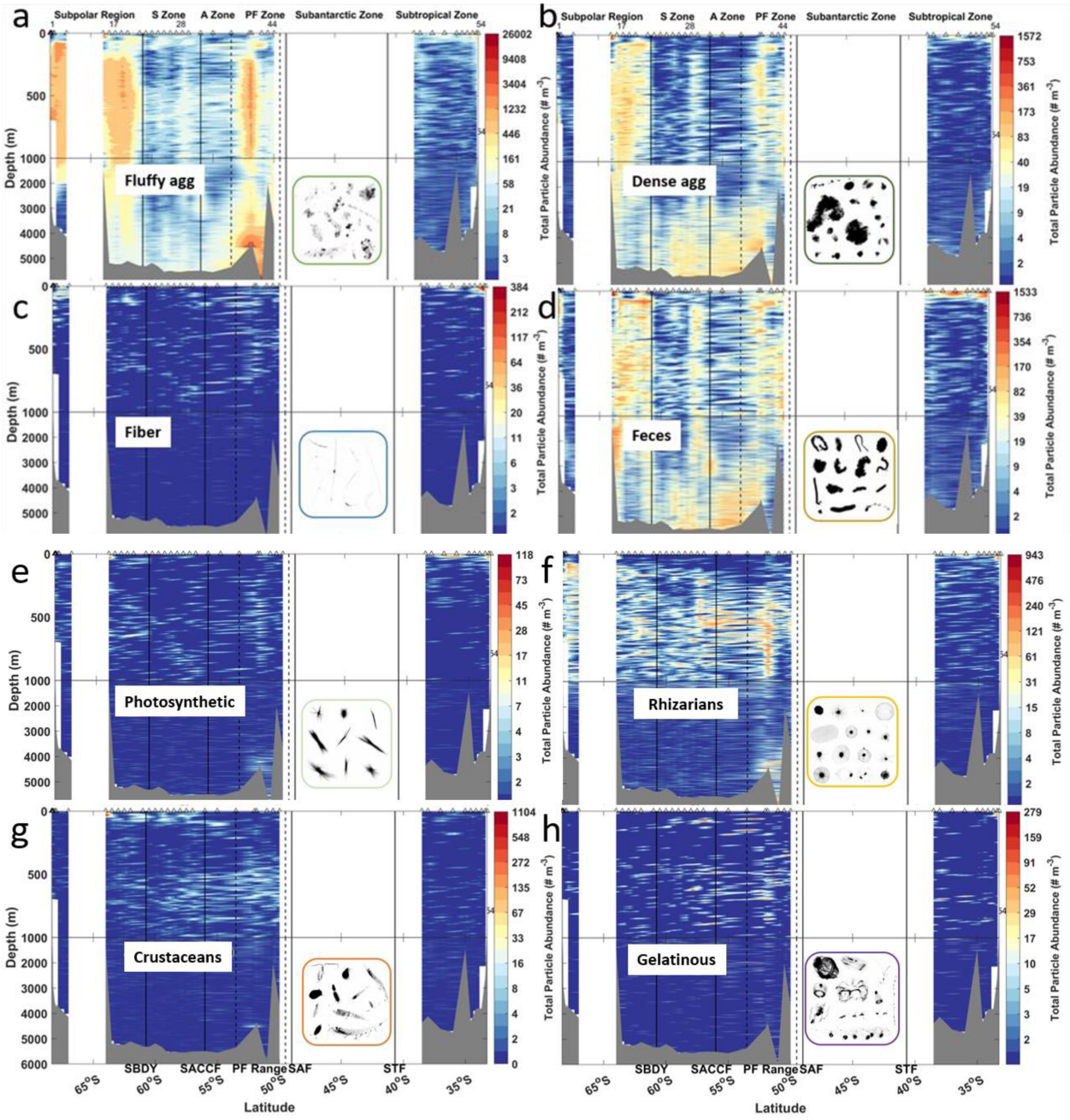

Figure 3.6: Spatial distribution of particles by particle type in the African sector of the Southern Ocean (I06S). Section plots of the concentration of detrital particles over depth: (a) fluffy aggregates, (b) dense aggregates, (c) fibers, and (d) feces. Section plots of the concentration of living (e) photosynthetic particles, (f) rhizarians, (g) crustaceans, and (h) gelatinous zooplankton are shown over depth. Solid and dashed black vertical lines indicate the approximate locations of fronts displayed and defined in Figures 3.1 and 3.3 labeled on the bottom. Frontal zones are labeled on top. Locations of samples are marked on the top with black triangles.

feces across the transect through the mesopelagic and bathypelagic zones. These patterns suggest that dense aggregates and feces attenuation vary strongly by region, with the Polar Frontal Zone and Subpolar region efficiently exporting these particle types. This is surprising as the Polar Frontal Zone usually has low abundances of fecal pellet-producing grazers (Halfter et al., 2020). However, HNLC water in the Polar Frontal Zone may facilitate higher mineral ballasting in the dense aggregates and feces due to increased silica requirements in iron-limited conditions (Meyerink et al., 2017). Again, the similarities between dense aggregates and feces patterns provide more evidence that these two categories cannot be distinguished using UVP images.

Fibers were primarily located in the surface of the Subtropical Zone in the African Sector, with the highest observed abundance of 384 fibers m^{-3} (Figure 3.6c). Similar to patterns in the Pacific Sector, there were homogenously-distributed small patches of fibers located throughout the mesopelagic and bathypelagic zones in all frontal regions, with higher abundances at the surface in the coastal Subtropical Zone and Subpolar Region. The high abundance of fibers in the surface water of these regions provides additional evidence that fibers in these data sets are primarily composed of living diatom chains, as was previously observed in coastal California (Ohman & Browman, 2019). Unfortunately, no microscopy samples were collected concurrently to verify whether the UVP observations of fibers were associated with chain-forming diatom blooms or other morphologically similar particles.

In the African Sector, living plankton were also generally found in lower abundances than detrital particles and appeared less strongly constrained by the frontal zones than living plankton observed in the Pacific Sector (Figure 3.6e-h). Photosynthetic plankton were most abundant at the surface, as expected, especially in the Subtropical Zone (Figure 3.6e). They were the lowest abundant particle type but were found in higher abundances in the African Sector than in the Pacific Sector, reaching abundances up to 118 m^{-3} (Figure 3.6e). *Trichodesmium* have been shown to be present in the Subtropical Zone of the African Sector of the Southern Ocean previously (Westberry & Siegel, 2006). Zooplankton in all three categories were relatively low in abundance at all depths in the Subtropical Zone (Figure 3.6f-h). Rhizarians were predominantly observed in the mesopelagic (Figure 3.6f) south of the Subtropical Zone. Crustaceans had a high abundance in the surface of the subpolar region that corresponded to a patch of photosynthetic plankton but were generally higher in abundance in the mesopelagic than at the surface across the transect (Figure 3.6g). The high abundance of crustaceans in the

mesopelagic of the African Sector (Figure 3.6f) may represent individuals in diapause or migrating to depth during the day (Atkinson et al., 2012; Conroy et al., 2020). Lastly, gelatinous zooplankton were observed to have the highest abundance in the mesopelagic zone across all frontal zones and had a very patchy distribution (Figure 3.6h). The distributions of living plankton suggest that the mesopelagic is a key habitat for zooplankton in the African Sector of the Southern Ocean at times of low NPP or 2-3 months after a bloom in chlorophyll *a*. It is unlikely that all of the organisms in the mesopelagic are diapausing or migrating to depth during the day because we did not observe the high abundance of organisms in the mesopelagic in the Pacific Sector at the same time of year or later in the year (Figure 3.5f-h).

3.4.4 The Role of Water Mass and Frontal Zone on Marine Particle Community

We focused on the Southern and Antarctic Zones for further analysis because these zones were sampled in both cruises and had very different particle assemblages between the cruises, particularly in the Southern Zone. Comparing the average fluorescence for each profile taken within the Southern Zone and Antarctic Zone in the Pacific Sector and Antarctic Sector (Figure 3.7a-d), the Southern Zone of the Pacific Sector showed the highest average fluorescence, about 0.3 relative fluorescence units (RFU), within the euphotic zone (Figure 3.7a). This matches the monthly satellite-derived chlorophyll *a* results that showed this region had the highest abundance of chlorophyll *a* of all of the frontal zones in both sectors (Figures 3.3b and 3.3d). These results provide further evidence that this zone was in a phytoplankton bloom state at the time of sampling. The average fluorescence profiles observed in the Antarctic Zone of the Pacific Sector (Figure 3.7b) and the Southern and Antarctic Zones of the African Sector (Figure 3.7c and 3.7d) were similar, with a euphotic zone value of around 0.15 RFU or about half of the average observed in the bloom state observed in the Southern Zone of the Pacific Sector. These data are expressed in relative units, hence the two sectors may have different calibrations and should not be compared directly. Nonetheless, the *in-situ* RFU data supports the observed surface chlorophyll *a* satellite data with highest surface chlorophyll *a* in the Southern Zone of the Pacific Sector (Figure 3.3b and 3.3d). We feel confident that the chlorophyll *a* fluorescence in the Southern Zone of the Pacific Sector was substantially higher than the other three zones, suggesting we had sampled an active phytoplankton bloom in that region.

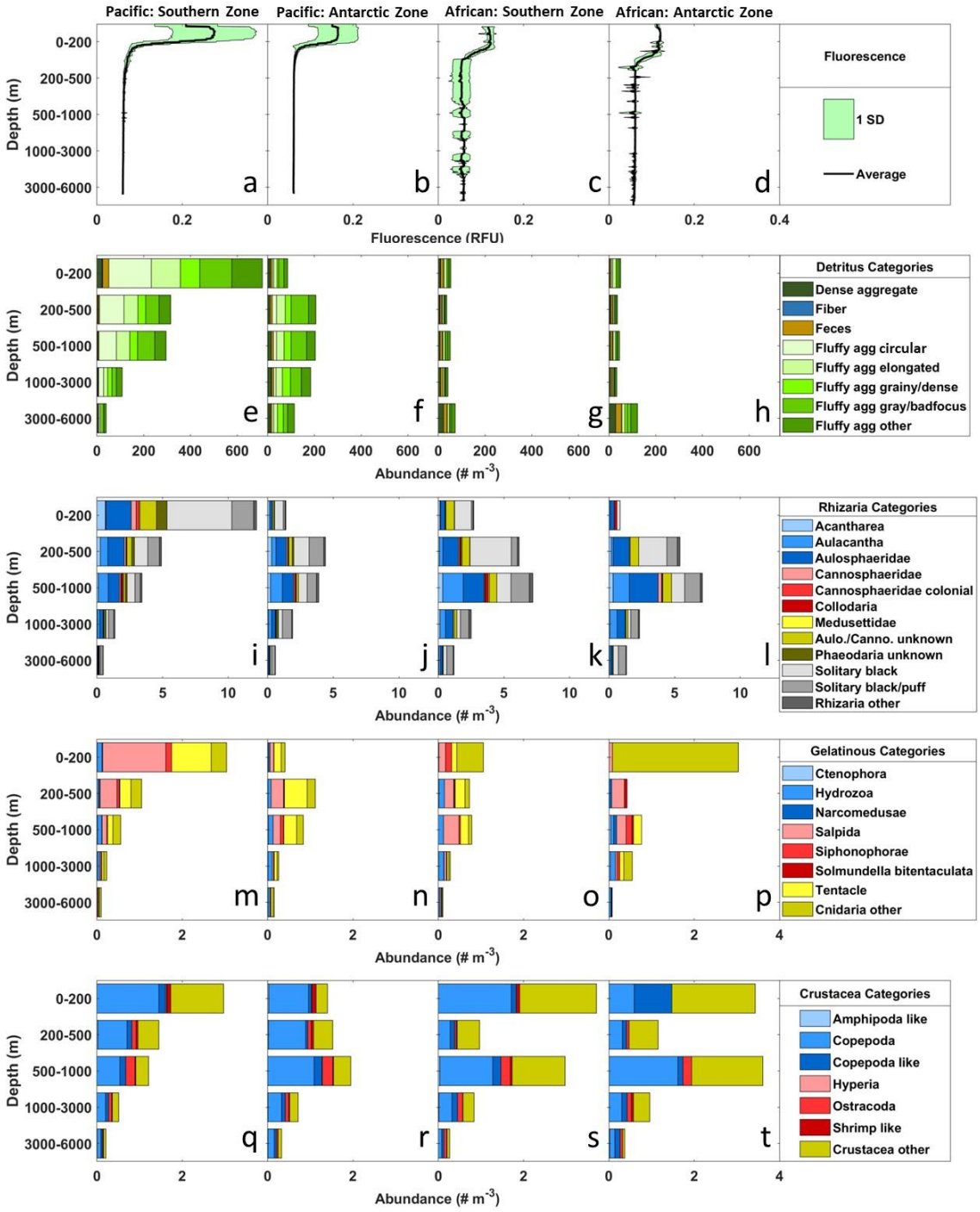

Figure 3.7: Abundance of fluorescence and different types of particles and living organisms over depth in two distinct frontal zone regions. The panels depict (a-d) the average fluorescence in Relative Fluorescence Units (RFU) (black) with one standard deviation (green), (e-h) the abundance of various detritus categories in # m^{-3}, (i-l) the average abundance of various rhizarian categories in # m^{-3}, (m-p) the abundance of various gelatinous categories in # m^{-3}, and (q-t) the abundance of various crustacean categories in # m^{-3}. From left to right in each panel: Pacific Sector (SO4P): Southern Zone, Pacific Sector (SO4P): Antarctic Zone, African Sector (IO6S): Southern Zone, African Sector (IO6S): Antarctic Zone.

We compared the abundance of different detrital particle types over depth within the Southern and Antarctic zones in the Pacific and African sectors (Figure 3.7e-h). Fluffy aggregates of various character were the most dominant particle type at all depths, zones, and sectors analyzed (Figure 3.7e-h). In contrast, the other super-categories of detritus, dense aggregates, fibers, and feces, are depicted without subdivision due to lower abundances (Figure 3.7e-h). Overall, detritus reached its highest abundance during 'bloom' conditions in the epipelagic (0 – 200 m) in the Southern Zone of the Pacific Sector (about 700 m^{-3}) (Figure 3.7e). This suggests that detritus was actively forming from phytoplankton aggregation and repackaging by zooplankton grazers. The majority of the fluffy aggregates super-category in this depth were "fluffy aggregate circular," which were relatively large, round, and light in color but not homogenously gray. We hypothesize that these "fluffy aggregate circular" are formed by the aggregation of newly dying or dead phytoplankton. Dense aggregates (about 25 m^{-3}) and feces (also about 25 m^{-3}) in the surface of the Southern Zone in the Pacific Sector were among the highest abundances analyzed within both transects. The abundance of detritus in the upper mesopelagic (200 – 500 m) and mesopelagic (500 – 1000 m) bins was about 350 m^{-3}, which was still higher than observed in any other zone/depth pair analyzed. The 1000 – 3000 m depth bin had detrital particle abundances of around 150 m^{-3}, and the deepest depth bin of 3000 – 6000 m had detrital abundances of less than 50 m^{-3}. Detrital particles were strongly attenuated in the Southern Zone of the Pacific Sector. As this zone is the 'bloom' condition, these results are not unexpected as the particles being created through photosynthesis and fecal pellet production at the surface have not had time to sink to deeper depths. In the non-bloom conditions, detritus was in highest abundance in the mesopelagic (200 – 1000 m) in the Antarctic Zone of the Pacific Sector (Figure 3.7f) and in the bathypelagic (3000 – 6000 m) in the Southern and Antarctic Zones of the African Sector (Figures 3.7g and 3.7h), suggesting these detrital particles could have been formed and exported from a previous bloom. "Fluffy aggregate gray/bad focus" particles were the most common detrital particle in the Antarctic Zone of the Pacific Sector (Figure 3.7f). The Southern and Antarctic zones of the African Sector had the highest abundances of dense aggregates and feces other than the surface of the "Bloom State" (Figures 3.7g and 3.7h). "Fluffy aggregate gray/bad focus" particles may be a more degraded version of the "fluffy aggregate circular," which were more common at the surface during the bloom. This

depth also had the highest relative abundance of dense aggregates and feces for any depth/zone analyzed.

Mirroring the detritus, the living plankton images captured by the UVP were generally most abundant in the epipelagic for the ‘bloom’ conditions (Figure 3.7i-t) and most abundant in the mesopelagic in the ‘non-bloom’ conditions. The protist predators, rhizarians, were particularly tightly correlated with patterns of detritus. Rhizarians had the highest abundance within the ‘Bloom’ waters, in the epipelagic (0 – 200 m), corresponding to greater phytoplankton and aggregate availability and decreased log-linearly over depth (Figure 3.7i). In the ‘Non-Bloom’ waters (Figure 3.7j-l), rhizarians had the highest abundance within the mesopelagic (200 – 1000 m), corresponding to the peak in aggregate abundances. As protists, rhizarians have much shorter generation times than metazoans (Flynn et al., 2018). Therefore, they can respond more quickly to bloom conditions by matching the growth rate of their prey. We investigated a breakdown of the taxa that comprised the rhizarian super-category within the Southern and Antarctic zones in the Pacific and Antarctic sectors (Figure 3.7i-l). The most numerous taxa was Solitary Black that was in high abundance within the surface waters of the Southern Zone in the Pacific Sector and the upper mesopelagic (200 – 500 m) depth bin in the “non-bloom” waters analyzed. The next most abundant rhizarian taxa was Aulosphaeridae that occured at high abundance from 0 – 1000 m in the Southern Zone of the Pacific Sector (Figure 3.7i) ‘bloom’ conditions, with highest abundance being in the epipelagic (0 – 200 m). It was also highly abundant from 200 – 1000 m in the ‘non-bloom’ conditions. Aulacantha was in highest abundance from 500 – 1000 m in the non-bloom zones and was not found from 0 - 200 m in any zone analyzed. These differences in the depth distribution of rhizarians suggest niche partitioning between these distinct morphologies, which corroborates previous observations of these groups (Biard & Ohman, 2020). However, these previous observations only analyzed the upper 500 m, making this is the first study that analyzes this high level of taxonomic identification of rhizarians down to 6000 m.

Gelatinous zooplankton had a similar pattern in abundance as rhizarians, but the taxa composition was very different between the zones and more variable in total abundance. Gelatinous zooplankton were at highest abundance from 0 – 200 m within the ‘bloom’ waters (Figure 3.7m) and within the Antarctic Zone of the African Sector (Figure 3.7p). Salpida were the most common taxa within ' bloom' conditions, followed by tentacles, cnidaria other, and a small amount of hydrozoa and siphonophorae (Figure 3.7m). In the ‘bloom’ condition, the

overall abundance of gelatinous zooplankton decreased log-linearly with depth, and the relative abundance of the various taxa was similar at all depths, suggesting little niche differentiation (Figure 3.7m). In the epipelagic of the Antarctic Zone of the African Sector, the majority of the gelatinous zooplankton were classified as cnidarians, with a few classified as salps, followed by ctenophores. However, in the mesopelagic (500 – 1000 m), there was a relatively even distribution of hydrozoans, narcomedusa, salps, siphonophores, *Solmundella bitentaculata*, and tentacles (Figure 3.7p). The Southern Zone of the African Sector had a similar distribution of gelatinous zooplankton groups but a much lower abundance from 0 – 200 m than the Antarctic Zone of the African Sector (Figure 3.7o and 3.7p). The Antarctic Zone of the Pacific Sector had a gelatinous zooplankton abundance peak from 200 – 500 m and had a similar abundance pattern to the rhizarians in this zone (Figure 3.7n). Gelatinous zooplankton can occupy multiple trophic positions, feeding on an extremely wide range of size classes, including the smallest particle size classes (> 2.5 μm) up to large crustaceans and larval fish (55 mm) (Kremer & Madin, 1992). Salps, for example, graze on phytoplankton blooms and produce dense fecal pellets that are thought to export carbon to depth efficiently (Décima et al., 2023; Steinberg et al., 2023). We did not observe many images of salp fecal pellets, likely due to their fast-sinking speeds of 300 – 1500 m d^{-1} (Bruland & Silver, 1981; Morten H. Iversen et al., 2017), and correspondingly short residence times within the water column. Therefore, salp fecal pellet abundances are likely to be underestimated by UVPs. Many gelatinous zooplankton, such as salps, can also reproduce asexually an ability that speeds up their response to prey availability and ability to exploit bloom conditions (Henschke et al., 2016; Reitzel et al., 2011).

In the ‘bloom’ state, crustaceans had a similar pattern to total detritus, rhizarians, and gelatinous zooplankton: highest in the surface and decreasing more or less log-linearly with depth (Figure 3.7q-t). Yet even during ‘non-bloom’ conditions, crustaceans were still relatively more abundant in the epipelagic and upper mesopelagic regions (200-1000m) than other living plankton categories (Figure 3.7q). Crustaceans have longer life cycles with more complex behavior, sometimes including diel vertical migration and seasonal diapause, than rhizarians or gelatinous zooplankton, which perhaps impacts their ability to adjust their location to match sinking detrital material (Atkinson et al., 1997). Copepods were always the most abundant taxa at all depths within the ‘bloom’ waters. Ostracods had their highest abundance in the lower mesopelagic (500 – 1000 m) (Figure 3.7q). These differences in depth distributions are expected

based on previously reported species distributions (Brandão et al., 2014; Conroy et al., 2020; Mierkiewicz et al., 2022).

To visualize the patterns of particle distributions by depth between these distinct regions, we performed a principle components analysis (PCA) (Figure B.4). The PCA of the particle assemblages across each transect revealed clustering driven by frontal zone and water mass (Figure B.4). In both the Pacific and African sectors, marine particle communities primarily diverged into crustacean-, feces-, and dense aggregates-dominated communities, or gelatinous zooplankton and rhizarian-dominated communities (Figure B.4b and B.4d). The depth was the primary variable driving differences in assemblages for the Pacific Sector with all particle types declining with increasing depth (Figure B.4a and B4b). The Southern Zone and Subpolar Regions had the highest abundances of all particle types. The Antarctic Zone samples were relatively separated from the Southern Zone samples. In contrast, latitude was the main driver for particle assemblage differences in the African Sector, with gelatinous zooplankton, rhizarians, and photosynthetic particles increasing with lower latitudes and all detritus categories and crustaceans increasing with higher latitudes (Figure B.4c and B.4d). These results suggest distinct particle assemblages by region and potentially different drivers in each region. However, there was great overlap of samples between the frontal zones in the African Sector.

To further investigate the possible drivers of particle composition within these key frontal zones in the African Sector, we used PCA to visualize each zone or region separately (Figure B.5). The Southern and Antarctic zones had the same water masses but very different patterns in marine particle communities. Therefore, we focused on the Southern and Antarctic zones (Figure 3.8) to understand how surface ‘bloom’ conditions influence particle assemblages. In the Southern Zone of the Pacific Sector, which had an active phytoplankton bloom at the time of sampling, the first dimension accounted for 74% of the variability and was closely aligned with changes in depth (Figure 3.8a). The second dimension accounted for 11.5% of the variability and was closely aligned with changes in the longitude. Lower Circumpolar Deep Water and Antarctic Bottom Water particle communities were very similar, contrasting with wide variability in Antarctic Surface Water particle communities. All particle categories were enriched in shallower depths, particularly photosynthetic particles, fibers, crustaceans, and rhizarians. Dense aggregates and feces were closely correlated and increased over depth. Fluffy aggregates and gelatinous zooplankton were closely correlated with each other and more abundant in eastern

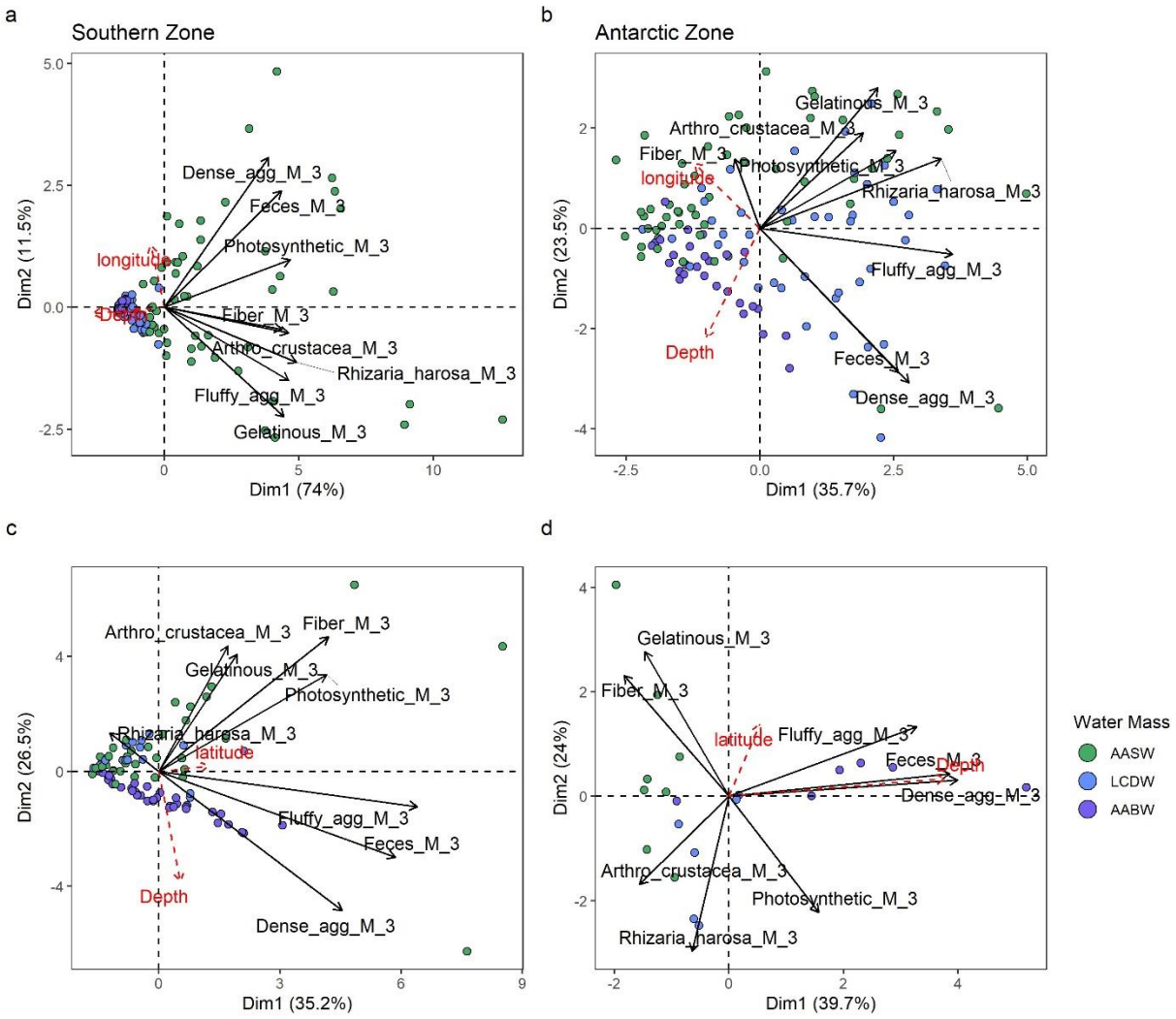

Figure 3.8: Effect of fronts and water mass on marine particle communities. Principle components analysis (PCA) on the marine particle communities in the Pacific sector of the Southern Ocean in the (a) Southern Zone and (b) Antarctic Zone and the African sector of the Southern Ocean in the (c) Southern Zone and (d) Antarctic Zone. Each super-category of marine particles is shown in solid black lines. Individual marine particle communities are shown as small circles colored by water mass. Quantitative supplementary variables are shown in a red dashed line. AASW- Antarctic Surface Water; LCDW – Lower Circumpolar Deep Water; AABW – Antarctic Bottom Water.

stations. These data corroborate our previous analysis that in the 'bloom' condition, the epipelagic is where we find the most abundant particles and most diverse particle assemblages, which are rapidly attenuated over depth. In the Antarctic Zone of the Pacific Sector, the first dimension accounted for 35.7% of the variability, and the second dimension accounted for

23.5% of the variability, which was most closely aligned with changes in depth (Figure 3.8b). Particle types were not tightly correlated, i.e., there were diverse particle communities that appeared to be shaped by other factors, such as particle sinking and animal behavior. The Antarctic Surface Water communities were associated with fibers, crustaceans, gelatinous zooplankton, and photosynthetic particles and these communities were more abundant in western stations. The Lower Circumpolar Deep Water samples were associated with particle assemblages with higher proportions of rhizarians and fluffy aggregates. Feces and dense aggregates were highly correlated with each other and most closely associated with the Antarctic Bottom Water, suggesting that they were exported efficiently, likely due to higher sinking speeds as expected for these relatively dense particles (Alldredge & Gotschalk, 1988; Turner, 2015).

The African Sector transect (Figures 3.8c and 3.8d) covered the same zones under 'non-bloom' conditions. In the Southern Zone of the African Sector, the first dimension accounted for 35.2% of the variability and was closely aligned with changes in latitude (Figure 3.8c). The second dimension accounted for 26.5% of the variability and was closely aligned with changes in depth. The Lower Circumpolar Deep Water and Antarctic Bottom Water particle communities were similar, and there was wide variability in Antarctic Surface Water particle communities. Particle communities in the Antarctic Surface Water and Lower Circumpolar Deep Water were very similar to each other. The Antarctic Surface Water and Lower Circumpolar Deep Water communities were associated with all the living or likely living particle types: rhizarians, crustaceans, gelatinous zooplankton, fibers, and photosynthetic particles. The Antarctic Bottom Water communities were associated with all the detrital particle types: Fluffy Aggregates, Feces, and Dense Aggregates. Feces were the most closely related particle type to dense aggregates, and both were most closely related to increasing depth; these patterns are similar to the 'non-bloom' conditions of the Antarctic Zone in the Pacific sector transect and suggest efficient export of dense particles from a previous export event. Photosynthetic particles and fluffy aggregates were the particle types most associated with lower latitudes. In the Antarctic Zone of the African Sector, the first dimension accounted for 39.7% of the variability and was closely aligned with changes in depth (Figure 3.8d). The second dimension accounted for 24% of the variability and was closely aligned with changes in latitude. There were diverse particle communities not strongly influenced by depth. The Antarctic Surface Water communities had higher abundances of fibers and gelatinous zooplankton. The Lower Circumpolar Deep Water particle communities

were associated with crustaceans, rhizarians, and photosynthetic particles. Antarctic Bottom Water particle assemblages were enriched in detrital particle types: fluffy aggregates, feces, and dense aggregates, as observed in the Antarctic Zone in the Pacific Sector. Overall, feces and dense aggregates are highly correlated and increased with depth at all 'non-bloom' frontal zones and sectors of the Southern Ocean analyzed (Figure 3.8). 'Bloom' condition strongly influenced particle assemblage and similarity throughout the water column on both living and detrital particles.

3.4.5 Conceptual Model

To summarize our observations, we created a conceptual diagram illustrating how the temporal evolution of *a* bloom over several months influences particle and plankton assemblages in the Southern Ocean (Figure 3.9). The 'During Bloom' conceptual diagram (Figure 3.9a) depicts a high abundance of phytoplankton and phytoplankton-derived fluffy aggregates as well as grazers such as crustaceans, rhizarians, and gelatinous zooplankton in the surface ocean (upper 200 m) as observed in the Southern Zone of the Pacific Sector (Figure 3.5a, f, g, and h). Fecal pellets produced by these grazers are largely restricted to the epipelagic (Figure 3.9a, Figure 3.5d), while large fluffy aggregates are beginning to sink out of the surface and reach mesopelagic depths (Figure 3.9a, Figure 3.5a). The 'Post Bloom' conceptual diagram (Figure 9b) represents the particle distributions 2 – 3 months after satellite-derived surface chlorophyll a maximum. There were still relatively high abundances of crustaceans and gelatinous zooplankton in the surface ocean (0 – 200 m) (Figures 3.6g and h) but low abundances of all detrital particles (Figures 3.6a-d). In the mesopelagic, there was a high abundance of grazers, such as crustaceans, rhizarians, and gelatinous zooplankton (Figures 3.6f-h) plus a high abundance of small particles (Figure 3.4d, Figure B.2), likely derived from sloppy feeding of detritus that sank out of the bloom surface water or disaggregation of locally produced fecal pellets. In the bathypelagic zone (>4000 m), there was a high abundance of large fecal pellets and dense aggregates (Figure 3.6b and 3.6d), likely supplied by sinking from the mesopelagic zone post-bloom or possibly sinking slowly from the surface during the bloom.

One of the limitations of our study is that we observed two snapshots in time of different blooms in the Southern Zone and drew inferences to understand bloom dynamics, whereas ideally, we would follow a single bloom over the course of three months to understand the fate of

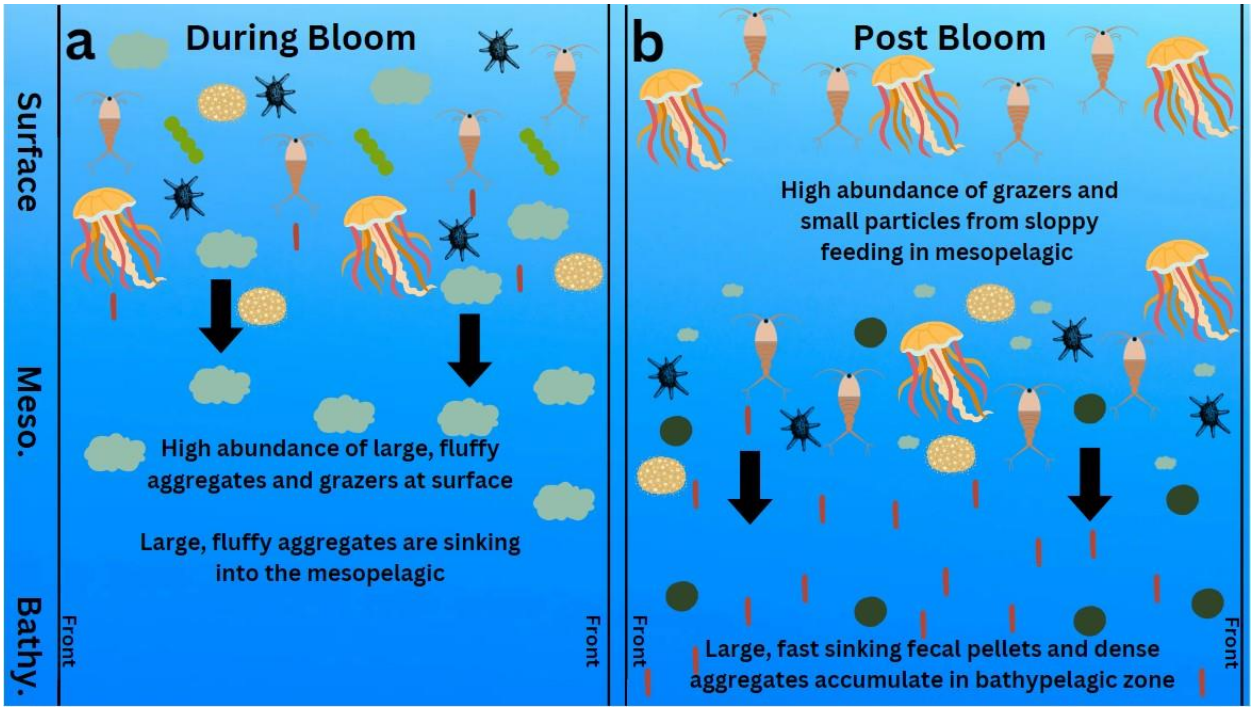

Figure 3.9: Conceptual diagram. (a) During Bloom depicts a high abundance of phytoplankton and large, phytoplankton-derived fluffy aggregates in the surface ocean (upper 200 m), grazers, and fecal pellets contained within the frontal zone (black lines). (b) Post bloom depicts some crustacean and gelatinous zooplankton in the surface (0 – 200 m) and a high abundance of small particles and grazers in the mesopelagic (200 – 1000 m). The bathypelagic zone (>4000 m) shows a high abundance of large fecal pellets and dense aggregates retained within the frontal zone.

particles. It is possible that the two bloom events highlighted in this study in the Southern Zone differed in initial phytoplankton composition and that this could have influenced the patterns of particle flux and repackaging. The Southern Ocean is known to have contrasting phytoplankton blooms, some dominated by diatoms and some dominated by *Phaeocystis* (Nissen & Vogt, 2021). It is commonly observed that diatom blooms are more likely to be associated with elevated export to the deep sea in the Southern Ocean (Roca-Martí et al., 2017; Smetacek et al., 2012), likely due to mineral ballasting from their silica frustules (Armstrong et al., 2002). *Phaeocystis* are the most productive phytoplankton generally from December through February in the Southern Ocean, particularly south of 60°S (Nissen & Vogt, 2021) yet are often associated with almost no enhanced carbon export below 300 m due to extensive remineralization (Jones & Smith, 2017; Meyer et al., 2022; Reigstad & Wassmann, 2007; Smith et al., 2017) and low rates of grazing and repackaging (Ditullio et al., 2000). We observed elevated grazer and fecal pellet abundance in the surface of the Southern Zone in the Pacific Sector and elevated fluffy aggregate

abundance to 1000 m (Figure 3.9a), which are more characteristic of a diatom bloom. Likewise, the high abundances of grazers in the mesopelagic and fecal pellets in the bathypelagic suggest that material from the surface bloom several months prior was exported to below 1000 m (Figure 9b), which is more characteristic of what is expected for a diatom-dominated bloom. Future studies could improve this limitation by following a single bloom event over time, potentially by utilizing Biogeochemical-Argo floats that can be deployed for long time scales and perform multiple dives to 2000 m (Bittig et al., 2019), although we have highlighted the need for full depth measurements of particles and plankton to understand carbon export. Future studies could also collect more information on the various phytoplankton communities that make up bloom events to determine if different export events can be linked to similar phytoplankton communities.

According to our conceptual model (Figure 3.9), particles and plankton are retained within the frontal zone and carbon export takes place in a two-stage vertical process over several months. Grazing in the mesopelagic occurred months after a surface phytoplankton bloom and appeared to be responsible for repackaging fluffy aggregates into dense aggregates and feces, facilitating deep export all the way to the seafloor. Enhanced fecal pellet production from grazing has been identified as a primary driver of export in the Southern Ocean (Cavan et al., 2015; Manno et al., 2015; Rembauville et al., 2015). However, none of these studies measured export 2-3 months after a surface bloom. If we had only observed the Pacific Sector Southern Zone during the surface chlorophyll *a* bloom, fluffy aggregates would have appeared to be the primary driver of export flux, which were attenuated nearly completely by about 2000 m (Figure 3.5a), leading us to conclude that the exported particles would have a shorter residence time in the Southern Ocean (~ 200 – 500 years) (Siegel et al., 2021). Only by sampling a similar region months after a surface phytoplankton bloom did we observe signs of high grazing pressure in the mesopelagic zone and high abundances of feces and dense aggregates in the bathypelagic zone, which leads us to conclude that a second-stage repackaging of detritus in the mesopelagic potentially stores carbon for much longer periods of time in the Southern Ocean (~750 – 1000 years) (Siegel et al., 2021). These results emphasize the importance of longer-term observations (months instead of weeks) following a bloom event and observations of deep particles (2000 m to the seafloor) to fully constrain the export pathways and durability of carbon storage in the deep sea. These results are important to consider for the verification step of carbon durability for

potential marine Carbon Dioxide Removal (mCDR) projects in the Southern Ocean (Boyd et al., 2023).

3.5 Conclusion

We captured detailed data on marine particle assemblages from both 'bloom' and 'post-bloom' conditions in the same regions of the Southern Ocean. This study highlights how marine particles and plankton distributions change over time in the wake of a phytoplankton bloom in the Southern Ocean and how fronts contain biological activity and carbon export from the surface down to the seafloor. It also illuminates the important role of grazers, particularly a few months after phytoplankton blooms subside, in transforming aggregates by breaking them apart into numerous smaller particles and repackaging them into feces in the mesopelagic zone. Feces appear to sink rapidly and readily, accumulating in large quantities in the bathypelagic zone a few months after a phytoplankton bloom at the surface. These bottom-up effects from fronts and top-down effects from grazing play a substantial role in how much carbon is exported after phytoplankton blooms in the Southern Ocean. The UVP offers a unique opportunity to observe these phenomena. We show that particle morphology, deep observations, and large spatial scales are essential for understanding the linkages and fate of carbon in the marine system.

3.6 References

Alldredge, A. (1998). The carbon, nitrogen and mass content of marine snow as a function of aggregate size. Deep Sea Research I, 45, 529–541.

Alldredge, A. L., & Gotschalk, C. C. (1989). Direct observations of the mass flocculation of diatom blooms: characteristics, settling velocities and formation of diatom aggregates. Deep Sea Research Part A, Oceanographic Research Papers, 36(2), 159–171. https://doi.org/10.1016/0198-0149(89)90131-3

Alldredge, Alice L., & Gotschalk, C. (1988). In situ settling behavior of marine snow. Limnology and Oceanography, 33(3), 339–351. https://doi.org/10.4319/lo.1988.33.3.0339

Armstrong, R., Lee, C., Hedges, J., Honjo, S., & Wakeham, S. G. (2002). A new, mechanistic model for organic carbon fluxes in the ocean based on the quantitative association of POC with ballast minerals. Deep Sea Research II: Topical Studies in Oceanography, 49, 219–236. Retrieved from http://www.sciencedirect.com/science/article/pii/S0967064501001011

Atkinson, A, Williams, R., & Poulet, S. A. (1992). Diel vertical migration and feeding of copepods at an oceanic site near South Georgia. Marine Biology, 113, 583-593. https://doi.org/10.1007/BF00349702

Atkinson, A., Schnack-Schiel, S. B., Ward, P., & Marin, V. (1997). Regional differences in the life cycle of *Calanoides acutus* (Copepoda: Calanoida) within the Atlantic sector of the Southern Ocean. Marine Ecology Progress Series, 150, 99–111. https://doi.org/10.3354/meps150099

Atkinson, A, Ward, P., Hunt, B. P. V, Pakhomov, E. A., & Hosie, G. W. (2012). An overview of Southern Ocean zooplankton data: Abundance, biomass, feeding and functional relationships. CCAMLR Science, 19, 171–218.

Atkinson, Angus. (1998). Life cycle strategies of epipelagic copepods in the Southern Ocean. Journal of Marine Systems, 15, 289–311. https://doi.org/10.1016/S0924-7963(97)00081-X

Baker, A. (1959). Distribution and life history of *Euphausia triacantha* Holt and Tattersall. Discovery Reports, 29, 309–340.

Baumgartner, M. F., & Tarrant, A. M. (2017). The physiology and ecology of diapause in marine copepods. Annual Review of Marine Science, 9(1), 387–411. https://doi.org/10.1146/annurev-marine-010816-060505

Behrenfeld, M. J., Boss, E. S., & Halsey, K. H. (2021). Phytoplankton community structuring and succession in a competition-neutral resource landscape. ISME Communications, 1(1), 12. https://doi.org/10.1038/s43705-021-00011-5

Bianchi, D., Stock, C., Galbraith, E. D., & Sarmiento, J. L. (2013). Diel vertical migration: Ecological controls and impacts on the biological pump in a one-dimensional ocean model. Global Biogeochemical Cycles, 27(2), 478–491. https://doi.org/10.1002/gbc.20031

Biard, T., & Ohman, M. D. (2020). Vertical niche definition of test-bearing protists (Rhizaria) into the twilight zone revealed by in situ imaging. Limnology and Oceanography, 65(11), 2583–2602. https://doi.org/10.1002/lno.11472

Bittig, H. C., Maurer, T. L., Plant, J. N., Wong, A. P., Schmechtig, C., Claustre, H., Truss, T. W., Udaya Bhaskar, T. V. S., Boss, E., Dall'Olmo, G., Organelli, E., Poteau, A., Johnson, K. S., Hanstein, C., Leymarie, E., Le Reste, S., Riser, S. C., Rupan, A. R., Taillandier, V., Thierry, V., & Xing, X. (2019). A BGC-Argo guide: Planning, deployment, data handling and usage. Frontiers in Marine Science, 6(502), 1-23. https://doi.org/10.3389/fmars.2019.00502

Boyd, P. W., Claustre, H., Legendre, L., Gattuso, J.-P., & Le Traon, P.-Y (2023). Operational monitoring of open-ocean carbon dioxide removal deployments: Detection, attribution, and determination of side effects. Oceanography. 36(Supplement 1), 1-10. https://doi.org/10.5670/oceanog.2023.s1.2

Boyd, P. W., Claustre, H., Levy, M., Siegel, D. A., & Weber, T. (2019). Multi-faceted particle pumps drive carbon sequestration in the ocean. Nature, 568(7752), 327–335. https://doi.org/10.1038/s41586-019-1098-2

Boyd, P. W., Arrigo, K. R., Ardyna, M., Halfter, S., Huckstadt, L., Kuhn, A. M., Lannuzel, D., Neukermans, G., Novaglio, C., Shadwick, E. H., Swart, S., & Thomalla, S. J. (2024). The role of biota in the Southern Ocean carbon cycle. Nature Reviews Earth and Environment. 5, 390–408. https://doi.org/10.1038/s43017-024-00531-3

Brandão, S. N., Vital, H., & Brandt, A. (2014). Southern Polar Front macroecological and biogeographical insights gained from benthic Ostracoda. Deep-Sea Research Part II: Topical Studies in Oceanography, 108, 33–50. https://doi.org/10.1016/j.dsr2.2014.06.004

Bruland, K. W., & Silver, M. W. (1981). Sinking rates of fecal pellets from gelatinous zooplankton (salps, pteropods, doliolids). Marine Biology, 63, 295–300. https://doi.org/10.1007/BF00395999

Buesseler, K. O., Lamborg, C. H., Boyd, P. W., Lam, P. J., Trull, T. W., Bidigare, R. R., Bishop, J. K. B., Casciotti, K. L., Dehairs, F., Elskens, M., Honda, M., Karl, D. M., Siegel, D. A., Silver, M. W., Steinberg, D. K., Valdes, J., Van Mooy, B., & Wilson, S. (2007). Revisiting carbon flux through the ocean's twilight zone. Science, 316(5824), 567–570. https://doi.org/10.1126/science.1137959

Carter, L., McCave, I. N., & Williams, M. J. M. (2008). Circulation and water masses of the Southern Ocean: A review. Developments in Earth and Environmental Sciences, 8, 85–114. https://doi.org/10.1016/S1571-9197(08)00004-9

Cavan, E. L., Le Moigne, F. A. C., Poulton, A. J., Tarling, G. A., Ward, P., Daniels, C. J., Fragoso, G. M., & Sanders, R. J. (2015). Attenuation of particulate organic carbon flux in the Scotia Sea, Southern Ocean, is controlled by zooplankton fecal pellets. Geophysical Research Letters, 42(3), 821–830. https://doi.org/10.1002/2014GL062744

Chapman, C. C., Lea, M. A., Meyer, A., Sallée, J. B., & Hindell, M. (2020). Defining Southern Ocean fronts and their influence on biological and physical processes in a changing climate. Nature Climate Change, 10(3), 209–219. https://doi.org/10.1038/s41558-020-0705-4

Conroy, J. A., Steinberg, D. K., Thibodeau, P. S., & Schofield, O. (2020). Zooplankton diel vertical migration during Antarctic summer. Deep-Sea Research Part I: Oceanographic Research Papers, 162, 103324. https://doi.org/10.1016/j.dsr.2020.103324

Copernicus Climate Service (2023) Global ocean gridded L 4 sea surface heights and derived variables reprocessed copernicus climate service. E.U. Copernicus Marine Service Information. CLS (France). https://doi.org/10.48670/moi-00145

Décima, M., Stukel, M. R., Nodder, S. D., Gutiérrez-Rodríguez, A., Selph, K. E., dos Santos, A. L., Safi, K., Kelly, T. B., Deans, F., Morales, S. E., Baltar, F., Latasa, M., Gorbunov, M. Y., & Pinkerton, M. (2023). Salp blooms drive strong increases in passive carbon export in the Southern Ocean. Nature Communications, 14(425) 1–16. https://doi.org/10.1038/s41467-022-35204-6

Ditullio, G. R., Grebmeier, J. M., Arrigo, K. R., Lizotte, M. P., Robinsonk, D. H., Leventer, A., Barry, J. P., Vanwoert, M. L., & Dunbar, R. B. (2000). Rapid and early export of *Phaeocystis antarctica* blooms in the Ross Sea, Antarctica. Nature, 404, 595-598. https://doi.org/10.1038/35007061

Drago, L., Panaïotis, T., Irisson, J. O., Babin, M., Biard, T., Carlotti, F., Coppola, L., Guidi, L., Hauss H., Karp-Boss L., Lombard F., McDonnell A. M. P., Picheral M., Rogge A., Waite A. M., Stemmann L., Kiko R. (2022). Global distribution of zooplankton biomass estimated by in situ imaging and machine learning. Frontiers in Marine Science, 9, 894372. https://doi.org/10.3389/fmars.2022.894372

Flynn, K. J., Skibinski, D. O. F., & Lindemann, C. (2018). Effects of growth rate, cell size, motion, and elemental stoichiometry on nutrient transport kinetics. PLoS Computational Biology, 14(4), e1006118. https://doi.org/10.1371/journal.pcbi.1006118

Gaube, P., McGillicuddy, D. J., Chelton, D. B., Behrenfeld, M. J., & Strutton, P. G. (2014). Regional variations in the influence of mesoscale eddies on near-surface chlorophyll. Journal of Geophysical Research: Oceans, 119(12), 8195–8220. https://doi.org/10.1002/2014JC010111

Geoffroy, M., Langbehn, T., Priou, P., Varpe, Ø., Johnsen, G., Le Bris, A., Fisher, J. A. D., Daase, M., McKee, D., Cohen, J., & Berge, J. (2021). Pelagic organisms avoid white, blue, and red artificial light from scientific instruments. Scientific Reports, 11(1), 14941. https://doi.org/10.1038/s41598-021-94355-6

Goldthwait, S. A., Carlson, C. A., Henderson, G. K., & Alldredge, A. L. (2005). Effects of physical fragmentation on remineralization of marine snow. Marine Ecology Progress Series, 305, 59–65.

Gruber, N., Landschützer, P., Landschützer, L., & Lovenduski, N. S. (2019). The variable Southern Ocean carbon sink. Annual Review of Marine Science, 11, 159–186. https://doi.org/10.1146/annurev-marine-121916

Guidi, L., Jackson, G. A., Stemmann, L., Miquel, J. C., Picheral, M., & Gorsky, G. (2008). Relationship between particle size distribution and flux in the mesopelagic zone. Deep-Sea Research Part I: Oceanographic Research Papers, 55(10), 1364–1374. https://doi.org/10.1016/j.dsr.2008.05.014

Halfter, S., Cavan, E. L., Swadling, K. M., Eriksen, R. S., & Boyd, P. W. (2020). The role of zooplankton in establishing carbon export regimes in the Southern Ocean – A comparison of two representative case studies in the subantarctic region. Frontiers in Marine Science, 7(September), 1–8. https://doi.org/10.3389/fmars.2020.567917

Henschke, N., Everett, J. D., Richardson, A. J., & Suthers, I. M. (2016). Rethinking the role of salps in the ocean. Trends in Ecology and Evolution, 31(9), 720–733. https://doi.org/10.1016/j.tree.2016.06.007

Irisson, J.-O., Ayata, S.-D., Lindsay, D. J., Karp-Boss, L., & Stemmann, L. (2022). Machine learning for the study of plankton and marine snow from images. Annual Review of Marine Science, 14(1), 277–301. https://doi.org/10.1146/annurev-marine-041921-013023

Iversen, M. H. (2023). Carbon export in the ocean: A biologist's perspective. Annual Review of Marine Science, 15, 17.1-17.25. https://doi.org/10.1146/annurev-marine-032122

Iversen, M. H., & Lampitt, R. S. (2020). Size does not matter after all: No evidence for a size-sinking relationship for marine snow. Progress in Oceanography, 189, 102445. https://doi.org/10.1016/j.pocean.2020.102445

Iversen, M. H., & Ploug, H. (2010). Ballast minerals and the sinking carbon flux in the ocean: Carbon-specific respiration rates and sinking velocity of marine snow aggregates. Biogeosciences, 7(9), 2613–2624. https://doi.org/10.5194/bg-7-2613-2010

Iversen, Morten H., Pakhomov, E. A., Hunt, B. P. V., van der Jagt, H., Wolf-Gladrow, D., & Klaas, C. (2017). Sinkers or floaters? Contribution from salp pellets to the export flux during a large bloom event in the Southern Ocean. Deep-Sea Research Part II: Topical Studies in Oceanography, 138, 116–125. https://doi.org/10.1016/j.dsr2.2016.12.004

Jones, R. M., & Smith, W. O. (2017). The influence of short-term events on the hydrographic and biological structure of the southwestern Ross Sea. Journal of Marine Systems, 166, 184–195. https://doi.org/10.1016/j.jmarsys.2016.09.006

Kiko, R., Picheral, M., Antoine, D., Babin, M., Berline, L., Biard, T., Boss, E., Brandt, P., Carlotti, R., Christiansen, S., Coppola, L., de la Cruz, L., Diamond-Riquier, E., Durrieu de Madron, X., Elineau, A., Gorsky, G., Guidi, L., Hauss, H., Irisson, J. O., Karp-Boss, L., Karstensen, J., Kim, D., Lekanoff, R. M., Lombard, F., Lopes, R. M., Marec, C., McDonnell, A. M. P., Niemeyer, D., Noyon, M., O'Daly, S. H., Ohman, M. D., Pretty, J. L., Rogge, A., Searson, S., Shibata, M., Tanaka, Y., Tanhua, T., Taucher, J., Trudnowska, E., Turner, J. S., Waite, A., & Stemmann, L. (2022). A global marine particle size distribution dataset obtained with the Underwater Vision Profiler 5. Earth System Science Data, 14(9), 4315–4337. https://doi.org/10.5194/essd-14-4315-2022

Kiørboe, T. (2001). Formation and fate of marine snow: Small-scale processes with large-scale implications. Scientia Marina, 65(Supplement 2), 57–71. https://doi.org/10.3989/scimar.2001.65s257

Kremer, P., & Madin, L. P. (1992). Particle retention efficiency of salps. Journal of Plankton Research, 14(7), 1009–1015. https://doi.org/10.1093/plankt/14.7.1009

De La Rocha, C. L., & Passow, U. (2007). Factors influencing the sinking of POC and the efficiency of the biological carbon pump. Deep-Sea Research Part II: Topical Studies in Oceanography, 54(5–7), 639–658. https://doi.org/10.1016/j.dsr2.2007.01.004

Laurenceau-Cornec, E. C., Le Moigne, F. A. C., Gallinari, M., Moriceau, B., Toullec, J., Iversen, M. H., Engel, A., & De La Rocha, C. L. (2020). New guidelines for the application of Stokes' models to the sinking velocity of marine aggregates. Limnology and Oceanography, 65(6), 1264–1285. https://doi.org/10.1002/lno.11388

Lerman, A., Lal, D., & Dacey, M. F. (1974). Stokes' Settling and Chemical Reactivity of Suspended Particles in Natural Waters. In R. J. Gibbs (Ed.), Suspended solids in water (pp. 17–47). Plenum Press.

Lombard, F., Boss, E., Waite, A. M., Uitz, J., Stemmann, L., Sosik, H. M., Schultz, J., Romagnan, J. B., Picheral, M., Pearlman, J., Ohman, M. D., Niehoff, B., Möller, K. O., Miloslavich, P., Lara-Lpez, A., Kudela, R., Lopes, R. M., Kiko, R., Karp-Boss, L., Jaffe, J. S., Iversen, M. H., Irisson, J. O., Fennel, K., Hauss, H., Guidi, L., Gorsky, G., Giering, S. L. C., Gaube, P., Gallager, S., Dubelaar, G., Cowen, R. K., Carlotti, F., Briseño-Avena, C., Berline, L., Benoit-Bird, K., Bax, N., Batten, S., Ayata, S. D., Artigas, L. F., & Appeltans, W. (2019). Globally consistent quantitative observations of planktonic ecosystems. Frontiers in Marine Science, 6(196), 1-21. https://doi.org/10.3389/fmars.2019.00196

Manno, C., Stowasser, G., Enderlein, P., Fielding, S., & Tarling, G. A. (2015). The contribution of zooplankton faecal pellets to deep-carbon transport in the Scotia Sea (Southern Ocean). Biogeosciences, 12(6), 1955–1965. https://doi.org/10.5194/bg-12-1955-2015

McDonnell, A. M. P., & Buesseler, K. O. (2012). A new method for the estimation of sinking particle fluxes from measurements of the particle size distribution, average sinking velocity, and carbon content. Limnology and Oceanography: Methods, 10(5), 329–346. https://doi.org/10.4319/lom.2012.10.329

Meyer, M. G., Jones, R. M., & Smith, W. O. (2022). Quantifying seasonal particulate organic carbon concentrations and export potential in the Southwestern Ross Sea using autonomous gliders. Journal of Geophysical Research: Oceans, 127(10). https://doi.org/10.1029/2022JC018798

Meyerink, S. W., Ellwood, M. J., Maher, W. A., Dean Price, G., & Strzepek, R. F. (2017). Effects of iron limitation on silicon uptake kinetics and elemental stoichiometry in two Southern Ocean diatoms, *Eucampia antarctica* and *Proboscia inermis*, and the temperate diatom *Thalassiosira pseudonana*. Limnology and Oceanography, 62(6), 2445–2462. https://doi.org/10.1002/lno.10578

Mierkiewicz, J., Trudnowska, E., Błachowiak-Samołyk, K., & Bielecka, L. (2022). Distinctive zonation of planktonic ostracods assemblages in the dynamic Southeastern Atlantic. Journal of Sea Research, 187, 102256. https://doi.org/10.1016/j.seares.2022.102256

Mishra, R. K., Naik, R. K., Venkataramana, V., Jena, B., AnilKumar, N., Soares, M. A., Sarkar, A., & Singh, A. (2020). Phytoplankton biomass and community composition in the frontal zones of Southern Ocean. Deep-Sea Research Part II: Topical Studies in Oceanography, 178(April), 104799. https://doi.org/10.1016/j.dsr2.2020.104799

Moriarty, R., Buitenhuis, E. T., & Le Quéré, C. (2013). Distribution of known macrozooplankton abundance and biomass in the global ocean. Earth System Science Data, 5(2), 241–257. https://doi.org/10.5194/essd-5-241-2013

National Aeronautics and Space Administration (NASA) Goddard Space Flight Center, Ocean Ecology Laboratory, Ocean Biology Processing Group (2014). MODIS-Aqua Ocean Color Data. NASA Goddard Space Flight Center, Ocean Ecology Laboratory, Ocean Biology Processing Group.

Nishikawa, J., & Tsuda, A. (2001). Diel vertical migration of the tunicate *Salpa thompsoni* in the Southern Ocean during summer. Polar Biology, 24(4), 299–302. https://doi.org/10.1007/s003000100227

Nissen, C., & Vogt, M. (2021). Factors controlling the competition between *Phaeocystis* and diatoms in the Southern Ocean and implications for carbon export fluxes. Biogeosciences, 18(1), 251–283. https://doi.org/10.5194/bg-18-251-2021

Ohman, M. D., & Browman, H. (2019). A sea of tentacles: Optically discernible traits resolved from planktonic organisms in situ. ICES Journal of Marine Science, 76(7), 1959–1972. https://doi.org/10.1093/icesjms/fsz184

Ohman, M. D., Powell, J. R., Picheral, M., & Jensen, D. W. (2012). Mesozooplankton and particulate matter responses to a deep-water frontal system in the southern California Current System. Journal of Plankton Research, 34(9), 815–827. https://doi.org/10.1093/plankt/fbs028

Orsi, A. H., Whitworth, T., & Nowlin, W. D. (1995). On the meridional extent and fronts of the Antarctic Circumpolar Current. Deep-Sea Research I: Oceanographic Research Papers, 42(5), 64–673. https://doi.org/10.1016/0967-0637(95)00021-W

Pardo, P. C., Pérez, F. F., Velo, A., & Gilcoto, M. (2012). Water masses distribution in the Southern Ocean: Improvement of an extended OMP (eOMP) analysis. Progress in Oceanography, 103, 92–105. https://doi.org/10.1016/j.pocean.2012.06.002

Picheral, M, Colin, S., & Irisson, J. (2017). EcoTaxa, a tool for the taxonomic classification of images. Retrieved from http://ecotaxa.obs-vlfr.fr

Picheral, M., Guidi, L., Stemmann, L., Karl, D. M., Iddaoud, G., & Gorsky, G. (2010). The underwater vision profiler 5: An advanced instrument for high spatial resolution studies of particle size spectra and zooplankton. Limnology and Oceanography: Methods, 8(SEPT), 462–473. https://doi.org/10.4319/lom.2010.8.462

Pinkerton, M. H., Smith, A. N. H., Raymond, B., Hosie, G. W., Sharp, B., Leathwick, J. R., & Bradford-Grieve, J. M. (2010). Spatial and seasonal distribution of adult *Oithona similis* in the Southern Ocean: Predictions using boosted regression trees. Deep-Sea Research Part I: Oceanographic Research Papers, 57(4), 469–485. https://doi.org/10.1016/j.dsr.2009.12.010

Ploug, H., Iversen, M. H., Koski, M., & Buitenhuis, E. T. (2008). Production, oxygen respiration rates, and sinking velocity of copepod fecal pellets: Direct measurements of ballasting by opal and calcite. Limnology and Oceanography, 53(2), 469–476. https://doi.org/10.4319/lo.2008.53.2.0469

Pollard, R. T., Lucas, M. I., & Read, J. F. (2002). Physical controls on biogeochemical zonation in the Southern Ocean. Deep-Sea Research II: Topical Studies in Oceanography, 49, 3289–3305. https://doi.org/10.1016/S0967-0645(02)00084-X

Reigstad, M., & Wassmann, P. (2007). Does *Phaeocystis* spp. contribute significantly to vertical export of organic carbon? Biogeochemistry, 83(1–3), 217–234. https://doi.org/10.1007/s10533-007-9093-3

Reitzel, A. M., Stefanik, D., & Finnerty, J. R. (2011). Asexual reproduction in Cnidaria: Comparative processes and candidate mechanisms. In T. Flatt & A. Heyland (Eds.), Mechanisms of Life History Evolution: The Genetics and Physiology of Life History Traits and Trade-Offs (online edition, pp. 101–113). Oxford: Oxford Academic. https://doi.org/10.1093/acprof:oso/9780199568765.003.0008

Rembauville, M., Blain, S., Armand, L., Quéguiner, B., & Salter, I. (2015). Export fluxes in a naturally iron-fertilized area of the Southern Ocean - Part 2: Importance of diatom resting spores and faecal pellets for export. Biogeosciences, 12(11), 3171–3195. https://doi.org/10.5194/bg-12-3171-2015

Roca-Martí, M., Puigcorbé, V., Iversen, M. H., van der Loeff, M. R., Klaas, C., Cheah, W., Bracher, A., & Masque, P. (2017). High particulate organic carbon export during the decline of a vast diatom bloom in the Atlantic sector of the Southern Ocean. Deep-Sea Research Part II: Topical Studies in Oceanography, 138, 102–115. https://doi.org/10.1016/j.dsr2.2015.12.007

Romagnan, J. B., Legendre, L., Guidi, L., Jamet, J. L., Jamet, D., Mousseau, L., Pedrotti, M. L., Picheral, M., Gorsky, G., Sardet, C., & Stemmann, L. (2015). Comprehensive model of annual plankton succession based on the whole-plankton time series approach. PLoS ONE, 10(3), e0119219. https://doi.org/10.1371/journal.pone.0119219

Romagnan, J. B., Aldamman, L., Gasparini, S., Nival, P., Aubert, A., Jamet, J. L., & Stemmann, L. (2016). High frequency mesozooplankton monitoring: Can imaging systems and automated sample analysis help us describe and interpret changes in zooplankton community composition and size structure — An example from a coastal site. Journal of Marine Systems, 162, 18–28. https://doi.org/10.1016/j.jmarsys.2016.03.013

Samanta, S., Cloete, R., Dey, S. P., Barraqueta, J. L. M., Loock, J. C., Meynecke, J. O., de Bie, J., Vichi, M., & Roychoudhury, A. N. (2023). Exchange of Pb from Indian to Atlantic Ocean is driven by Agulhas Current and atmospheric Pb input from South Africa. Scientific Reports, 13(5465) 1–12. https://doi.org/10.1038/s41598-023-32613-5

Sanders, R. J., Henson, S. A., Martin, A. P., Anderson, T. R., Bernardello, R., Enderlein, P., Fielding, S., Giering, S. L. C., Hartmann, M., Iversen, M., Khatiwala, S., Lam, P., Lampitt, R., Mayor, D. J., Moore, M. C., Morphy, E., Painter S. C., Poulton, A. J., Saw, K., Stowasser, G., Tarling, G. A., Torres-Valdes, S., Trimmer, M., Wolff, G. A., Yool, A., & Zubkov, M. (2016). Controls over ocean mesopelagic interior carbon storage (COMICS): Fieldwork, synthesis, and modeling efforts. Frontiers in Marine Science, 3(136), 1 - 7. https://doi.org/10.3389/fmars.2016.00136

Sarmiento, J. L., & Gruber, N. (2006). Carbon Cycle, CO_2 and Climate. In Ocean Biogeochemical Dynamics (pp. 392–453). https://doi.org/10.1063/1.2754608

Schröder, S. M., Kiko, R., & Koch, R. (2020). Morphocluster: Efficient annotation of plankton images by clustering. Sensors (Switzerland), 20(11), 1–26. https://doi.org/10.3390/s20113060

Siegel, D. A., Devries, T., Doney, S. C., & Bell, T. (2021). Assessing the sequestration time scales of some ocean-based carbon dioxide reduction strategies. Environmental Research Letters, 16(10), 104003. https://doi.org/10.1088/1748-9326/ac0be0

Sigman, D. M., & Boyle, E. A. (2000). Glacial/interglacial variations in atmospheric carbon dioxide. Nature, 407, 859–869. https://doi.org/10.1038/35038000

Sigman, D. M., Hain, M. P., & Haug, G. H. (2010). The polar ocean and glacial cycles in atmospheric CO2 concentration. Nature, 466(7302), 47–55. https://doi.org/10.1038/nature09149

Smetacek, V., Klaas, C., Strass, V. H., Assmy, P., Montresor, M., Cisewski, B., Savoye, N., Webb, A., d'Ovidio, F., Arrieta, J. M., Bathmann, U., Bellerby, R., Berg, G. M., Croot, P., Gonzalez, S., Henjes, J., Herndl, G. J., Hoffmann, L. J., Leach, H., Losch, M., Mills, M. M., Neill, C., Peeken, I., Rottgers, R., Sachs, O., Sauter, E., Schmidt, M. M., Schwarz, J., Terbruggen, A., & Wolf-Gladrow, D. (2012). Deep carbon export from a Southern Ocean iron-fertilized diatom bloom. Nature, 487(7407), 313–319. https://doi.org/10.1038/nature11229

Smith, W. O., McGillicuddy, D. J., Olson, E. B., Kosnyrev, V., Peacock, E. E., & Sosik, H. M. (2017). Mesoscale variability in intact and ghost colonies of *Phaeocystis antarctica* in the Ross Sea: Distribution and abundance. Journal of Marine Systems, 166, 97–107. https://doi.org/10.1016/j.jmarsys.2016.05.007

Sow, S. L. S., Brown, M. V., Clarke, L. J., Bissett, A., van de Kamp, J., Trull, T. W., Raes, E. J., Seymour, J. R., Bramucci, A. R., Ostrowski, M., Boyd, P. W., Deagle, B. E., Pardo, P. C., Sloyan, B. M., & Bodrossy, L. (2022). Biogeography of Southern Ocean prokaryotes: a comparison of the Indian and Pacific sectors. Environmental Microbiology, 24(5), 2449–2466. https://doi.org/10.1111/1462-2920.15906

Steinberg, D. K., & Landry, M. R. (2017). Zooplankton and the ocean carbon cycle. Annual Review of Marine Science, 9(1), 413–444. https://doi.org/10.1146/annurev-marine-010814-015924

Steinberg, D. K., Stamieszkin, K., Maas, A. E., Durkin, C. A., Passow, U., Estapa, M. L., Omand, M. M., McDonnell, A. M. P., Karp-Boss, L., Galbraith, M., & Siegel, D. A. (2023). The outsized role of salps in carbon export in the Subarctic Northeast Pacific Ocean. Global Biogeochemical Cycles, 37(1), e2022GB007523. https://doi.org/10.1029/2022GB007523

Stemmann, L., & Boss, E. (2012). Plankton and particle size and packaging: From determining optical properties to driving the biological pump. Annual Review of Marine Science, 4, 263–290. https://doi.org/10.1146/annurev-marine-120710-100853

Stokes, G. G. (1851). On the effect of the internal friction of fluids on the motion of pendulums. Transactions of the Cambridge Philosophical Society, Part II(9), 8–106.

Suaria, G., Achtypi, A., Perold, V., Lee, J. R., Pierucci, A., Bornman, T. G., Aliani, S., & Ryan, P. G. (2020). Microfibers in oceanic surface waters: A global characterization. Science Advances, 6(eaay8493), 8493–8498. https://doi.org/10.1126/sciadv.aay8493

Talley, L. D., Pickard, G. L., Emery, W. J., & Swift, J. H. (2011). Chapter 13: Southern Ocean. In Descriptive Physical Oceanography (Vol. 6, pp. 437–471).

Trudnowska, E., Lacour, L., Ardyna, M., Rogge, A., Irisson, J. O., Waite, A. M., Babin, M., & Stemmann, L. (2021). Marine snow morphology illuminates the evolution of phytoplankton blooms and determines their subsequent vertical export. Nature Communications, 12(1), 2816. https://doi.org/10.1038/s41467-021-22994-4

Turner, J. T. (2015). Zooplankton fecal pellets, marine snow, phytodetritus and the ocean's biological pump. Progress in Oceanography, 130, 205–248. https://doi.org/10.1016/j.pocean.2014.08.005

Venables, H., Meredith, M. P., Atkinson, A., & Ward, P. (2012). Fronts and habitat zones in the Scotia Sea. Deep-Sea Research Part II: Topical Studies in Oceanography, 59–60, 14–24. https://doi.org/10.1016/j.dsr2.2011.08.012

Westberry, T. K., & Siegel, D. A. (2006). Spatial and temporal distribution of *Trichodesmium* blooms in the world's oceans. Global Biogeochemical Cycles, 20(4), GB4016. https://doi.org/10.1029/2005GB002673

Chapter 4: Impact of biogeochemical provinces and carbonate saturation state on marine particle and plankton morphology in the deep sea: contrasting the Atlantic and Pacific Oceans

4.1 Abstract

Surface production supplies material that sinks into the deep ocean as marine particles. Few full-depth, ocean-basin-wide measurements exist to describe the abundance and distributions of marine particles and plankton. In this study, we (1) describe the relationship of biogeochemical provinces to marine plankton and particle communities, (2) investigate variations in marine particle communities within biogeochemical provinces, and (3) test the impact of carbonate saturation state on living plankton abundance and detrital particle morphology in the Atlantic and Pacific Oceans. We deployed a plankton and particle imaging system (UVP5) on a CTD during two U.S. GO-SHIP cruises (i.e., A22 in the Atlantic and P02 in the Pacific). We classified 1.4 million images into 46 detrital and 61 living categories and found that marine particle communities were differentiated by biogeochemical province, particularly in the epipelagic. We found some patchiness within provinces, such as a seamount in the subtropical Pacific gyre associated with a biological hotspot and strong export event. Finally, our data suggest that plankton distribution and marine particle morphology in the Atlantic Ocean could potentially be more strongly impacted by aragonite and calcite saturation state than in the Pacific Ocean, despite the presence of much shallower aragonite and calcite saturation horizons in the Pacific. We attribute this to calcifying plankton being better adapted to lower calcite and aragonite saturation state conditions in the Pacific Ocean. These results shed light on how biogeochemical provinces in the tropical and subtropical Pacific and Atlantic influence patterns of particle export and remineralization at all depths, with implications for how this influences global biogeochemical cycles.

4.2 Introduction

The ocean is currently a natural sink of atmospheric carbon dioxide. This removal is partially due to the ocean's biological carbon pump, a mechanism that sequesters photosynthetically fixed carbon dioxide into the deep ocean and seafloor (Sarmiento & Gruber, 2006). The biological carbon pump operates by three main mechanisms: gravitational sinking of particulate organic matter, physical mixing and subduction of water containing particulate organic matter, and active

migration of zooplankton either daily or seasonally and subsequent respiration, mortality, and fecal pellet production at depth (Boyd et al., 2019; Iversen, 2023; Le Moigne, 2019). Detrital particulate organic matter takes the form of dead phytoplankton cells, fecal pellets produced by zooplankton, and aggregated detrital matter (Turner, 2015). In general, the deeper detrital particles reach in the ocean before they are remineralized back into dissolved carbon dioxide by heterotrophic respiration, the longer the carbon sequestration times from the atmosphere (Kwon et al., 2009). Additionally, sinking and suspended detrital particles in the deep ocean represent the majority of the base of the food web for deep-dwelling organisms, where sunlight is not present for photosynthesis. Despite many decades of study, there is still substantial uncertainty in our understanding of the biological carbon pump's role in the global carbon cycle. This uncertainty is partly due to the spatial and temporal heterogeneity of the biological carbon pump (Buesseler et al., 2007; Henson et al., 2011; Kelly et al., 2018). As such, global estimates of carbon export out of the euphotic zone due to the biological carbon pump vary by nearly 50% (Dunne et al., 2007; Henson et al., 2012; Laufkötter et al., 2016; Nowicki et al., 2022). Unfortunately, our understanding of carbon sequestration in depths greater than 1000 m, where carbon can be sequestered for timescales of up to millennia (Siegel et al., 2021), is even less understood.

Biogeochemical provinces are used to simplify the spatial heterogeneity of unique physical, chemical, and biological signatures in the global oceans (Longhurst, 2007). These provinces are also used to explain the spatial heterogeneity of the biological carbon pump. There is evidence that different biogeochemical provinces have factors other than unique phytoplankton community structures that affect carbon export efficiency or the ratio between carbon flux out of the euphotic zone and primary production in the euphotic zone (Henson et al., 2019). Lower export efficiency is common in the subtropical gyre biome, whereas higher export efficiency is more common in the tropical coastal biome (Henson et al., 2019). Differences in the abundance and activity of microzooplankton and bacteria drive these differences. In addition to characteristic export efficiencies, biogeochemical provinces have unique seasonal cycles of particle biovolume and slope of the particle size distribution (Clements et al., 2022). The North Pacific subtropical gyre has a relatively flatter slope of particle size distribution, with more larger particles, than the North Atlantic subtropical gyre (Clements et al., 2022). Measuring the

biological carbon pump by biogeochemical province gives us a lens to look for patterns in an ecologically and physically meaningful way while simplifying some of the spatial heterogeneity.

The Atlantic and Pacific Oceans span similar latitudes, and both are strongly impacted at the surface by the Coriolis force and prevailing winds resulting from Hadley cells (Talley et al., 2011). The combination of these physical forces on the ocean sets up a subtropical high-pressure system around 30°, which initiates the subtropical gyres around latitudes 20 – 40° in the northern and southern hemispheres of the Atlantic and Pacific Oceans. While the physical circulation of the gyres is similar in the upper 1000 m, the underlying thermohaline circulation, and thus chemistry, is distinct between the Atlantic and Pacific oceans. Deep water formation in the North Atlantic brings "young" highly oxygenated, low-nutrient water from the surface to the seafloor (Sarmiento & Gruber, 2006). This water mass slowly flows south, merging with the eastward-flowing Southern Ocean. Some of this water will become Antarctic Bottom Water (AABW) (Talley, 2013). Some of the AABW will split in the Pacific Sector of the Southern Ocean and flow northward through the Pacific Ocean (Talley, 2013). When the water hits the continental shelf bordering northern Asia and North America, it shoals and eventually reaches the surface, where it warms and flows south down the eastern Pacific. It takes about 1000 years from when water is subducted in the North Atlantic until it resurfaces in the North Pacific (England, 1995). During this time, the water ages. Older water is depleted in oxygen as microbes respire sinking organic material, releasing dissolved nutrients and carbon dioxide into the deep ocean (Sarmiento & Gruber, 2006). Older water has more inorganic carbon and a lower pH; therefore, the aragonite saturation horizon of the Pacific Ocean's subtropical gyre is located around 200 – 500 m (Feely et al., 2002), much shallower than in the Atlantic Ocean's subtropical gyre, which is located around 3000 m (Chung et al., 2003).

The northern Atlantic and Pacific oceans have biogeochemical provinces classified as Westerlies, Trades, and Coastal, with distinct biology between these ocean basins based on differences in geochemistry. Coastal provinces such as the Northwest Atlantic Shelves Province and the California Upwelling Coastal Province are known for very high primary productivity composed primarily of diatoms (Morrow et al., 2018; Mouw & Yoder, 2005), with high and efficient carbon flux (Siegel et al., 2014). Trade wind provinces, including the Caribbean, North Atlantic Tropical Gyral, and North Pacific Tropical Gyre Provinces, are known for low to moderate productivity rates (Finenko et al., 2003; Huston & Wolverton, 2009; Kodama et al.,

2021) and low carbon fluxes (Siegel et al., 2014). Similar to the Trade provinces, the Westerlies provinces, such as the North Atlantic Subtropical Gyral Province West and the North Pacific Subtropical Gyre Province West, are known for lower productivity rates (Finenko et al., 2003; Karl, 1999) and low carbon fluxes (Siegel et al., 2014). Where Westerly provinces intersect with western boundary currents such as the Gulf Stream and Kuroshio, cold core rings can have elevated primary. Carbon flux is low to moderate (Siegel et al., 2014) and tends to be higher in the more productive Kuroshio region compared with the Gulf Stream. These differences in surface communities, productivity, and carbon export are well-documented; however, how these factors and differences in marine chemistry influence the morphology of marine particles sinking out of the euphotic zone into the meso- and bathypelagic is not well-constrained.

In-situ imaging technologies, like the Underwater Vision Profiler 5 (UVP5), sample delicate marine snow particles without damaging them (Lombard et al., 2019; Picheral et al., 2010). The increasing computational power of personal computing devices and improvements in deep learning technology are allowing particles to be categorized into more categories, more accurately, and more quickly than previously possible (Irisson et al., 2022). Using unsupervised clustering within a convolutional neural network framework allows for images to be clustered into data-driven categories much more quickly and accurately than with traditional random forest prediction and manual validation (Schröder et al., 2020). This is helpful because different particle types have different mineral content, shape, densities, and porosities, all of which affect size-specific carbon content, sinking speed, and remineralization rates (Armstrong et al., 2002; Iversen & Lampitt, 2020; De La Rocha & Passow, 2007). Additionally, a fecal pellet has a different source than an aggregate made up of phytoplankton material even though the two can overlap in particle size (Turner, 2015). Marine snow particles imaged as Arctic as sea ice retreated and categorized into ecologically meaningful functional morphotypes demonstrated the different morphotypes behave differently both spatially and temporally (Trudnowska et al., 2021). These new techniques allow us to classify marine snow quickly and accurately into ecologically meaningful categories that have implications for particle carbon content, porosity, and sinking speed that go beyond the size-specific metrics that have historically been used.

This study used the U.S. GO-SHIP platform to sample and classify marine snow into 105 ecologically meaningful classifications of detritus and living plankton on an ocean basin-wide, full-depth scale. We imaged marine particles with a UVP5 High-Definition unit on two U.S. GO-

SHIP Cruises in 2021 and 2022 in the North Atlantic and North Pacific oceans, respectively. We apply statistical tests to determine if the distribution of different types of marine snow is distinct at different depths or in different biogeochemical provinces. Additionally, we explore the role of differing Atlantic and Pacific Oceans' chemistries to determine if different carbonate saturation state patterns impact calcifiers' distributions and marine particle morphology in the deep sea.

4.3 Methods

4.3.1 Study Area and Data Collection

Data from this study were collected with the U.S. Global Ocean Ship-based Hydrographic Investigations Program (GO-SHIP) on the A22 cruise from April to May 2021 on the R/V Thompson and the P02 cruise from May to July 2022 on the R/V Revelle (Table 4.1, Figure 4.1). The A22 cruise was a latitudinal cruise from Venezuela to the northeastern United States, primarily along 65°W. P2 was a longitudinal cruise from Japan to the southwestern United States, primarily along 30°N.

The CTD unit consisted of a Seabird SBE911plus, a WetLabs ECO-FL-RTD fluorometer, and an SBE43 dissolved oxygen sensor. A Cstar transmissometer was also mounted to the CTD rosette package. The high-definition UVP5 SN-201 attached to the CTD rosette package sampled the water column down to 6000 m in tandem with the other sensors on the CTD. UVP5 SN-207 images a water volume of 0.88 L at up to 6 Hz, capturing all the particles 0.06 – 27 mm in ESD within each image (Picheral et al., 2010). We collected 90 UVP profiles during the A22 cruise and 208 UVP profiles during the P2 cruise. Oxygen sensor calibrations were refined as bottle oxygen results became available.

Table 4.1: Cruise and image metadata.

Cruise Name	Date Range	Latitude Range	Longitude Range	Number of Stations	Number of Images
A22	April 22 – May 15, 2021	12 N – 40 N	64 W – 70 W	90	628,260
P02	May 1 – July 15, 2022	24 N – 33 N	133 E – 117 W	208	750,290

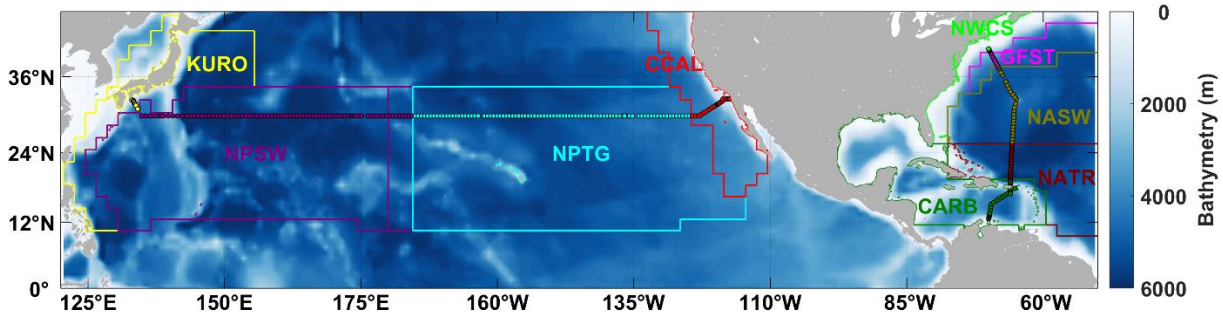

Figure 4.1: Map with biogeochemical provinces and stations. Sampling stations are shown from two U.S. GO-SHIP cruises: P2 (left), a latitudinal cruise (~30°N) in the Pacific Ocean sampled during the spring and summer of 2022 from Japan to the United States, and A22 (right), a primarily longitudinal cruise (~64°W) in the Atlantic Ocean sampled during the spring of 2021 from the United States to Venezuela in colored circles. Bathymetry is indicated in shades of blue. Biogeochemical Province locations are outlined and labeled (Longhurst, 2007). Each station is assigned to a province and shaded by that province. Abbreviations are defined in section 4.3.2.

4.3.2 Environmental Conditions

We used previously defined biogeochemical provinces (Longhurst, 2007), commonly used in other studies (Finenko et al., 2003; Sun & Wang, 2017). It should be noted that the province boundaries, as used in this study, are approximate locations only and that these boundaries vary seasonally (Reygondeau et al., 2013). Additionally, the provinces used in this study are determined by the epipelagic zone; mesopelagic provinces are similar, though not identical, to epipelagic provinces (Sutton et al., 2017; Reygondeau et al., 2018). In the Pacific, we crossed four biogeochemical provinces. From west to east, these are the Kuroshio Current Province (KURO), North Pacific Subtropical Gyre Province West (NPSW), North Pacific Tropical Gyre Province (NPTG), and California Upwelling Coastal Province (CCAL). In the Atlantic, we crossed five biogeochemical provinces. From north to south, these are the Northwest Atlantic Shelves Province (NASW), Gulf Stream Province (GFST), North Atlantic Subtropical Gyral Province West (NASW), North Atlantic Tropical Gyral Province (NATR), and Caribbean Province (CARB). These biogeochemical provinces fit into three global province types: Westerlies (i.e., KURO, NPSW, NASW, and GFST), Trades (NPTG, CARB, and NATR), and Coastal (CCAL and NWCS).

Four inorganic carbon parameters, including total carbon dioxide, pH, total alkalinity, and the partial pressure of carbon dioxide, were collected from bottle samples and measured on board during each cruise. Nutrients, including total phosphorous and silica, were collected from the

same bottles and measured on board using a Seal Analytical continuous-flow AutoAnalyzer 3. The Standard Operating Procedures for every measurement made on the A22 cruise (Menezes, 2022), P02 Leg 1 cruise (Macdonald, 2022), and P02 Leg 2 cruise (Thurnherr, 2022) are available online. At every other station, a total of 36 bottle samples were collected at approximately every 20 m from 0 – 100 m, 50 m from 100 – 500 m, 100 m from 500 – 2000 m, and every 200 to 300 m below 2000 m. At the other stations, a total of about 10 bottle samples were collected at approximately the following resolution: 5 m, 75m, 150 m, 200 m, 350 m, 500 m, and approximately every 700 – 1000 m to the seafloor. These specific depths varied for each station to improve the interpolation across the transect. We used the CO2Sys Excel Macros (Pierrot et al., 2006) to calculate the saturation state (Ω) of aragonite and calcite. Our input conditions were salinity from the CTD data files, temperature of 25°C, and pressure of 0 dbars (as all the analyses were performed at this temperature and pressure), total phosphorous, total silica, and all four inorganic carbon parameters, when available. The output conditions were the in-situ temperature and pressure from the CTD data files. We removed all flagged data for all input and output conditions. We used the following scales and constants: total scale (mol/kg-SW) for the pH scale, K1 and K2 from Lueker et al., 2000 for CO_2 Constants, Dickson KSO_4 source, and Lee et al., 2010 for the total boron source.

4.3.3 Particle Data and Image Processing

The UVP initial particle data processing and image classification was performed as in O'Daly et al. (Chapter 3). In brief, particle size, abundance, and biovolume were processed using the Zooprocess Version 7.39 software and published to the Ecotaxa website (https://ecotaxa.obs-vlfr.fr/prj/9566) (Picheral et al., 2017; Picheral et al., 2010). Transect plots of particle abundance, biovolume, and mean size were created in Matlab R2019a. The grey-scale JPEG images of particles larger than ~ 1 mm were used to identify the particle's type. We used the Morphocluster protocol to determine the particle type for each UVP image (Schröder et al., 2020). An instrument malfunction during the Pacific cruise delayed our ability to access data after station 57. These data were not included in the Morphocluster run. After 91% classification in Morphocluster with the images in the run, we imported the data to Ecotaxa using existing categories and visually inspected each category. We uploaded the data after station 57 on the Pacific cruise (a total of 750,290 images, increasing the total number of images included in the Morphocluster run by 13%) to combine the new images with the remaining unclassified images.

When the validated data in each category was considered clean (<5% error, see Section 3.3.4 for more details), we used the validated images to predict the remaining images into one of the categories. The error of the final predictions of the images was not analyzed; however, it is assumed not to contribute substantially to the overall error rate of the classifications because it represents a small percentage of the images. We combined many categories into eight super-categories for plotting in this manuscript: fluffy aggregates, dense aggregates, fibers, fecal pellets, photosynthetic particles, crustaceans, rhizarians, and gelatinous zooplankton. Every Ecotaxa category and, when relevant, its super-category is listed (Table B1).

4.3.4 Statistical Analysis

A principal component analysis (PCA) was performed to compare marine particle communities in different biogeochemical provinces. The covariance matrix was calculated using the function *PCA* in the FactoMineR package in R using the default setting with variables scaled to unit variance. Each sample in this analysis is a marine particle community that represents the abundance of each of the eight particle super-categories in each CTD cast averaged over the following depth bins: 0 - 50 m, 50 – 100 m, 100 – 200 m, 200 - 500 m, 500 – 1000 m, 1000 – 2000 m, 2000 – 3000 m, 3000 – 4000 m, 4000 – 5000 m, and 5000 – 6000 m. Depth, latitude or longitude (depending on the ordination of the cruise transect), total particle abundance, total particle biovolume, slope of total particle size distribution, mean total particle size, temperature, salinity, oxygen, fluorescence, transmission, saturation state of aragonite, and saturation state of calcite were plotted as quantitative supplementary variables to see how those variables correlate with the different marine particle types.

4.4 Results and Discussion

4.4.1 Particle and Water Properties

Biogeochemical provinces were associated with different patterns in total particle abundance, biovolume, and average particle size in the Atlantic and Pacific Oceans (Figures 4.2a – 4.2f). In both oceans, particle abundance was high near the coasts and in the surface ocean (Figures 4.2a and 4.2b). The Atlantic Ocean had a much higher total particle abundance, reaching over 60 particles per liter, whereas the Pacific Ocean peaked at around 25 particles per liter (Figure 4.2a). The Atlantic Ocean had elevated particle abundance down to about 1000 m and very low

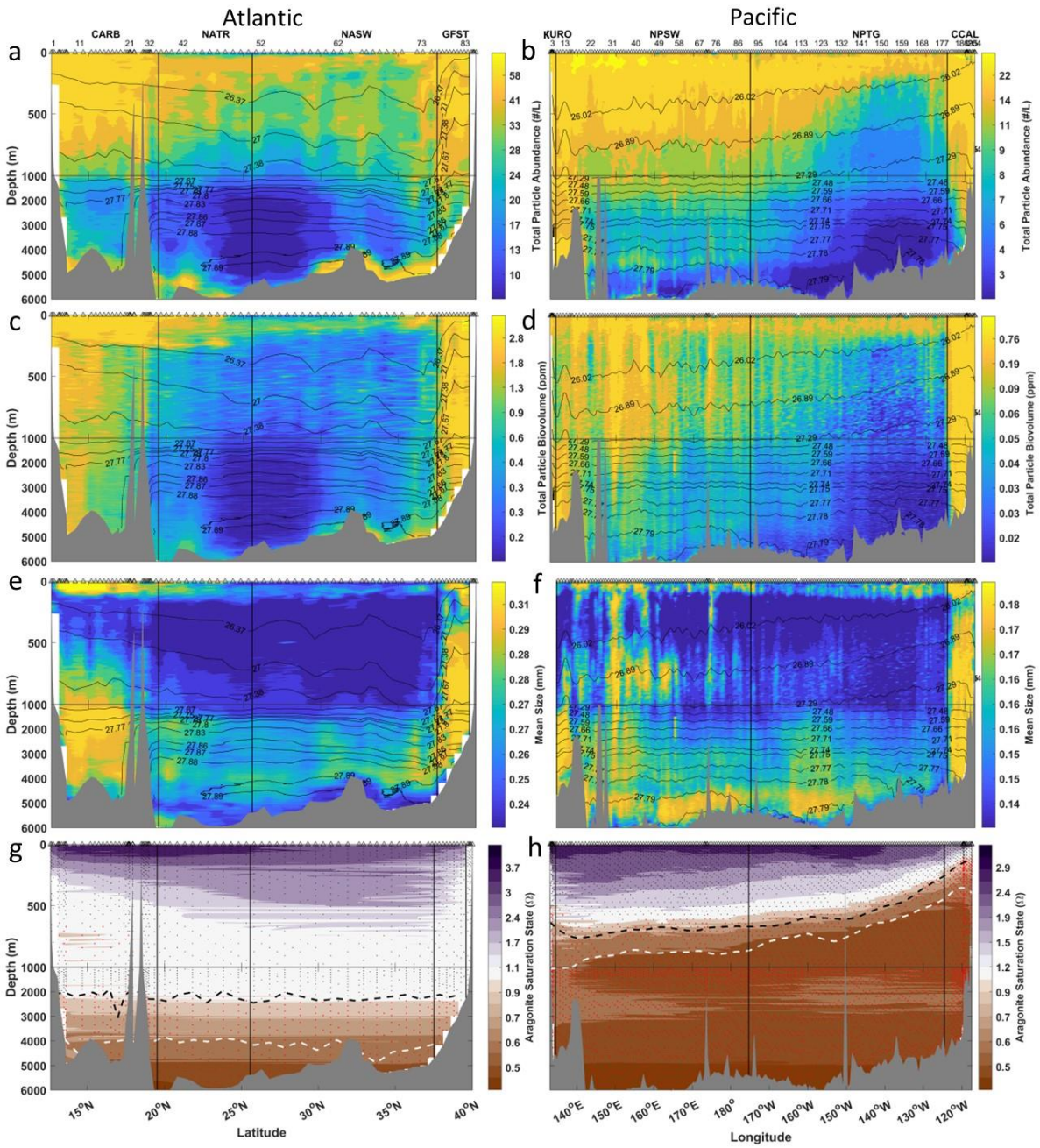

Figure 4.2: Spatial distributions of particle and water properties in the Atlantic and Pacific Oceans. Section plots of (a and b) total particle abundance in #/L, (c and d) total particle biovolume (ppm), (e and f) mean size (mm), and (g and h) aragonite saturation state (in Ω). The Atlantic Ocean (A22) is shown in panels a, c, e, and g and the Pacific Ocean (P02) is shown in panels b, d, f, and h. The locations of samples are marked on the top of each panel with black triangles. In panels a-f, Sigma-theta is shown in black contour lines. The black dashed line in panels g and h indicates the aragonite saturation horizon (Ω = 1) and the white dashed line indicates the calcite saturation horizon. Dots indicate sample locations used to calculate saturation state; black dots have an aragonite saturation >1, and red dots <1. The approximate locations of Biogeochemical Provinces are marked with vertical black lines and labeled on top – see text for acronyms.

abundance below 2000 m in the subtropical gyres (NATR and NASW provinces). It is somewhat unexpected that the surface of the Caribbean and Gulf Stream provinces had among the highest particle abundances observed in both cruises because surface waters in these regions are highly oligotrophic (Forget et al., 2011; Zhu et al., 2024), especially compared to the California Upwelling Coastal Province, which can have periods of upwelling during the summer (Jorgensen et al., 2024). There was also a thick nepheloid layer, especially north of 30°N and south of 23°N. In fact, the highest total particle abundance in both cruises was found in the nepheloid layer around 37°N. A pronounced nepheloid layer, or layer of water above the ocean floor that contains significant amounts of suspended sediment, has been described previously in this region (Gardner et al., 2018) and has been attributed to overlying areas with high surface eddy kinetic energy (Gardner et al., 2018).

In the subtropical gyre in the Pacific Ocean, there was high particle abundance down to about 2000 m within the western side (NPSW province) (Figure 4.2b), while within the eastern side (NPTG), there was a strong, nearly linear gradient in total particle abundance moving from 2000 m in the western portion and up to 250 m in the eastern boundary. The Pacific transect had almost no nepheloid layer in contrast with the Atlantic. In both oceans, total particle biovolume followed a similar pattern as total particle abundance (Figures 4.2a-4.2d). The nepheloid layer was less pronounced in total biovolume in the Atlantic Ocean (Figure 4.2c). The mean particle size in both oceans was larger in the upper 100 m, greater than about 0.27 mm in the Atlantic and 0.16 mm in the Pacific (Figures 4.2e and 4.2f). Mean particle size was elevated at all depths in the GFST and CCAL provinces (Figures 4.2e and 4.2f). This is expected as carbon export is known to be higher and more efficient in these provinces compared to the gyre provinces (Henson et al., 2019; Siegel et al., 2014).

In the CARB province, there was a mesopelagic particle size minimum from about 100 m to 600 m and particle size was elevated below 600 m (Figure 4.2e). This pattern potentially indicates a previous export event where larger particles previously sank to deeper depths or maybe there was enhanced physical aggregation of smaller particles below 6000 m. In the NATR and NASW, particle size was a bit elevated below 1500 m down to the nepheloid layer, where it lowered substantially (Figure 4.2e), cementing the fact that this nepheloid layer is made up of abundant small particles that comprise little biovolume. In the NPSW, patches of elevated mean particle size from 100 m to 3000 m around stations 31 and 76 (Figure 4.2f). These could reflect

anomalous pulsed export events. Below 3000 m in all provinces in the Pacific, mean particle size was elevated down to the seafloor (Figure 4.2f).

Biogeochemical provinces are also, to some degree, associated with different patterns in the aragonite saturation state in the Atlantic and Pacific Oceans (Figures 4.2g and 4.2h). In the Atlantic Ocean, the aragonite saturation horizon was located at about 2000 m depth throughout the transect (Figure 4.2g). There was a small section of water south of 20 deg N with a localized aragonite saturation horizon from about 500 m to 1000 m. The calcite saturation horizon was located at about 4000 m throughout the transect. This pattern was very different in the Pacific Ocean, where the aragonite saturation horizon was located around 750 m on the westernmost portion of the transect and shoaled to about 100 m at the California coast on the easternmost portion (Figure 4.2h). The calcite saturation horizon had a similar pattern, but it is slightly deeper, starting at about 1000 m on the westernmost portion of the transect and shoaled to around 500 m on the coast of California. This difference in aragonite and calcite saturation was expected based on the deep circulation of the two basins (Sarmiento & Gruber, 2006; Talley et al., 2011) but provides an interesting contrast for understanding the impacts of saturation state on particle morphology.

We investigated particle morphology using in-situ imaging. Large particles greater than about 1 mm were classified by morphology and presented in 8 super-categories (Figure 4.3, 4.4). We first present the results from "younger" water in the Atlantic Ocean. Fluffy aggregates were the most numerous particle type in the Atlantic Ocean, with the highest observed abundance of over 40,000 fluffy aggregates m^{-3} (Figure 4.3a). Their distribution was similar to total particle abundance but differed in a few notable areas, mostly explained by the lower detection limit of the camera system. Fluffy aggregates were most common in the upper 500 m across the transect. Fluffy aggregates in the Caribbean and Gulf Stream Provinces had relatively high abundances (~ 200 m^{-3}) down to the seafloor. There is an apparent break at 500 m, and below that, fluffy aggregates were in low abundance in the North Atlantic Tropical and Subtropical Gyral Provinces. We investigated if this was due to a malfunction in the UVP sampling and found that the volume of water sampled was consistent below the upper 100 m, where the CTD descended at a slower rate (Figure C.1), supporting the conclusion that the instrument sampled as expected. The pycnocline in this region is within the upper 200 m of the water column and is unlikely influencing the pattern in fluffy aggregate abundance. While fluffy aggregate abundance

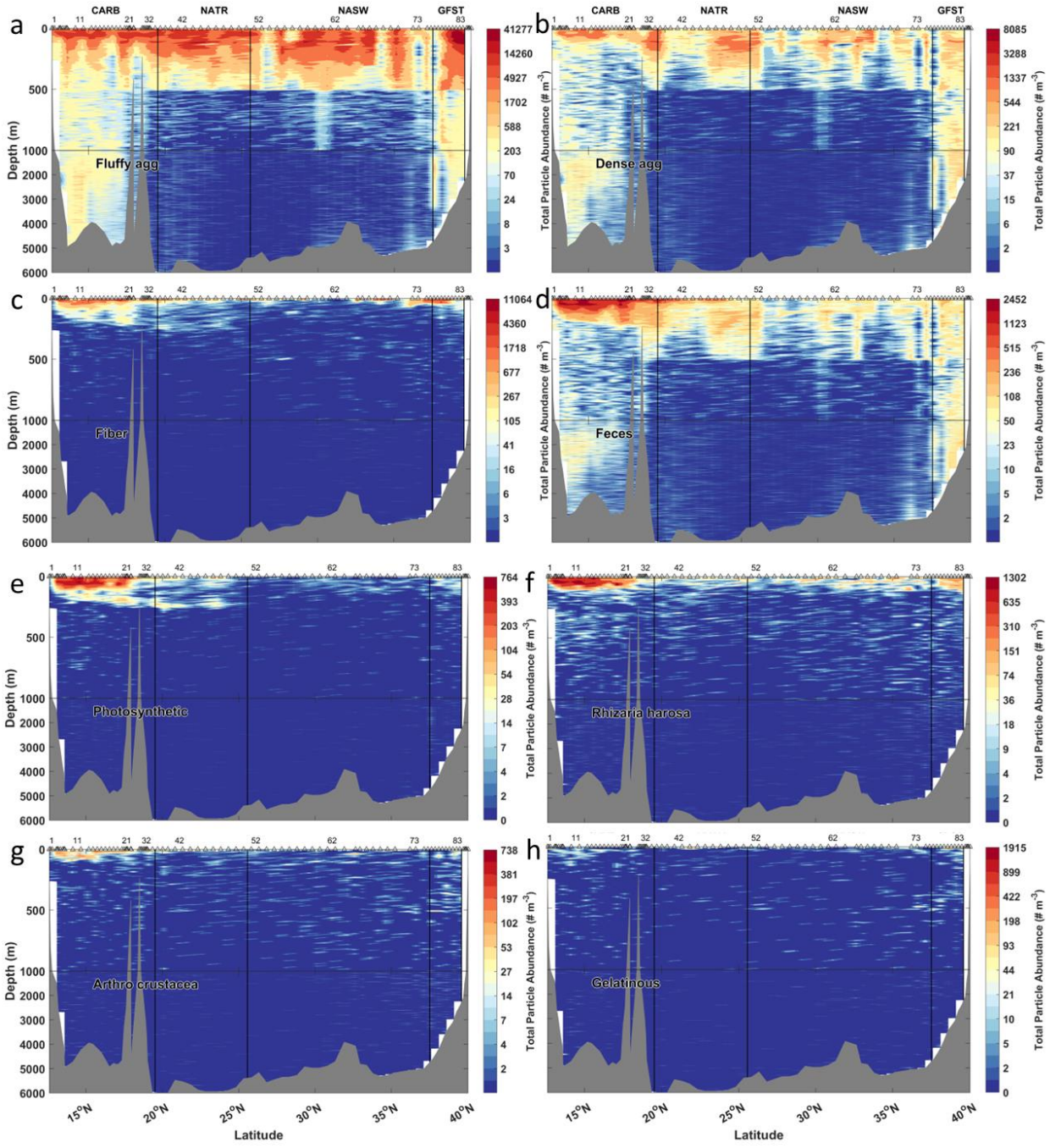

Figure 4.3: Spatial distribution of particles by particle type in the Atlantic Ocean (A22). Section plots of the concentration of detrital particles over depth: (a) fluffy aggregates, (b) dense aggregates, (c) fibers, and (d) feces. Section plots of the concentration of living (e) photosynthetic particles, (f) rhizarians, (g) crustaceans, and (h) gelatinous particles are shown over depth. The approximate locations of Biogeochemical Provinces are marked with vertical black lines and labeled on top. See text for acronyms. Locations of samples are marked on the top with black triangles.

decreased at 500 m, total particle abundance was elevated down to about 1000 m, rather than 500 m, in these provinces (Figure 4.2a). Many of these particles between 500 and 1000 m were likely small fluffy aggregates, below the lower limit for images of the UVP. Therefore, we attribute the apparent break in the abundance of fluffy aggregates to the lower limit for images of the UVP, not to a dramatic decrease in all fluffy aggregates at 500 m.

Dense aggregates and feces had a similar pattern as fluffy aggregates but at lower magnitudes (Figure 4.3b and 4.3d). However, dense aggregates were more abundant than feces. In the Caribbean Province, there was low total particle abundance below 1000 m until the nepheloid layer started around 1000 m above the seafloor (~4000 m). This region of low total particle abundance from about 1000 to 4000 m in the Caribbean Province had relatively high fluffy aggregate, dense aggregate, and feces abundance. This may be indicative of an older export event, as previous analysis from the Southern Ocean has indicated (Chapter 3). Fibers had the second highest abundance of any particle type in the Atlantic Ocean of over 10,000 fibers m^{-3} (Figure 4.3c). Fibers were almost all located in the upper 250 m, particularly in the Caribbean and North Atlantic Tropical Gyral Provinces and in the upper 100 m in the North Atlantic Subtropical Gyral and Gulf Stream Provinces. Fibers were most numerous in the Caribbean and Gulf Stream Provinces. These patterns provide more data that these fibers are likely living diatom chains, similar to previous findings (Chapter 3, Ohman & Browman, 2019). The low export signature of the subtropical gyre in the two gyre provinces is strongly supported by low abundances of total particles and all detrital particle types (Siegel et al., 2014).

Across super-categories, living plankton had lower abundances than all detrital particles (Figure 4.3e-4.3h). All living particle types had relatively similar distributions, with the highest abundances in the epipelagic. Photosynthetic particles from UVP images were nearly all “puff” and “tuft” varieties of colonial *Trichodesmium*, a filamentous cyanobacteria known to be in high abundance in the North Atlantic Subtropical Ocean throughout nearly all our cruise transect (Capone et al., 1997). Photosynthetic particles had the most similar distribution to fibers, with high abundances of photosynthetic particles down to about 250 m in the Caribbean, as expected (Capone et al., 1997), and moderate abundances down to about 250 m in the North Atlantic Tropical Gyral Province (Figure 4.3e), further supporting the hypothesis that “fibers” captured in these images may be living diatom chains (Ohman & Browman, 2019). Photosynthetic particles

were nearly absent from the North Atlantic Subtropical Gyral Province. Due to the lower detection limit of the UVP camera, pico- and nanophytoplankton are not imaged by the UVP unless they colonize or aggregate into large particles. As pico- and nanophytoplankton are common in the Atlantic subtropical gyre, it is unsurprising that there were not many images of photosynthetic particles. They were present in moderate abundances down to about 200 m in the Gulf Stream Province.

Particles identified as rhizarians had a similar pattern as photosynthetic particles; they were most abundant in the upper 150 m of the Caribbean province, low to moderate in the upper 150 m of the North Atlantic Tropical Gyral Province, moderate in the upper 150 m of the North Atlantic Subtropical Gyral Province, and slightly higher in the upper 150 m of the Gulf Stream Province (Figure 4.3f). There was a patchy distribution of rhizarians below 150 m in all provinces. These patterns are somewhat supported by the modeled distribution of solitary collodarians that are higher biomass in the upper 200 m compared to 200 – 500 m, except that solitary collodarians were found in relatively similar biomass within the gyre and in the Gulf Stream and the Caribbean in the upper 200 m (Drago et al., 2022). Solitary collodarians are not a good representation of all rhizarians; however, there are limited studies of total rhizarian abundance in this region. Rhizarians reached the highest abundance of any living particle type, reaching 1300 cells m^{-3}, similar to previous findings that rhizarians can have a similar abundance to all mesozooplankton in the tropics and subtropics (Biard et al., 2016).

Crustaceans had the highest abundances in the upper 100 m in the Caribbean province, low abundances at all depths in the gyre provinces, and patchy moderate abundances down to about 500 m in the Gulf Stream Province (Figure 4.3g). These are expected patterns based on previous observations (Almazán et al., 2022; Drago et al., 2022; Wiebe et al., 1976). Gelatinous zooplankton had a relatively high but patchy abundance, mostly closer to the coasts in the Caribbean and Gulf Stream Provinces, but still relatively more dispersed throughout the water column, particularly in the upper 1000 m. Gelatinous zooplankton have been shown to have very low biovolumes in the epipelagic in the subtropical gyre in the North Atlantic previously (Lilley et al., 2011). These results likely underestimate true crustacean abundance, as crustaceans perform some avoidance behaviors of the descending UVP5 mounted to the CTD rosette (Geoffroy et al., 2021). Additionally, the UVP5 samples much less water volume than

zooplankton nets that results in undercounting the relatively low abundance of crustaceans and gelatinous zooplankton (Romagnan et al., 2016).

Next, we present the results from "older" water in the Pacific Ocean (Figure 4.4). Fluffy aggregates were the most numerous particle type in the Pacific Ocean, with the highest observed abundance of 3550 m^{-3} in the surface of the western portion of the North Pacific Subtropical Gyre Province, but they did not have a homogenous distribution throughout the province. Fluffy aggregates were moderately abundant below 1000 m west of station 13. They had high abundance from about stations 15 to 55 from the surface to 1000 m, with some bands of lower particle abundance. Below 1000 m at these stations, fluffy aggregate abundances were elevated. East of station 55, generally, there was a moderate abundance of fluffy aggregates in the upper 100 m (~ 50 m^{-3}). The North Pacific Tropical Gyre Province was homogenous in fluffy aggregate distribution: there was a moderate abundance of fluffy aggregates in the upper 100 m with slightly elevated abundances from 500 – 1000 m. Fluffy aggregates were very common at all depths in the California Province (~ 200 m^{-3}) and slightly higher on the surface (~ 600 m^{-3}) and had the most similarity to the total particle abundance of any province. The Kuroshio Current Province had a high abundance of fluffy aggregates in the upper 150 m (~ 500 m-3), then low to moderate abundances below 150 m (~ 5 m^{-3}). This is a bit unexpected as this is considered a high-flux province (Siegel et al., 2014), though possibly the sinking particles were too small to be imaged. Additionally, we sampled a snapshot in time, and export is episodic and often seasonally variable (Conte et al., 2001; Karl et al., 2021), which could explain the low fluffy aggregate abundance observed in the Kuroshio Current Province.

The fluffy aggregate distribution was distinct from total particle abundance (Figure 4.2b), particularly in the Kuroshio Current, which had elevated total particle abundance at all depths, and in the upper 1000 m of the North Pacific Subtropical Gyre, which had elevated total particle abundance across the whole province. These particles were likely below the lower limit for images of the UVP. Dense aggregates and feces had a similar pattern as fluffy aggregates but at lower magnitudes (Figure 4.3b and 4.4d). Dense aggregates had a slightly higher abundance (reaching over 2300 m^{-3}) than feces (reaching over 1500 m^{-3}). Dense aggregates and feces also had a more pronounced mesopelagic band of elevated particles from about 500 – 1000 m than fluffy aggregates, especially in the North Pacific Subtropical Gyre and the western half of the

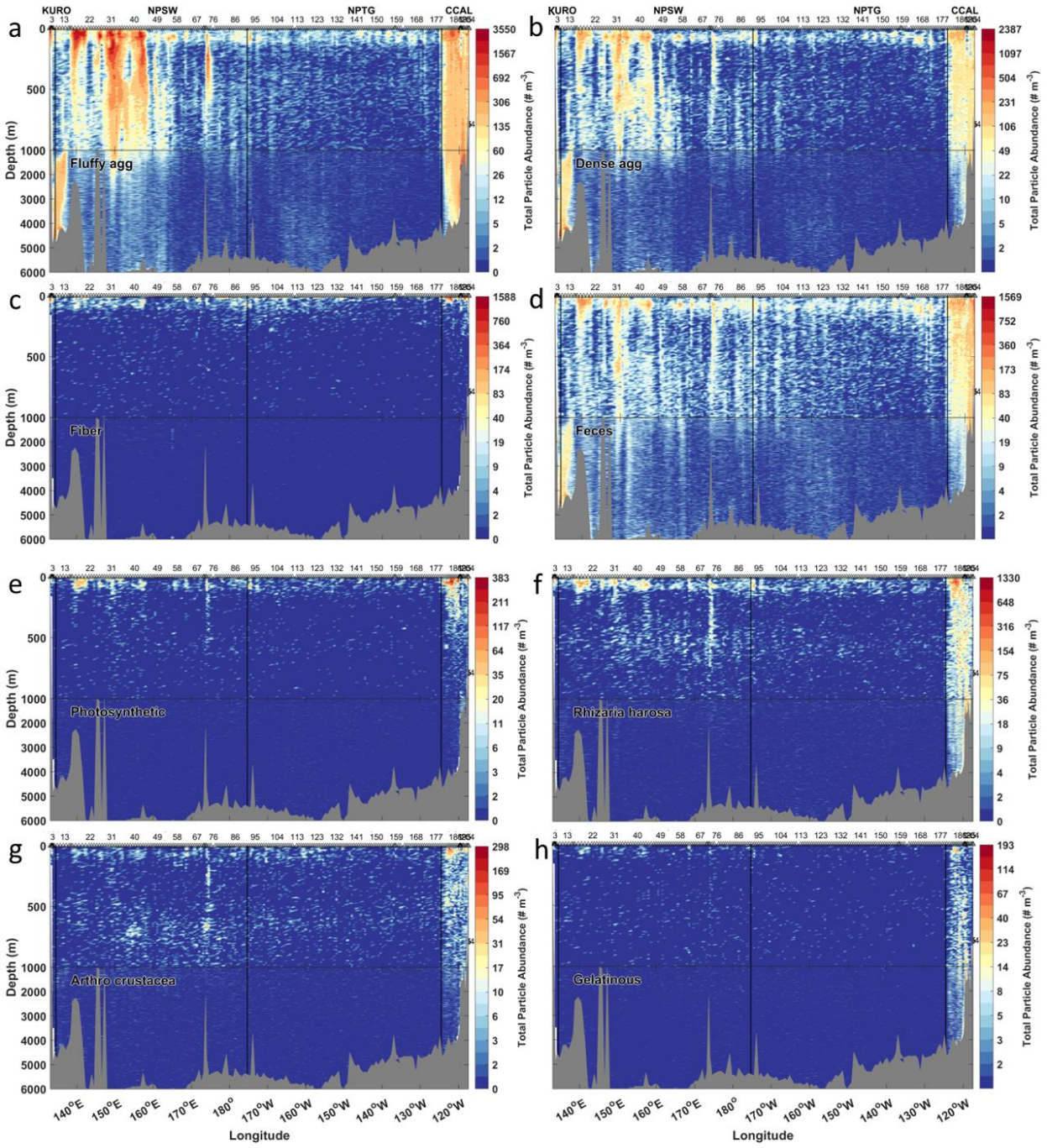

Figure 4.4: Spatial distribution of particles by particle type in the Pacific Ocean (P2). Section plots of the concentration of detrital particles over depth: (a) fluffy aggregates, (b) dense aggregates, (c) fibers, and (d) feces. Section plots of the concentration of living (e) photosynthetic particles, (f) rhizarians, (g) crustaceans, and (h) gelatinous particles are shown over depth. The approximate locations of Biogeochemical Provinces are marked with vertical black lines and labeled on top. See text for acronyms. Locations of samples are marked on the top with black triangles.

Tropical Gyre. Fibers generally had high abundance in the upper 150 m in all provinces but were in the highest abundance in the Kuroshio Current and California Upwelling Coastal Provinces (Figure 4.4c), reaching up to 1600 m^{-3}, two regions that are expected to be more productive and had diatoms (Hasegawa, 2019; Morrow et al., 2018). Again, these provide more data that these fibers are likely living diatom chains, similar to previous findings (Chapter 3, Ohman & Browman, 2019).

Across super-categories, living plankton had lower abundances than all detrital particles in the Pacific (Figure 4.4e-4.4g). All living particle types had relatively similar distributions, generally with the highest abundances in the epipelagic. Photosynthetic particles were generally found in the upper 150 m in the three western provinces (~ 20 m^{-3}). They were in highest abundance in the California Upwelling Coastal Province down to about 300 m (~ 380 m^{-3}), but elevated concentrations persisted to 1000 m (~ 20 m^{-3}), indicating efficient flux of phytoplankton material in this province. Rhizarians and crustaceans had similar distributions (Figures 4.4f and 4.4g), possibly indicating they are grazing on similar food sources or each other. In the North Pacific Subtropical Gyre Province West and North Pacific Tropical Gyre Province, there are two main bands of elevated crustaceans and rhizarians: one in the upper 100 m and one from 500 m to 1000 m. This lower band could be made up of diel vertically migrating organisms (Steinberg & Landry, 2017), or organisms with a mesopelagic depth niche (Biard & Ohman, 2020). Diel vertical migration has been observed within the 500 – 1000 m depth band in the subtropical North Pacific, however migration to 200 m was more common (Sun et al., 2019). However, at Station Aloha, in the subtropical North Pacific, substantial vertical migration to the 500 – 750 m depth band was observed (Steinberg et al., 2008). It is unlikely these mesopelagic crustaceans were in diapause because of the general lack of diapause in juveniles or adults in this region (Baumgartner & Tarrant, 2017). Rhizarians and crustaceans had very high abundances at all depths in the California Upwelling Coastal Province, particularly in the upper 100 m.

Rhizarians were the most numerous of the living categories in the Pacific, further supporting a previous study that rhizarians may have a similar abundance to all mesozooplankton in the tropics and subtropics (Biard et al., 2016). The role of rhizarians as predators, flux feeders, and symbiotic primary producers is likely underestimated due to a lack of study of these protists (Biard, 2022). Gelatinous zooplankton had a patchy distribution in the Pacific, mostly in the

California Upwelling Coastal Province at all depths and in the upper 100 m in the North Pacific Subtropical Gyre Province West. Gelatinous zooplankton are expected to be more abundant in more productive areas, like the California Upwelling Coastal Province (Lucas et al., 2014).

At station 74, around 174°E in the North Pacific Subtropical Gyre Province West, a seamount reached about 2500 m. This seamount appears to be a part of the Hawaiian-Emperor seamount chain, possibly just to the southwest of the Colohan seamount (O'Connor et al., 2013). We observed a strong signal of elevated detrital and living particles in the overlying water at this station. Fluffy aggregates, dense aggregates, and feces are also more abundant from the surface to 800 m (Figures 4.4a, 4.4b, and 4.4d). There were elevated abundances of photosynthetic particles, rhizarians, and crustaceans from the surface to 600 m (Figure 4.4e – 4.4g). It is known that seamounts can affect the physical oceanography of the overlying waters, enhancing mixing (Jiang et al., 2021). These results support previous studies that have identified seamounts as planktonic and upper trophic level biological hotspots (Dai et al., 2022; Haury et al., 2000; Sergi et al., 2020). We passed over other seamounts along this transect (e.g., 145°E, 147°E, and 174°W) and did not observe a signal of elevated particles and plankton. Perhaps the station spacing of approximately 100 nautical miles missed the other seamount signals. Or perhaps there were unique physical or chemical features at the seamount at 174°E that resulted in enhanced particles and plankton.

Finally, we compared detrital particle distributions in the Pacific to the Atlantic. While all detrital particle types had a similar pattern in abundance to total particle abundance in the Atlantic, all detrital particles had a much more distinct pattern in abundance from total particle abundance in the Pacific (Figures 4.2b and 4.4a-4.4d). This was likely due to smaller particles in the Pacific than in the Atlantic (Figures 4.2e and 4.2f) that are more likely to be below the lower size limit for images. In the Atlantic Ocean, the two gyre provinces had the biggest difference between the total particle and fluffy aggregate distribution that we have attributed to small particles in the gyres (Figures 4.2b and 4.3a). This is a likely explanation in the Pacific Ocean as well, and more of these transects were within the gyre because it was a longitudinal transect along 30°N. As in the Atlantic, fluffy aggregates were the most numerous particle type in the Pacific Ocean (Figure 4.4a). However, they were in much lower abundance in the Pacific than in the Atlantic, with the highest observed abundance of about 3500 fluffy aggregates m^{-3}. As

observed in the Atlantic, dense aggregates and feces have a similar pattern as fluffy aggregates but at lower magnitudes and dense aggregates were in higher abundance than feces (Figures 4.4b and 4.4d). Regardless, we observed low export signals (low abundances of total particles and all detrital particle types) from the subtropical gyre in the Atlantic and Pacific, as expected (Siegel et al., 2014), except for maybe the western half of the North Pacific Subtropical Gyre Province west that had elevated detrital particles down to about 1000 m. Also, as observed in the Atlantic, fibers were in the upper 150 m in all provinces but were in the highest abundance in the Kuroshio Current and California Upwelling Coastal Provinces (Figure 4.3c and 4.4c).

All living categories were more numerous in the Atlantic than in the Pacific. The general pattern of higher particle and plankton abundances observed in the Atlantic than in the Pacific is likely due to the orientations of the two transects. The Pacific transect fell along 30°N, a subtropical region that is known for low productivity and low living biomass (Huston & Wolverton, 2009; Karl, 1999), while the Atlantic Transect went from 12°N to 40°N. The temperate zone north of 35°N is known to be much more productive, especially near the coast (Mouw & Yoder, 2005). A region in the Pacific that is more similar to our Atlantic cruise would be the region from Papua New Guinea to northern Japan, which is closer to the western boundary current (Hogg & Johns, 1995). In the Pacific, living plankton were found in generally similar or slightly lower abundances than in the Atlantic, possibly due to either less biomass or less biomass of large plankton groups in the Pacific. Photosynthetic particles were lower in abundance in the Pacific than in the Atlantic (Figure 4.3c and 4.4c), as expected due to known *Trichodesmium* distribution (Capone et al., 1997). *Trichodesmium* is expected to be in both regions (Capone et al., 2005; Karl et al., 1997). However, the region of the Atlantic Ocean that we sampled is more productive than the region of the Pacific Ocean that we sampled (Huston & Wolverton, 2009; Karl, 1999; Mouw & Yoder, 2005), which may explain the pattern we observed. It is also possible that the *Trichodesmium* in the Pacific performed less colonization and formed smaller particles that were not imaged by the UVP.

4.4.2 The role of Biogeochemical Province on Marine Particle Community

To visualize the patterns of particle distributions by depth between the Atlantic and Pacific Oceans, we performed a principal components analysis (PCA) (Figure 4.5). The PCA of the particle assemblages across each transect revealed clustering by depth, particularly with

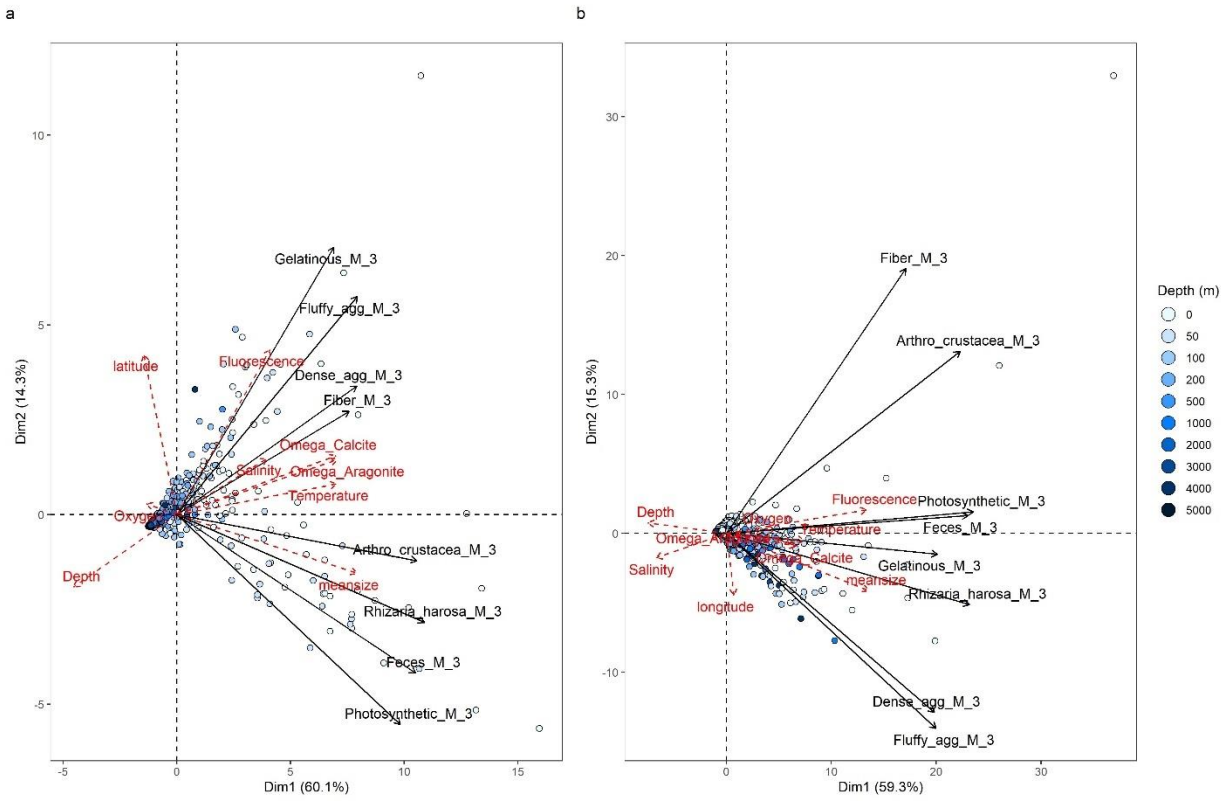

Figure 4.5: Effect of depth on marine particle communities in the Atlantic and Pacific Oceans. Principal components analysis (PCA) of the marine particle communities in the (a) Atlantic Ocean (A22) and (b) Pacific Ocean (P02). Each super-category of marine particles is shown in solid black lines. Individual marine particle communities are shown as small circles colored by depth. Quantitative supplementary variables are shown in a red dashed line. tot_par_abundance: total particle abundance, tot_par_biovolume: total particle biovolume, slope_b: Slope of total Particle Size Distribution, meansize: mean total particle size, Omega_Aragonite: saturation state of aragonite, and Omega_Calcite: saturation state of calcite.

larger differences among particle communities from the upper 200 m than among deep communities in both oceans (Figure 4.5). In the Atlantic Ocean, particle communities split into two groups associated with depth (Figure 4.5a). In shallower depths, gelatinous zooplankton, fluffy aggregates, dense aggregates, and fibers were most abundant, which was associated with fluorescence, higher latitudes, and higher salinity. Crustaceans, rhizarians, feces, and photosynthetic particles were most abundant at slightly deeper depths and were associated with mean particle size and low oxygen. However, all particle types are more abundant in the surface. In the Pacific Ocean, there is less of a clear distinction of marine particle communities by depth than in the Atlantic: many of the samples below 100 m overlapped without a clear delineation by depth (Figure 4.5b). In the Pacific, particle communities split into three groups. Fibers grouped

with crustaceans. Photosynthetic particles, feces, gelatinous zooplankton, and rhizarians grouped together with fluorescence and shallower depths, while dense aggregates and fluffy aggregates grouped together with increasing longitude and total particle abundance. As in the Atlantic, all particle types were more abundant at shallower depths.

Given the large effect of depth on particle community composition (Figure 4.5), we separated out the epipelagic zone (i.e., upper 200 m) and investigated variability by BGC Province (Figure 4.6). In all four panels, depth aligned with the first principal component, indicating it strongly correlated with different patterns in marine particle communities. In the Atlantic surface water, particle communities split into two groups primarily by biogeochemical province (Figure 4.6a). Particle types (i.e., gelatinous, fluffy aggregate, dense aggregate, and fiber) and environmental variables (i.e., fluorescence, increased oxygen, and decreased salinity) were associated with the two northern provinces (Northwest Atlantic Shelves Province and Gulf Stream Province). Crustaceans, rhizarians, feces, and photosynthetic particles were associated with the southernmost Caribbean Province, as were mean particle size, temperature, and higher aragonite/calcite saturation state. The two middle provinces, North Atlantic Tropical and Subtropical Gyral Provinces, fall between these two groups, with Tropical slightly more associated with higher abundances of all particle types than Subtropical. In the Atlantic deep water, dense aggregates and feces were highly correlated and are more common in the two northern provinces (Northwest Atlantic Shelves Province and Gulf Stream Province), as well as increasing particle size (Figure 4.6c). The other group was gelatinous zooplankton, rhizarians, phytoplankton, fibers, crustaceans, and fluffy aggregates which were most common in the Caribbean and North Atlantic Subtropical and Tropical Gyral Provinces and were associated with higher temperature, salinity, and saturation state.

In the Pacific Ocean surface water, the pattern was unexpected because adjacent provinces did not always fall next to each other. KURO and NPSW were most associated with dense aggregates and fluffy aggregates (Figure 4.6b). NPSW had fewer particles than KURO. The next most similar province was CCAL, which was not geographically close to NPSW or KURO. This province had the most photosynthetic particles, feces, gelatinous zooplankton, and rhizarians, as well as elevated fluorescence, cooler temps, lowest calcite/aragonite saturation states, and largest particle sizes. Finally, NPTG had the lowest abundance of all particle types and was associated with the most saline and warmest water and highest saturation state. In the deep Pacific Ocean,

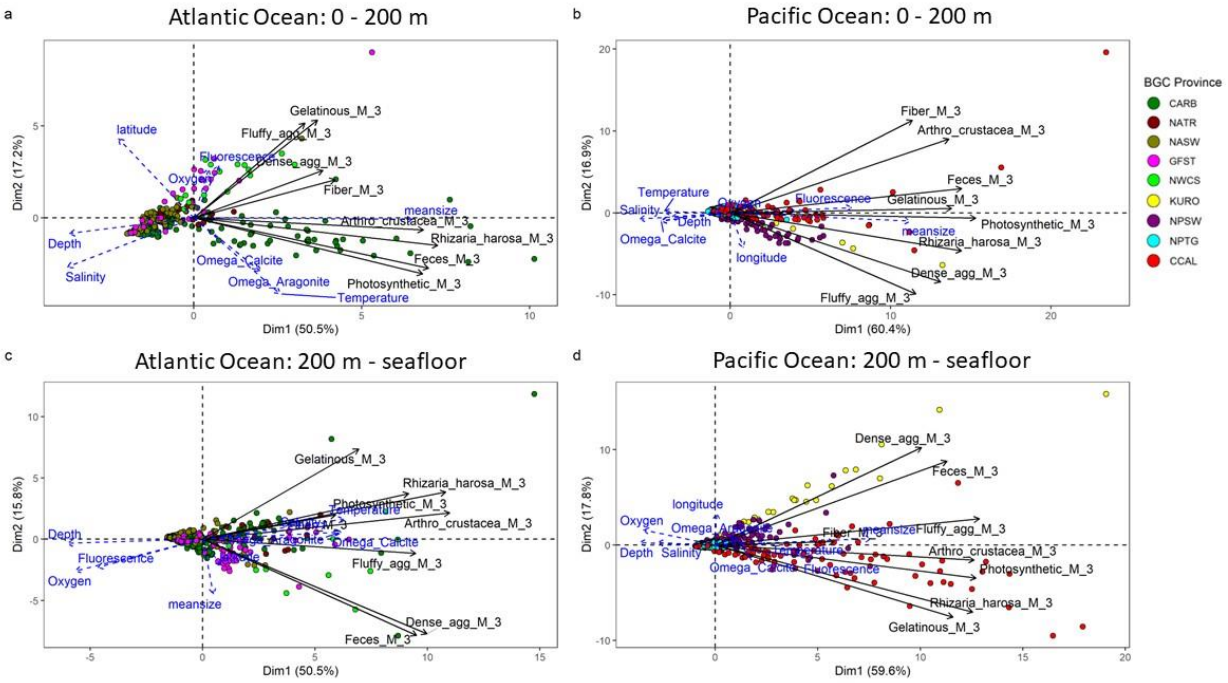

Figure 4.6: Effect of Biogeochemical (BGC) Province on marine particle communities in the Atlantic and Pacific Oceans. Principal components analysis (PCA) of the marine particle communities in the (a and c) Atlantic Ocean (A22) and (b and d) Pacific Ocean (P02). Panels a and b depict the water column above 200 m and panels c and d depict the water column below 200 m. Each super-category of marine particles is shown in solid black lines. Quantitative supplementary variables are shown in a blue dashed line. Individual marine particle communities are shown as small circles colored by Biogeochemical Province. See text for Province acronyms. meansize: mean total particle size, Omega_Aragonite: saturation state of aragonite, and Omega_Calcite: saturation state of calcite.

the pattern was similar to that found in the shallow water (Figure 4.6d). Dense aggregates and feces were most common in Kuroshio Current and the North Pacific Subtropical West Provinces and all other particle types were most common in California Upwelling Coastal Province along with increased particle size, warmest temperature, and low oxygen. The North Pacific Tropical Province still had the lowest abundance of all particle types, as it did in the upper 200 m (Figure 4.6b). Overall, the Atlantic Ocean was much more distinct between the upper 200 m and the lower ocean than the Pacific Ocean. Additionally, particle communities were distinct within each biogeochemical province in the upper 200 m and below 200 m in both oceans. Considering that the biogeochemical provinces are only determined within the epipelagic zone (Reygondeau et al., 2013), it is fascinating to see the marine particle community signature of the province persist to deep depths. The authors are unaware of any other study that has found evidence for signatures of biogeochemical provinces in the bathypelagic zone. Ultimately, we see that marine particle

communities are distinct among the different biogeochemical provinces in both oceans at nearly all depths.

4.4.3 The role of Saturation State on Plankton and Marine Particle Morphology

Some of the taxa identified with UVP images are known to be sensitive to the chemistry of the water, either as organisms with calcium carbonate shells, which are affected by the aragonite and calcite saturation state, or organisms with strontium sulfate skeletons. Acantharians are a rhizarian protist with a strontium sulfate skeleton (Biard, 2022; Brass, 1980). These are heterotrophic, though some are known to have symbiotic relationships with photosynthesizing organisms and thus are considered mixotrophic (Brisbin et al., 2018). Most other rhizarian taxa have silica skeletons (Biard, 2022). Acantharians can regulate their skeletons biologically through biomineralization (Decelle & Not, 2015); however, because strontium sulfate is a rare mineral in the ocean, their skeletons quickly dissolve after they die (Beers & Stewart, 1970). Acantharians were more common in the Pacific than in the Atlantic (Figure 4.7a and 4.7b). The highest abundances were in the Caribbean and California Upwelling Coastal Provinces. Surprisingly, they were in lower abundance in the upper 150 m in both oceans, though previous work has identified these as preferring the upper 100 m (Biard & Ohman, 2020). Their abundances were generally low but evenly distributed down to the seafloor in both oceans (Figures 4.9a and 4.9b). Some studies have shown that ample food availability allows many calcifiers to maintain their shells even in corrosive conditions (Thomsen et al., 2013; Pansch et al., 2014; Leung et al., 2022). The distributions of Acantharians observed indicate that their food source may be abundant enough in either ocean to fight off their skeletons' dissolution.

We also investigated the abundance and distribution of two calcifying taxa: foraminiferans and mollusks (Figure 4.7c – 4.7f). There are about 40 species of planktic foraminifera (Hemleben et al., 1989), most of which have calcite tests (Todd & Blackmon, 1956). In the Atlantic, most of the foraminiferans were observed between 500 and 1000 m, with almost no foraminiferans below the aragonite saturation horizon (Figure 4.7c). However, in the Pacific, foraminiferans were frequently observed, sometimes in high abundance, below both the aragonite and calcite saturation horizons (Figure 4.7d). Foraminiferans were mostly absent from depths > 1000 m in the Kuroshio and North Pacific Subtropical Gyre Provinces. Foraminiferans were more abundant in the North Pacific Tropical Gyre Province, with peaks around 300, 500,

3000, and 4000 m. There were also foraminiferans in the California Upwelling Coastal Province from about 200 – 500 m and from 2000 m to the seafloor.

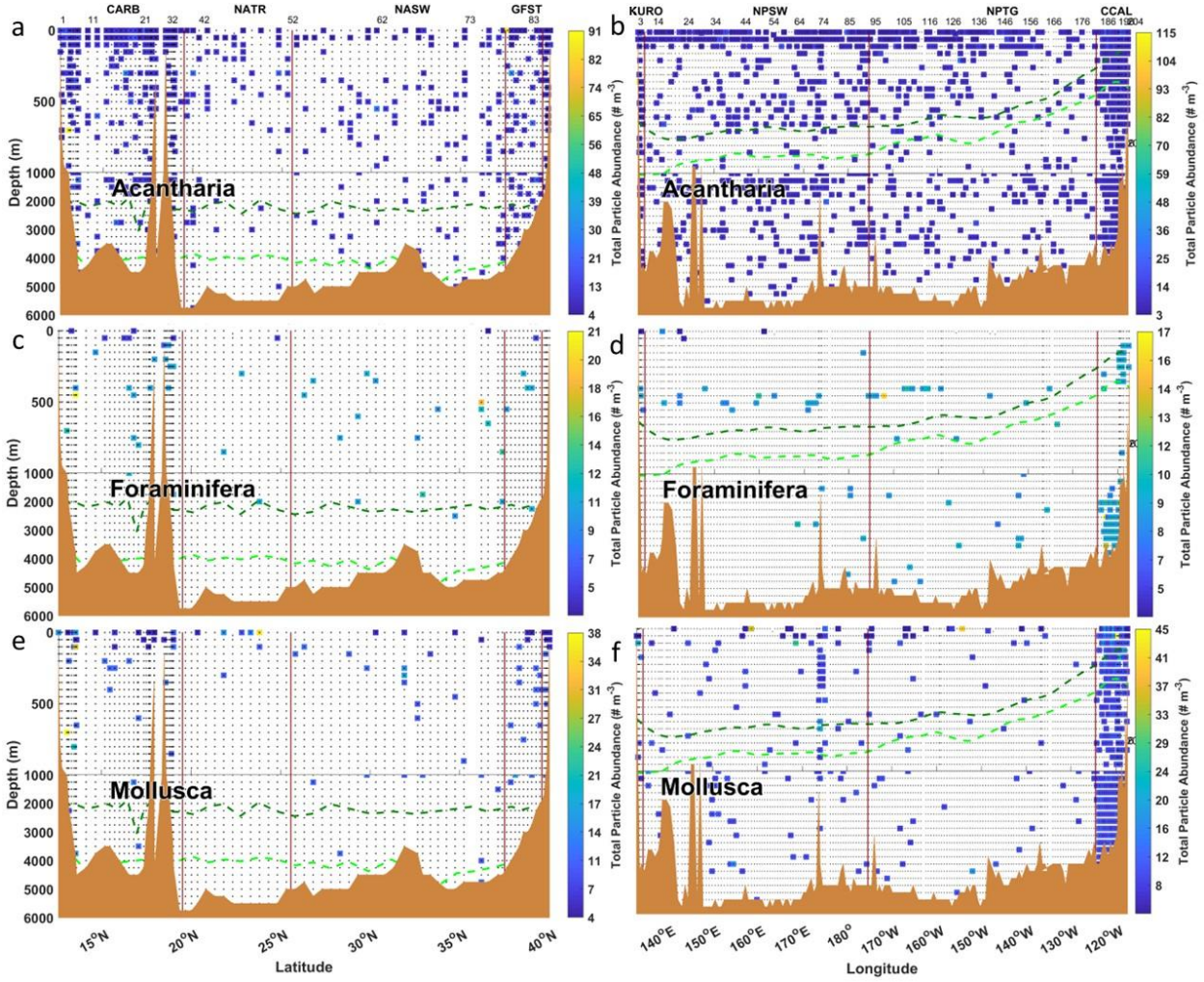

Figure 4.7: Spatial distribution of abundance of taxa sensitive to saturation state in the Atlantic and Pacific Oceans. Section plots of the abundance of living taxa over depth: (a and b) Acantharia, (c and d) Foraminifera, and (e and f) Mollusca. The Atlantic Ocean (A22) is shown in panels a, c, and e, and the Pacific Ocean (P02) in panels b, d, and f. Locations of depth bins (binned at 50 m resolution above 1000 m and 250 m resolution below 1000 m) sampled are labeled with a small black dot. Depth bins with at least one sample present are marked with a square colored by abundance. The Aragonite Saturation Horizon is shown in a dark green dashed line, and the Calcite Saturation Horizon is in a light green dashed line. The approximate locations of Biogeochemical Provinces are marked with vertical maroon lines and labeled on top See text for acronyms. Some station numbers are displayed on the top.

Nearly all the mollusks imaged were shelled pteropods, which have aragonite shells (Ramos-Silva et al., 2021). In the Atlantic Ocean, mollusks were present below the aragonite saturation

horizon but nearly absent below the calcite saturation horizon (Figure 4.7e). They peaked in abundance in the Caribbean Province from about 750 m to the aragonite saturation horizon, around 2000 m. A patch of high abundance was on the surface of the North Atlantic Tropical Gyral Province. Perhaps food availability below the calcite saturation horizon was too limited for them to be able to survive. Mollusks were more abundant in the Pacific and had a more varied distribution (Figure 4.7f). They were present with a patchy distribution at nearly all depths in every province. Mollusks were found consistently at all depths in the California Upwelling Coastal Province.

The California Upwelling Coastal Province has more observations at all depths of all three of these taxa, including acantharians, that supports the claim that more abundant food resources are required for these sensitive taxa to live in undersaturated conditions (Leung et al., 2019; Ramajo et al., 2016). Additionally, it is unlikely many of these imaged taxa are dead because these large, dense particles would have very fast sinking rates (500 – 3000 m day^{-1}) (Lalli & Gilmer, 1989; Walker et al., 2021) and be very unlikely to be sampled by the UVP due to this. Overall, the calcifying taxa abundances were generally higher and more likely to be distributed from the surface to the seafloor in the Pacific Ocean than in the Atlantic Ocean. In the Atlantic, our data suggest that the aragonite and calcite saturation horizons appeared to create a biophysical limitation on the distributions of calcifying organisms like foraminiferans and shelled pteropods. However, the calcifying taxa in the Pacific may be better adapted to lower saturation states because those conditions are so much more widespread in the Pacific than in the Atlantic. This conclusion is supported by one study that measured the impact of predicted pH and oxygen levels on several species of pteropods from the North Pacific and North Atlantic and found that only one species of pteropod was impacted by the combined predicted conditions and it was from the North Atlantic (Maas et al., 2016).

We expect that mean particle color will lighten as “hard parts,” including calcium carbonate, dissolve. In the Atlantic Ocean, detritus was darker at the surface and in the more coastal provinces (i.e., Caribbean and Gulf Stream Provinces) (Figure 4.8a). In the Pacific Ocean, fluffy aggregate mean grey level varied more by longitude than depth (Figure 4.8b). West of station 47 in the middle of the North Pacific Subtropical Gyre Province West, there were relatively darker fluffy aggregates. The California Upwelling Coastal Province also had darker fluffy aggregates at all depths.

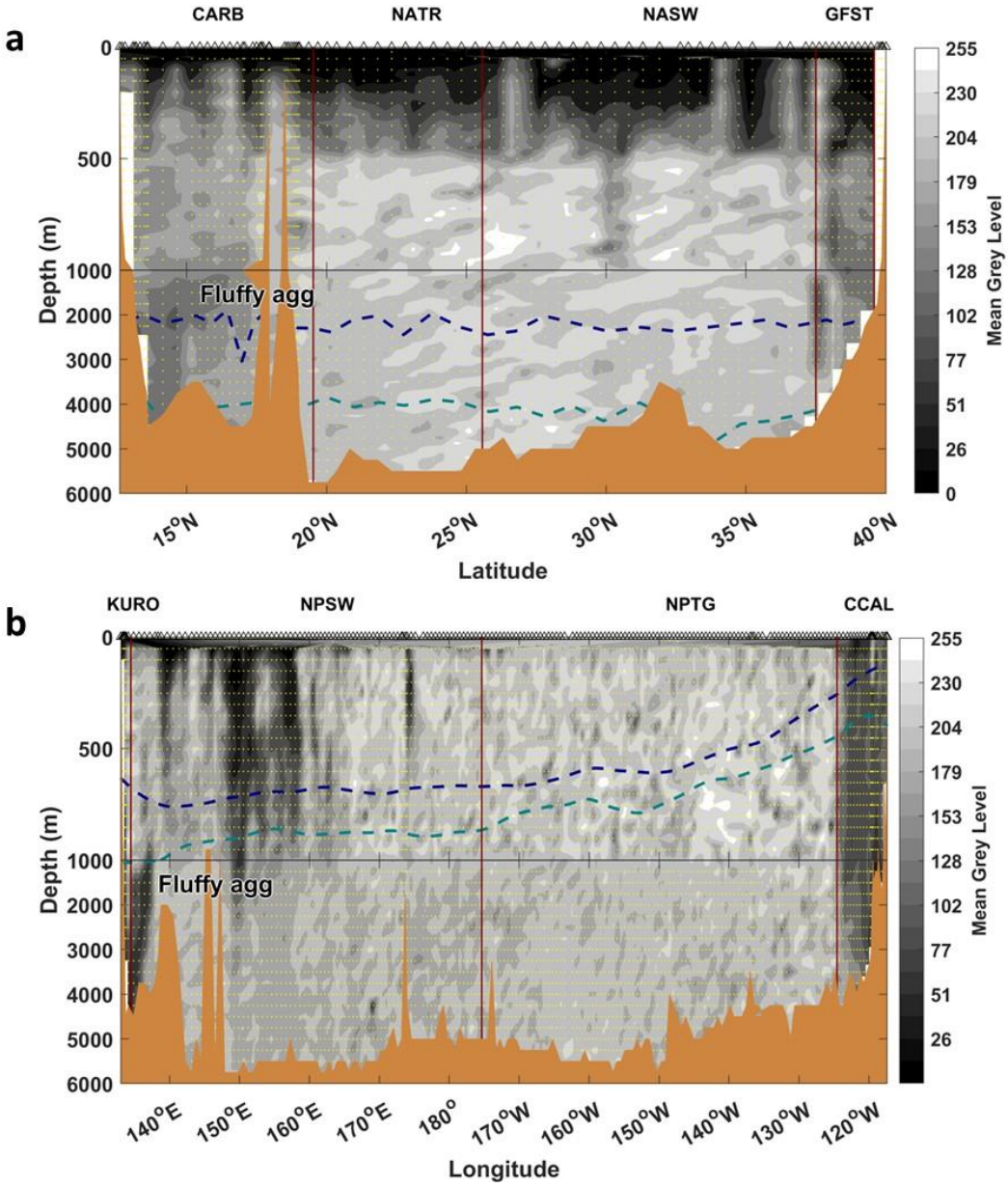

Figure 4.8: Impact of Saturation State on fluffy aggregate mean grey level in the Atlantic and Pacific Oceans. Section plots of the Mean Grey Level (from 0 to 255) of fluffy aggregates in the (a) Atlantic Ocean (A22) and (b) Pacific Ocean (P02). Locations of depth bins (binned at 50 m resolution above 1000 m and 250 m resolution below 1000 m) with at least one image in the particle category are labeled with a small yellow dot. The Aragonite Saturation Horizon is shown in a dark blue dashed line and the Calcite Saturation Horizon is shown in an aqua dashed line. The approximate locations of Biogeochemical Provinces are marked with vertical maroon or black lines and labeled on top. See text for acronyms. Locations of samples are marked on the top with black triangles.

To further investigate the relationship between aragonite saturation state and mean grey level of fluffy aggregates (Figures 4.9a – 4.9d), we performed linear regressions for different depth ranges in the Atlantic and Pacific Oceans, with results indicating that particles get lighter at lower saturation states. However, we would not expect the aragonite saturation state to affect the mean grey level of particles above the saturation horizon that is observed in both oceans (Figures 4.9a and 4.9c). We would only expect a causal relationship below the aragonite saturation horizon. This provides mixed evidence for our hypothesis that a lower saturation state will dissolve calcium carbonate parts in detrital particles, thereby lightening those particles' mean grey level. In the Atlantic, particles also get significantly smaller at lower saturation states (Figure 4.9b). Ignoring the relationship between water depth and saturation state, we would expect particles to be darker and larger at deeper depths because these particles are more likely to sink faster and be minerally ballasted. Despite this, we still see a significant relationship between these parameters and the saturation state that decreases with depth (Figures 4.2b and 4.2d). The adjusted r-squared value in the Atlantic Ocean is about 9% (Figure 4.9e) and only about 3% in the Pacific Ocean (Figure 4.9f). Dissolution cannot explain most of the variance in the mean grey level. This may be due to the prevalence of other mineral hard parts (e.g., silica) that would be unaffected by the carbonate saturation state (Taucher et al., 2022).

Biological controls on particle grey level are likely mixed; calcium carbonate hard parts are not remineralized readily by biology, but organic matter is remineralized as particles sink. Organic matter could be lighter than calcium carbonate hard parts, or it could be dense and dark as well. This dense dark organic matter is likely the most readily remineralized part of sinking particles. We are likely measuring both the biological removal of dark organic matter and the chemical weathering of dark parts calcium carbonate shells with our imaging. It should be noted that mineral hard parts can minerally ballast sinking particles and protect internal organic matter as they sink, likely leaving particles denser and darker as they sink to deeper depths (Armstrong et al., 2002). This method provides a framework to investigate the impact of various environmental factors on marine particle morphology. We may have some evidence that particles get lighter and smaller in corrosive conditions. However, other important factors that impact particle mean grey level remain unknown.

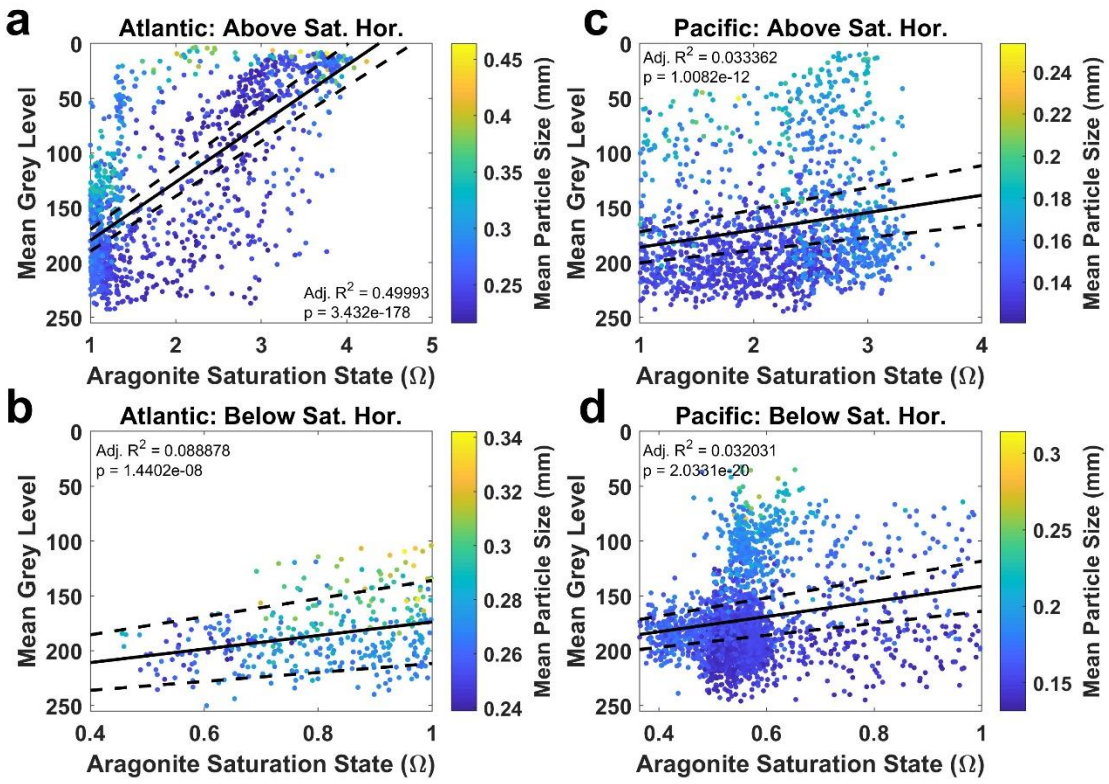

Figure 4.9: Effect of saturation state on fluffy aggregate morphology. Aragonite saturation state (in Ω) is plotted against Mean Grey Level (from 0 to 255) and colored by mean particle size (in mm) for fluffy aggregates in the Atlantic Ocean (a) above and (b) below the aragonite saturation horizon and in the Pacific Ocean (c) above and (d) below aragonite saturation horizon. Linear regression between aragonite saturation state and mean grey level is shown in the black line with the 95% confidence interval plotted as black dashed lines. The corresponding adjusted R-squared value (Adj. R2) and significance factor (p) are displayed within each panel.

4.5 Conclusion

This study is the first to describe the role of biogeochemical provinces and saturation states on marine particle morphology in the deep sea. Marine particles were larger, darker, and more abundant in coastal or westerly western boundary provinces, and living plankton were also more common there. A seamount reaching 2500 m at 174°E in the North Pacific Subtropical Gyre Province West was associated with elevated fluffy and dense aggregates, feces, crustacea, and rhizarians from the surface to the seafloor. The effect of bathymetry and seamounts on marine particle morphology has not been previously observed, though seamounts have been identified as biological hotspots (Dai et al., 2022). We found that marine particle communities are distinct in different biogeochemical provinces at all depths. We investigated the competing effects of depth and saturation state. We found that decreasing the saturation state correlated with lighter and

smaller fluffy aggregates even though darker (and thus denser) and bigger particles should be more likely to sink to deeper depths where saturation states are lower. We also found that the aragonite and calcite saturation horizons appear to exclude calcifiers from deep waters in the Atlantic Ocean but not the Pacific Ocean. Plankton in the Atlantic Ocean appear to be more sensitive to the saturation horizons of aragonite and calcite than in the Pacific, indicating that Pacific plankton are better adapted to low saturation states as this ocean has more prevalent low saturation state conditions. Marine particle morphology is an important factor to consider when measuring aspects of the biological carbon pump.

4.6 References

Almazán, E. T., Nuño, J. A. R., Aguilera, J. L. H., Gómez, M. A. M., Monter, E. C., Campos, E. D., Jiménez, R. M., Monreal, D. S., Contreras Tereza, V. K., Arenas Fuentes, V. E., & Salas de León, D. A. (2022). Historical observations of zooplankton groups in Mexican waters of the Gulf of Mexico and Caribbean Sea. Arabian Journal of Geosciences, 15, 1215. https://doi.org/10.1007/s12517-022-10481-z

Armstrong, R., Lee, C., Hedges, J., Honjo, S., & Wakeham, S. G. (2002). A new, mechanistic model for organic carbon fluxes in the ocean based on the quantitative association of POC with ballast minerals. Deep Sea Research II: Topical Studies in Oceanography, 49, 219–236. Retrieved from http://www.sciencedirect.com/science/article/pii/S0967064501001011

Baumgartner, M. F., & Tarrant, A. M. (2017). The physiology and ecology of diapause in marine copepods. Annual Review of Marine Science, 9(1), 387–411. https://doi.org/10.1146/annurev-marine-010816-060505

Beers, J. R., & Stewart, G. L. (1970). The preservation of acantharians in fixed plankton samples. Limnology and Oceanography, 15(5), 825–827. https://doi.org/10.4319/lo.1970.15.5.0825

Biard, T. (2022). Diversity and ecology of Radiolaria in modern oceans. Environmental Microbiology, 24(5), 2179–2200. https://doi.org/10.1111/1462-2920.16004

Biard, T., & Ohman, M. D. (2020). Vertical niche definition of test-bearing protists (Rhizaria) into the twilight zone revealed by in situ imaging. Limnology and Oceanography, 65(11), 2583–2602. https://doi.org/10.1002/lno.11472

Biard, T., Not, F., Hauss, H., Guidi, L., Gorsky, G., Vandromme, P., Hauss, H., Gorsky, G., Guidi, L., Kiko, R., & Not F. (2016). In situ imaging reveals the biomass of giant protists in the global ocean. Nature, 532(7600), 504–507. https://doi.org/10.1038/nature17652

Boyd, P. W., Claustre, H., Levy, M., Siegel, D. A., & Weber, T. (2019, April 18). Multi-faceted particle pumps drive carbon sequestration in the ocean. Nature. 568, 327–335. https://doi.org/10.1038/s41586-019-1098-2

Brass, G. W. (1980). Trace elements in acantharian skeletons. Limnology and Oceanography, 25(1), 146–149. https://doi.org/10.4319/lo.1980.25.1.0146

Brisbin, M. M., Mesrop, L. Y., Grossmann, M. M., & Mitarai, S. (2018). Intra-host symbiont diversity and extended symbiont maintenance in photosymbiotic Acantharea (clade F). Frontiers in Microbiology, 9, 1998. https://doi.org/10.3389/fmicb.2018.01998

Buesseler, K. O., Lamborg, C. H., Boyd, P. W., Lam, P. J., Trull, T. W., Bidigare, R. R., Bishop, J. K. B., Casciotti, K. L., Dehairs, F., Elskens, M., Honda, M., Karl, D. M., Siegel, D. A., Silver, M. W., Steinberg, D. K., Valdes, J., Van Mooy, B., & Wilson, S. (2007). Revisiting carbon flux through the ocean's twilight zone. Science, 316(5824), 567–570. https://doi.org/10.1126/science.1137959

Capone, D G, Zehr, J. P., Paerl, H. W., Bergman, B., & Carpenter, E. J. (1997). *Trichodesmium*, a globally significant marine cyanobacterium. Science, 276, 1221–1229. https://doi.org/10.1126/science.276.5316.1221

Capone, Douglas G., Burns, J. A., Montoya, J. P., Subramaniam, A., Mahaffey, C., Gunderson, T., Michaels, A. F., & Carpenter, E. J. (2005). Nitrogen fixation by *Trichodesmium* spp.: An important source of new nitrogen to the tropical and subtropical North Atlantic Ocean. Global Biogeochemical Cycles, 19(2), 1–17. https://doi.org/10.1029/2004GB002331

Chung, S.-N., Lee, K., Feely, R. A., Sabine, C. L., Millero, F. J., Wanninkhof, R., Bullister, J. L., Key, R. M., & Peng, T.-H. (2003). Calcium carbonate budget in the Atlantic Ocean based on water column inorganic carbon chemistry. Global Biogeochemical Cycles, 17(4), 1–16. https://doi.org/10.1029/2002gb002001

Clements, D. J., Yang, S., Weber, T., McDonnell, A. M. P., Kiko, R., Stemmann, L., & Bianchi, D. (2022). Constraining the particle size distribution of large marine particles in the global ocean with in situ optical observations and supervised learning. Global Biogeochemical Cycles, 36, e2021GB007276. https://doi.org/10.1029/2021GB007276

Conte, M. H., Ralph, N., & Ross, E. H. (2001). Seasonal and interannual variability in deep ocean particle fuxes at the Oceanic Flux Program (OFP)/Bermuda Atlantic Time Series (BATS) site in the western Sargasso Sea near Bermuda. Deep-Sea Research II: Topical Studies in Oceanography, 48, 1471–1505. https://doi.org/10.1016/S0967-0645(00)00150-8

Dai, S., Zhao, Y., Li, X., Wang, Z., Zhu, M., Liang, J., Lui, H., & Sun. X. (2022). Seamount effect on phytoplankton biomass and community above a deep seamount in the tropical western Pacific. Marine Pollution Bulletin, 175, 113354. https://doi.org/10.1016/j.marpolbul.2022.113354

Decelle, J., & Not, F. (2015). Acantharia. In Encyclopedia of Life Sciences (pp. 1–10). John Wiley and Sons, LTD. https://doi.org/10.1002/9780470015902.a0002102.pub2

Drago, L., Panaïotis, T., Irisson, J. O., Babin, M., Biard, T., Carlotti, F., Coppola, L., Guidi, L., Hauss H., Karp-Boss L., Lombard F., McDonnell A. M. P., Picheral M., Rogge A., Waite A. M., Stemmann L., Kiko R. (2022). Global distribution of zooplankton biomass estimated by in situ imaging and machine learning. Frontiers in Marine Science, 9, 894372. https://doi.org/10.3389/fmars.2022.894372

Dunne, J. P., Sarmiento, J. L., & Gnanadesikan, A. (2007). A synthesis of global particle export from the surface ocean and cycling through the ocean interior and on the seafloor. Global Biogeochemical Cycles, 21(4), 1–16. https://doi.org/10.1029/2006GB002907

England, M. H. (1995). The age of water and ventilation timescales in a global ocean model. Journal of Physical Oceanography, 25, 2756–2777. https://doi.org/10.1175/1520-0485(1995)025<2756:TAOWAV>2.0.CO;2

Feely, R. A., Sabine, C. L., Lee, K., Millero, F. J., Lamb, M. F., Greeley, D., Bullister, J. L., Key, R. M., Peng, T. H., Kozyr, A., Ono, T., & Wong, C. S. (2002). In situ calcium carbonate dissolution in the Pacific Ocean. Global Biogeochemical Cycles, 16(4), 91-1-91–12. https://doi.org/10.1029/2002gb001866

Finenko, Z. Z., Piontkovski, S. A., Williams, R., & Mishonov, A. V. (2003). Variability of phytoplankton and mesozooplankton biomass in the subtropical and tropical Atlantic Ocean. Marine Ecological Progress Series, 250, 125–144. https://doi.org/10.1016/S0967-0645(00)00181-8

Forget, M. H., Platt, T., Sathyendranath, S., & Fanning, P. (2011). Phytoplankton size structure, distribution, and primary production as the basis for trophic analysis of Caribbean ecosystems. ICES Journal of Marine Science, 68(4), 751–765. https://doi.org/10.1093/icesjms/fsq182

Gardner, W. D., Mishonov, A. V., & Richardson, M. J. (2018). Decadal comparisons of particulate matter in repeat transects in the Atlantic, Pacific, and Indian Ocean basins. Geophysical Research Letters, 45(1), 277–286. https://doi.org/10.1002/2017GL076571

Gardner, Wilford D., Jo Richardson, M., Mishonov, A. V., & Biscaye, P. E. (2018). Global comparison of benthic nepheloid layers based on 52 years of nephelometer and transmissometer measurements. Progress in Oceanography, 168(May), 100–111. https://doi.org/10.1016/j.pocean.2018.09.008

Geoffroy, M., Langbehn, T., Priou, P., Varpe, Ø., Johnsen, G., Le Bris, A., Fisher, J. A. D., Daase, M., McKee, D., Cohen, J., & Berge, J. (2021). Pelagic organisms avoid white, blue, and red artificial light from scientific instruments. Scientific Reports, 11, 14941. https://doi.org/10.1038/s41598-021-94355-6

Hasegawa, D. (2019). Island mass effect. In T. Nagai, H. Saito, K. Suzuki, & M. Takahashi (Eds.), Kuroshio Current, Physical, Biogeochemical and Ecosystem Dynamics (pp. 163–174). Hoboken: John Wiley & Sons. https://doi.org/10.1002/9781119428428.ch10

Haury, L., Fey, C., Newland, C., & Genin, A. (2000). Zooplankton distribution around four eastern North Pacific seamounts. Progress in Oceanography, 45, 69-105. https://doi.org/10.3389/fmars.2020.00416

Hemleben, C., Spindler, M., & Anderson, O. R. (1989). Modern Planktonic Foraminifera. New York, NY: Springer New York. https://doi.org/10.1007/978-1-4612-3544-6

Henson, S., Le Moigne, F., & Giering, S. (2019). Drivers of carbon export efficiency in the global ocean. Global Biogeochemical Cycles, 33(7), 891–903. https://doi.org/10.1029/2018GB006158

Henson, S. A., Sanders, R., Madsen, E., Morris, P. J., Le Moigne, F., & Quartly, G. D. (2011). A reduced estimate of the strength of the ocean's biological carbon pump. Geophysical Research Letters, 38(4), L04606. https://doi.org/10.1029/2011GL046735

Henson, S. A., Sanders, R., & Madsen, E. (2012). Global patterns in efficiency of particulate organic carbon export and transfer to the deep ocean. Global Biogeochemical Cycles, 26(1), 1–14. https://doi.org/10.1029/2011GB004099

Hogg, N. G., & Johns, W. E. (1995). Western boundary currents. Reviews of Geophysics, 33(2 S), 1311–1334. https://doi.org/10.1029/95RG00491

Huston, M. A., & Wolverton, S. (2009). The global distribution of net primary production: Resolving the paradox. Ecological Monographs, 79(3), 343–377. https://doi.org/10.1890/08-0588.1

Irisson, J.-O., Ayata, S.-D., Lindsay, D. J., Karp-Boss, L., & Stemmann, L. (2022). Machine learning for the study of plankton and marine snow from images. Annual Review of Marine Science, 14(1), 277–301. https://doi.org/10.1146/annurev-marine-041921-013023

Iversen, M. H. (2023). Carbon export in the ocean: A biologist's perspective. Annual Review of Marine Science, 15, 17.1-17.25. https://doi.org/10.1146/annurev-marine-032122

Iversen, M. H., & Lampitt, R. S. (2020). Size does not matter after all: No evidence for a size-sinking relationship for marine snow. Progress in Oceanography, 189, 102445. https://doi.org/10.1016/j.pocean.2020.102445

Jiang, X., Dong, C., Ji, Y., Wang, C., Shu, Y., Liu, L., & Ji, J. (2021). Influences of Deep-Water Seamounts on the Hydrodynamic Environment in the Northwestern Pacific Ocean. Journal of Geophysical Research: Oceans, 126(12). https://doi.org/10.1029/2021JC017396

Jorgensen, E. M., Hazen, E. L., Jacox, M. G., Pozo Buil, M., Schroeder, I., & Bograd, S. J. (2024). Physical and biogeochemical phenology of coastal upwelling in the California Current system. Geophysical Research Letters, 51(7). https://doi.org/10.1029/2024GL108194

Karl, D., Letelier, R., Tupas, L., Dore, J., Christian, J., & Hebel, D. (1997). The role of nitrogen fixation in biogeochemical cycling in the subtropical North Pacific Ocean. Nature, 388, 533–538. https://doi.org/10.1038/41474

Karl, D. M. (1999). A sea of change: Biogeochemical variability in the North Pacific subtropical gyre. Ecosystems, 2, 181–214. https://doi.org/10.1007/s100219900068

Karl, D. M., Letelier, R. M., Bidigare, R. R., Björkman, K. M., Church, M. J., Dore, J. E., & White, A. E. (2021). Seasonal-to-decadal scale variability in primary production and particulate matter export at Station ALOHA. Progress in Oceanography, 195, 102563. https://doi.org/10.1016/j.pocean.2021.102563

Kelly, T. B., Goericke, R., Kahru, M., Song, H., & Stukel, M. R. (2018). CCE II: Spatial and interannual variability in export efficiency and the biological pump in an eastern boundary current upwelling system with substantial lateral advection. Deep-Sea Research Part I: Oceanographic Research Papers, 140, 14–25. https://doi.org/10.1016/j.dsr.2018.08.007

Kodama, T., Watanabe, T., Taniuchi, Y., Kuwata, A., & Hasegawa, D. (2021). Micro-size plankton abundance and assemblages in the western North Pacific Subtropical Gyre under microscopic observation. PLoS ONE, 16(4), e0250604. https://doi.org/10.1371/journal.pone.0250604

Kwon, E. Y., Primeau, F., & Sarmiento, J. L. (2009). The impact of remineralization depth on the air–sea carbon balance. Nature Geoscience, 2(9), 630–635. https://doi.org/10.1038/ngeo612

De La Rocha, C. L., & Passow, U. (2007). Factors influencing the sinking of POC and the efficiency of the biological carbon pump. Deep-Sea Research Part II: Topical Studies in Oceanography, 54(5–7), 639–658. https://doi.org/10.1016/j.dsr2.2007.01.004

Lalli, C. M., & Gilmer, R. W. (1989). Pelagic Snails. Stanford: Stanford University Press.

Laufkötter, C., Vogt, M., Gruber, N., Aumont, O., Bopp, L., Doney, S. C., J. P. Dunne, J. Hauck, J. G. John, I. D. Lima, R. Seferian, and C. Völker. (2016). Projected decreases in future marine export production: The role of the carbon flux through the upper ocean ecosystem. Biogeosciences, 13(13), 4023–4047. https://doi.org/10.5194/bg-13-4023-2016

Leung, J. Y. S., Doubleday, Z. A., Nagelkerken, I., Chen, Y., Xie, Z., & Connell, S. D. (2019). How calorie-rich food could help marine calcifiers in a CO_2-rich future. Proceedings of the Royal Society B: Biological Sciences, 286(1906), 20190757. https://doi.org/10.1098/rspb.2019.0757

Leung, J. Y. S., Zhang, S. & Connell, S. D. (2022). Is Ocean Acidification Really a Threat to Marine Calcifiers? A Systematic Review and Meta-Analysis of 980+ Studies Spanning Two Decades. Small, 18, 2107407. https://doi.org/10.1002/smll.202107407

Lilley, M. K. S., Beggs, S. E., Doyle, T. K., Hobson, V. J., Stromberg, K. H. P., & Hays, G. C. (2011). Global patterns of epipelagic gelatinous zooplankton biomass. Marine Biology, 158(11), 2429–2436. https://doi.org/10.1007/s00227-011-1744-1

Lombard, F., Boss, E., Waite, A. M., Uitz, J., Stemmann, L., Sosik, H. M., Schultz, J., Romagnan, J. B., Picheral, M., Pearlman, J., Ohman, M. D., Niehoff, B., Möller, K. O., Miloslavich, P., Lara-Lpez, A., Kudela, R., Lopes, R. M., Kiko, R., Karp-Boss, L., Jaffe, J. S., Iversen, M. H., Irisson, J. O., Fennel, K., Hauss, H., Guidi, L., Gorsky, G., Giering, S. L. C., Gaube, P., Gallager, S., Dubelaar, G., Cowen, R. K., Carlotti, F., Briseño-Avena, C., Berline, L., Benoit-Bird, K., Bax, N., Batten, S., Ayata, S. D., Artigas, L. F., & Appeltans, W. (2019). Globally consistent quantitative observations of planktonic ecosystems. Frontiers in Marine Science, 6(196), 1-21. https://doi.org/10.3389/fmars.2019.00196

Longhurst, A. R. (2007). Toward an ecological geography of the sea. In Ecological Geography of the Sea (pp. 1–17). Elsevier. https://doi.org/10.1016/B978-012455521-1/50002-4

Lucas, C. H., Jones, D. O. B., Hollyhead, C. J., Condon, R. H., Duarte, C. M., Graham, W. M., Robinson, K. L., Pitt, K. A., Schildhauer, M., & Regetz, J. (2014). Gelatinous zooplankton biomass in the global oceans: Geographic variation and environmental drivers. Global Ecology and Biogeography, 23(7), 701–714. https://doi.org/10.1111/geb.12169

Maas, A. E., Lawson, G. L., & Wang, Z. A. (2016). The metabolic response of thecosome pteropods from the North Atlantic and North Pacific oceans to high CO_2 and low O_2. Biogeosciences, 13(22), 6191–6210. https://doi.org/10.5194/bg-13-6191-2016

Macdonald, A. (2022). Cruise Report of the 2022 P02W US GO-SHIP Reoccupation. (Release Draft 1). https://cchdo.ucsd.edu/data/35206/33RR20220430_do.pdf

Menezes, V. (2022). Cruise Report of the 2021 A22 US GO-SHIP Reoccupation. (Release Draft 1). https://cchdo.ucsd.edu/data/24670/325020210420_do.pdf

Le Moigne, F. A. C. (2019). Pathways of organic carbon downward transport by the oceanic biological carbon pump. Frontiers in Marine Science. 6, 634. https://doi.org/10.3389/fmars.2019.00634

Morrow, R. M., Ohman, M. D., Goericke, R., Kelly, T. B., Stephens, B. M., & Stukel, M. R. (2018). CCE V: Primary production, mesozooplankton grazing, and the biological pump in the California Current Ecosystem: Variability and response to El Niño. Deep-Sea Research Part I: Oceanographic Research Papers, 140, 52–62. https://doi.org/10.1016/j.dsr.2018.07.012

Mouw, C. B., & Yoder, J. A. (2005). Primary production calculations in the Mid-Atlantic Bight, including effects of phytoplankton community size structure. Limnology and Oceanography, 50(4), 1232–1243. https://doi.org/10.4319/lo.2005.50.4.1232

Nowicki, M., DeVries, T., & Siegel, D. A. (2022). Quantifying the carbon export and sequestration pathways of the ocean's biological carbon pump. Global Biogeochemical Cycles, 36(3), e2021GB007083. https://doi.org/10.1029/2021GB007083

O'Connor, J. M., Steinberger, B., Regelous, M., Koppers, A. A. P., Wijbrans, J. R., Haase, K. M., Stoffers, P., Jokat, W., & Garbe-Schönberg, D. (2013). Constraints on past plate and mantle motion from new ages for the Hawaiian-Emperor Seamount Chain. Geochemistry, Geophysics, Geosystems, 14(10), 4564–4584. https://doi.org/10.1002/ggge.20267

Ohman, M. D., & Browman, H. (2019). A sea of tentacles: Optically discernible traits resolved from planktonic organisms in situ. ICES Journal of Marine Science, 76(7), 1959–1972. https://doi.org/10.1093/icesjms/fsz184

Pansch, C., Schaub, I., Havenhand, J. & Wahl, M. (2014). Habitat traits and food availability determine the response of marine invertebrates to ocean acidification. Global Change Biology, 20, 765-777. https://doi.org/10.1111/gcb.12478

Picheral, M., Colin, S., & Irisson, J. (2017). EcoTaxa, a tool for the taxonomic classification of images. Retrieved from http://ecotaxa.obs-vlfr.fr

Picheral, M., Guidi, L., Stemmann, L., Karl, D. M., Iddaoud, G., & Gorsky, G. (2010). The underwater vision profiler 5: An advanced instrument for high spatial resolution studies of particle size spectra and zooplankton. Limnology and Oceanography: Methods, 8, 462–473. https://doi.org/10.4319/lom.2010.8.462

Pierrot, D., Lewis, E., & Wallace, D. (2006). MS Excel Program Developed for CO2 System Calculations. https://doi.org/10.3334/CDIAC/otg.CO2SYS_XLS_CDIAC105a

Ramajo, L., Pérez-León, E., Hendriks, I. E., Marbà, N., Krause-Jensen, D., Sejr, M. K., Blicher, M. E., Lagos, N. A., Olsen, Y. S., & Duarte, C. M. (2016). Food supply confers calcifiers resistance to ocean acidification. Scientific Reports, 6, 19374. https://doi.org/10.1038/srep19374

Ramos-Silva, P., Wall-Palmer, D., Marlétaz, F., Marin, F., & Peijnenburg, K. T. C. A. (2021). Evolution and biomineralization of pteropod shells. Journal of Structural Biology, 213(4), 107779. https://doi.org/10.1016/j.jsb.2021.107779

Reygondeau, G., Longhurst, A., Martinez, E., Beaugrand, G., Antoine, D., & Maury, O. (2013). Dynamic biogeochemical provinces in the global ocean. Global Biogeochemical Cycles, 27(4), 1046–1058. https://doi.org/10.1002/gbc.20089

Reygondeau, G., Guidi, L., Beaugrand, G., Henson, S. A., Koubbi, P., MacKenzie, B. R., Sutton, T. T., Fioroni, M., & Maury, O. (2018). Global biogeochemical provinces of the mesopelagic zone. Journal of Biogeography, 45(2), 500–514. https://doi.org/10.1111/jbi.13149

Romagnan, J. B., Aldamman, L., Gasparini, S., Nival, P., Aubert, A., Jamet, J. L., & Stemmann, L. (2016). High frequency mesozooplankton monitoring: Can imaging systems and automated sample analysis help us describe and interpret changes in zooplankton community composition and size structure – An example from a coastal site. Journal of Marine Systems, 162, 18–28. https://doi.org/10.1016/j.jmarsys.2016.03.013

Sarmiento, J. L., & Gruber, N. (2006). Ocean Biogeochemical Dynamics. Princeton University Press. Princeton, NJ: Princeton University Press. https://doi.org/10.1063/1.2754608

Schröder, S. M., Kiko, R., & Koch, R. (2020). Morphocluster: Efficient annotation of Plankton images by clustering. Sensors (Switzerland), 20(11), 1–26. https://doi.org/10.3390/s20113060

Sergi, S., Baudena, A., Cotté, C., Ardyna, M., Blain, S., & d'Ovidio, F. (2020). Interaction of the Antarctic Circumpolar Current with seamounts fuels moderate blooms but vast foraging grounds for multiple marine predators. Frontiers in Marine Science, 7, 416. https://doi.org/10.3389/fmars.2020.00416

Siegel, D. A., Buesseler, K. O., Doney, S. C., Sailley, S. F., Behrenfeld, M. J., & Boyd, P. W. (2014). Global assessment of ocean carbon export by combining satellite observations and food-web models. Global Biogeochemical Cycles, 28(3), 181–196. https://doi.org/10.1002/2013GB004743

Siegel, D. A., Devries, T., Doney, S. C., & Bell, T. (2021). Assessing the sequestration time scales of some ocean-based carbon dioxide reduction strategies. Environmental Research Letters, 16(10), 104003. https://doi.org/10.1088/1748-9326/ac0be0

Steinberg, D. K., & Landry, M. R. (2017). Zooplankton and the ocean carbon cycle. Annual Review of Marine Science, 9(1), 413–444. https://doi.org/10.1146/annurev-marine-010814-015924

Steinberg, D. K., Cope, J. S., Wilson, S. E., & Kobari, T. (2008). A comparison of mesopelagic mesozooplankton community structure in the subtropical and subarctic North Pacific Ocean. Deep-Sea Research Part II: Topical Studies in Oceanography, 55(14–15), 1615–1635. https://doi.org/10.1016/j.dsr2.2008.04.025

Sun, D., & Wang, C. (2017). Latitudinal distribution of zooplankton communities in the Western Pacific along 160°E during summer 2014. Journal of Marine Systems, 169, 52–60. https://doi.org/10.1016/j.jmarsys.2017.01.011

Sun, D., Zhang, D., Zhang, R., & Wang, C. (2019). Different vertical distribution of zooplankton community between North Pacific Subtropical Gyre and Western Pacific Warm Pool: its implication to carbon flux. Acta Oceanologica Sinica, 38(6), 32–45. https://doi.org/10.1007/s13131-018-1237-x

Sutton, T. T., Clark, M. R., Dunn, D. C., Halpin, P. N., Rogers, A. D., Guinotte, J., Bograd, S. J., Angel, M. V., Perez, J. a. A., Wishner, K., Haedrich, R. L., Lindsay, D. J., Drazen, J. C., Vereshchaka, A., Piatkowski, U., Morato, T., Błachowiak-Samołyk, K., Robison, B. H., Gjerde, K. M., Pierrot-Bults, A., Bernal, P., Reygondeau, G. & Heino, M. (2017) A global biogeographic classification of the mesopelagic zone. Deep-Sea Research Part I: Oceanographic Research Papers, 126, 85-102. http://doi.org/10.1016/j.dsr.2017.05.006

Talley, L., Pickard, G., Emery, W., & Swift, J. (2011). Dynamical processes for descriptive ocean circulation. In Descriptive Physical Oceanography (6th ed., pp. 187–243). Elsevier Ltd.

Talley, L. D. (2013). Closure of the global overturning circulation through the Indian, Pacific, and southern oceans. Oceanography, 26(1), 80–97. https://doi.org/10.5670/oceanog.2013.07

Taucher, J., Bach, L. T., Prowe, A. E. F., Boxhammer, T., Kvale, K., & Riebesell, U. (2022). Enhanced silica export in a future ocean triggers global diatom decline. Nature, 605(7911), 696–700. https://doi.org/10.1038/s41586-022-04687-0

Thomsen, J., Casties, I., Pansch, C., Körtzinger, A. & Melzner, F. (2013). Food availability outweighs ocean acidification effects in juvenile *Mytilus edulis*: laboratory and field experiments. Global Change Biology, 19, 1017-1027. https://doi.org/10.1111/gcb.12109

Thurnherr, A. (2022). Cruise Report of the 2022 P02E US GO-SHIP Reoccupation. https://cchdo.ucsd.edu/data/35209/33RR20220613_do.pdf

Todd, R., & Blackmon, P. (1956). Calcite and aragonite in Foraminifera. Journal of Paleontology, 30(1), 217–219. Retrieved from https://www.jstor.org/stable/1300395

Trudnowska, E., Lacour, L., Ardyna, M., Rogge, A., Irisson, J. O., Waite, A. M., Babin, M., & Stemmann, L. (2021). Marine snow morphology illuminates the evolution of phytoplankton blooms and determines their subsequent vertical export. Nature Communications, 12, 2816. https://doi.org/10.1038/s41467-021-22994-4

Turner, J. T. (2015). Zooplankton fecal pellets, marine snow, phytodetritus and the ocean's biological pump. Progress in Oceanography, 130, 205–248. https://doi.org/10.1016/j.pocean.2014.08.005

Walker, M., Hammel, J. U., Wilde, F., Hoehfurtner, T., Humphries, S., & Schuech, R. (2021). Estimation of sinking velocity using free-falling dynamically scaled models: Foraminifera as a test case. Journal of Experimental Biology, 224(2), 224. https://doi.org/10.1242/jeb.230961

Wiebe, P. H., Hulburt, E. M., Carpenter, E. J., E. Jahn, A., Knapp, G. P., Boyd, S. H., Ortner, P. B., & Cox, J. L. (1976). Gulf stream cold core rings: large-scale interaction sites for open ocean plankton communities. Deep Sea Research and Oceanographic Abstracts, 23(8), 695–710. https://doi.org/10.1016/s0011-7471(76)80015-0

Zhu, Y., Mulholland, M. R., Bernhardt, P. W., Neeley, A. R., Widner, B., Tapia, A. M., & Echevarria, M. A. (2024). Nitrogen uptake rates and phytoplankton composition across contrasting North Atlantic Ocean coastal regimes north and south of Cape Hatteras. Frontiers in Microbiology, 15, 1380179. https://doi.org/10.3389/fmicb.2024.1380179

Chapter 5: General Conclusions

Chapter 2 represents the first description of the biological carbon pump in the Northern Gulf of Alaska. I conclude that main driver of carbon flux in the Northern Gulf of Alaska during summer was aggregation processes and the main drivers of efficient carbon export were the proportion of chlorophyll-a in the large size fraction and aggregation processes. These results lead us to question our expectations about conditions and processes creating strong and efficient flux events. In Chapter 3, I show that particle morphology is essential for understanding the linkages and fate of carbon in the marine system. I captured detailed data on marine particle assemblages from both 'bloom' and 'non-bloom' conditions in the same regions of the Southern Ocean, suggesting different sources and fates of these particle types and different depth niches for morphologically distinct zooplankton predators. In Chapter 4, I found that decreasing the saturation state is associated with lighter and smaller detrital particles, even though darker (and thus denser) and bigger particles should be more likely to sink to deeper depths where saturation states are lower. Plankton and particles in the Atlantic Ocean appear to be more sensitive to the saturation horizons of aragonite and calcite than in the Pacific, indicating that Pacific plankton, living and dead, are better adapted to low saturation states as this ocean has more prevalent low saturation state conditions.

Overall, these results can help improve the global and regional climate and ecological models to better predict the fate of organic material produced through photosynthesis. This research can help better predict how the strength of carbon storage in the ocean may change with climate change, which is critical for climate modelers to predict the effects of climate change more accurately. This research highlights the importance of marine particle morphology as a factor to consider when measuring aspects of the biological carbon pump.

Appendix A: Supplemental Material for Chapter 2

This chapter has been published and is publicly available to download here: https://doi.org/10.1002/lno.12561. Supporting information, as cited in the chapter, is available in the same link.

Appendix B: Supplemental Material for Chapter 3

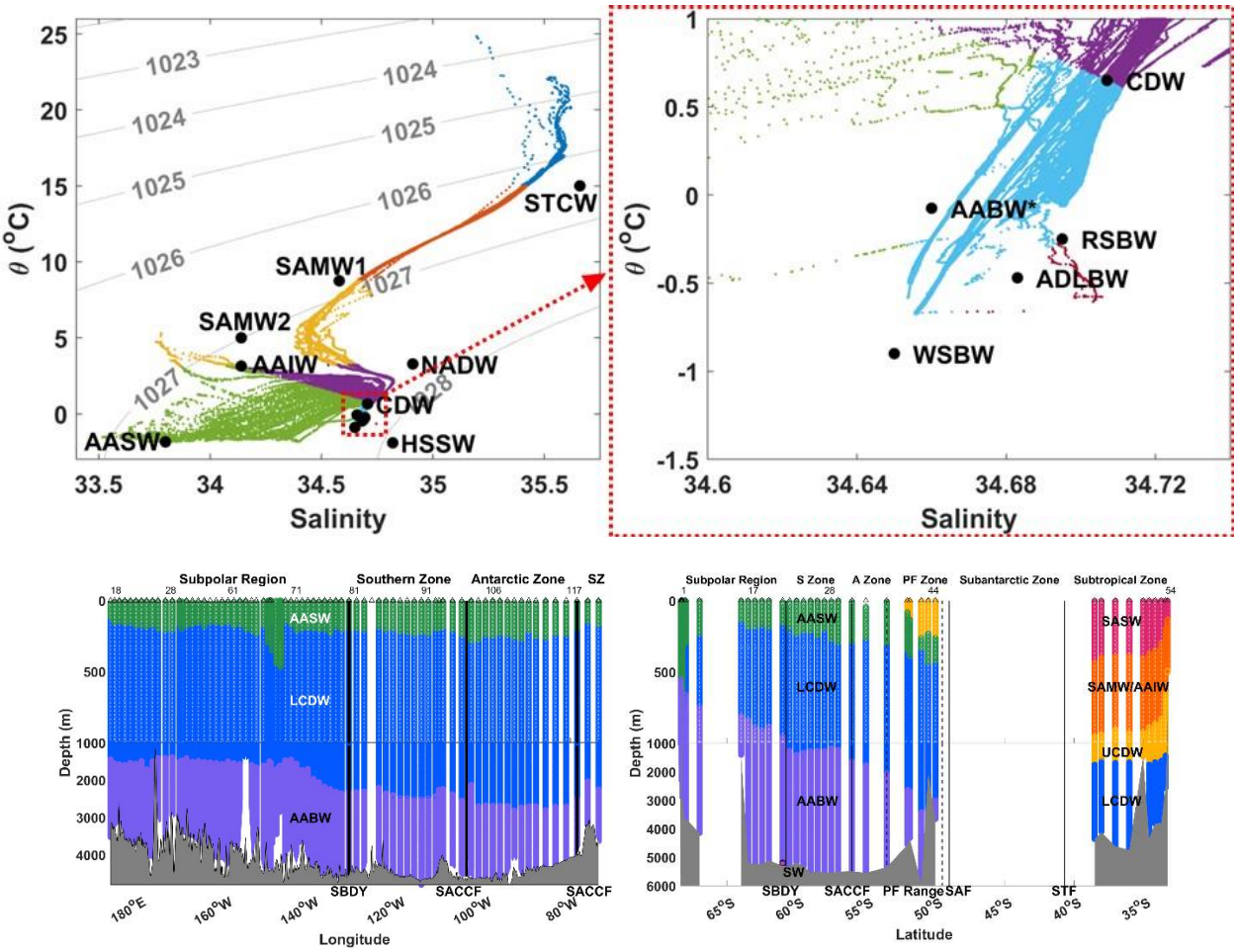

Figure B.1: Water mass delineations. (a) Water masses are characterized by Potential Temperature (theta) and Salinity with potential density contoured in dashed grey lines. Water mass endmembers are plotted and labeled in black. These water mass classifications are plotted over depth and space in (b) the Pacific sector and (c) the Indian sector of the Southern Ocean.

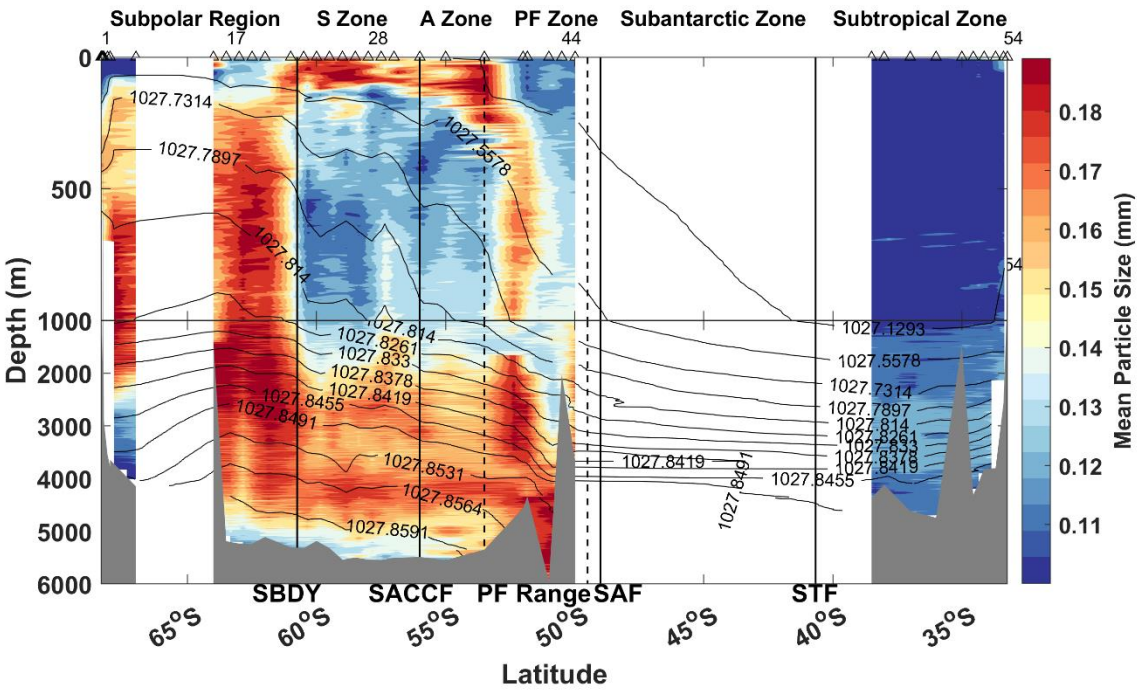

Figure B.2: Mean Particle Size in the African Sector. Section plot of mean particle size in mm for the African Sector cruise (I06S). Sigma-theta is shown in black contour lines on the lower panels. Climatological frontal regions are marked on the top: Subpolar Region; SZ/S Zone – Southern Zone; A Zone – Antarctic Zone; PF Zone – Polar Frontal Zone; Subantarctic Zone; and Subtropical Zone. Climatological frontal zones are marked with vertical black lines and labeled on the bottom: SB - Southern Boundary; SF - Southern Antarctic Circumpolar Current Front; PF - Polar Front; SAF – Subantarctic Front; STF – Subtropical Front.

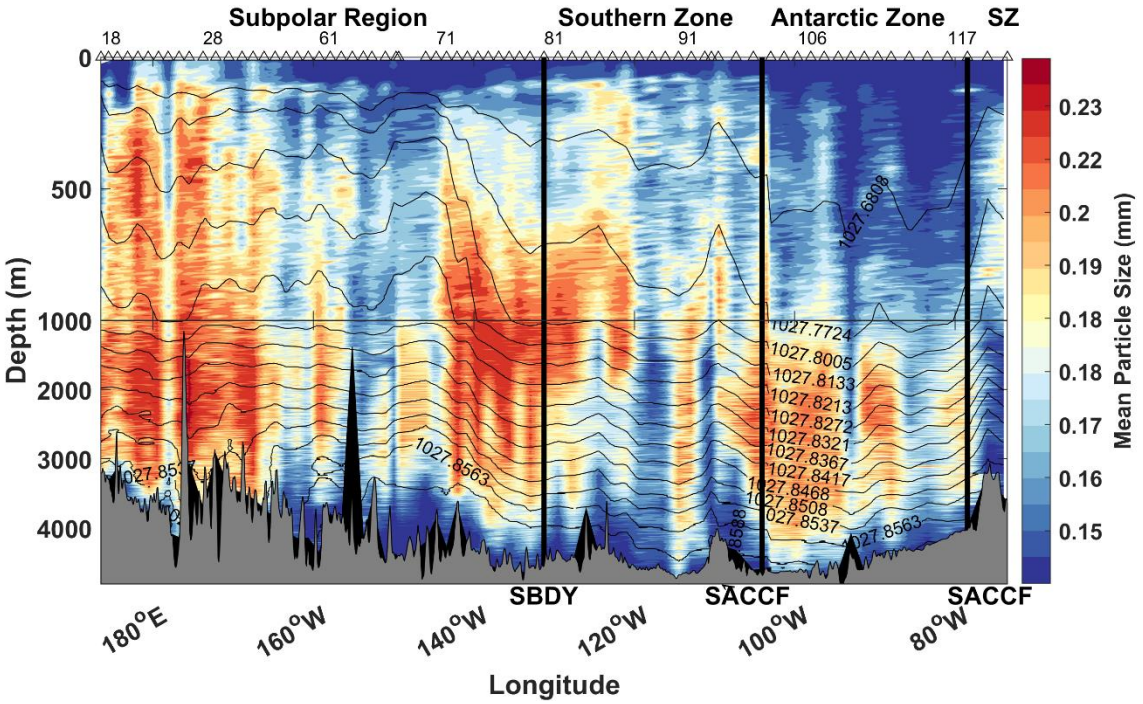

Figure B3: Mean Particle Size in the Pacific Sector. Section plot of mean particle size in mm for the Pacific Sector cruise (S04P). Sigma-theta is shown in black contour lines on the lower panels. Climatological frontal regions are marked on the top: Subpolar Region; SZ/S Zone – Southern Zone; A Zone – Antarctic Zone; PF Zone – Polar Frontal Zone; Subantarctic Zone; and Subtropical Zone. Climatological frontal zones are marked with vertical black lines and labeled on the bottom: SB - Southern Boundary; SF - Southern Antarctic Circumpolar Current Front; PF - Polar Front; SAF – Subantarctic Front; STF – Subtropical Front.

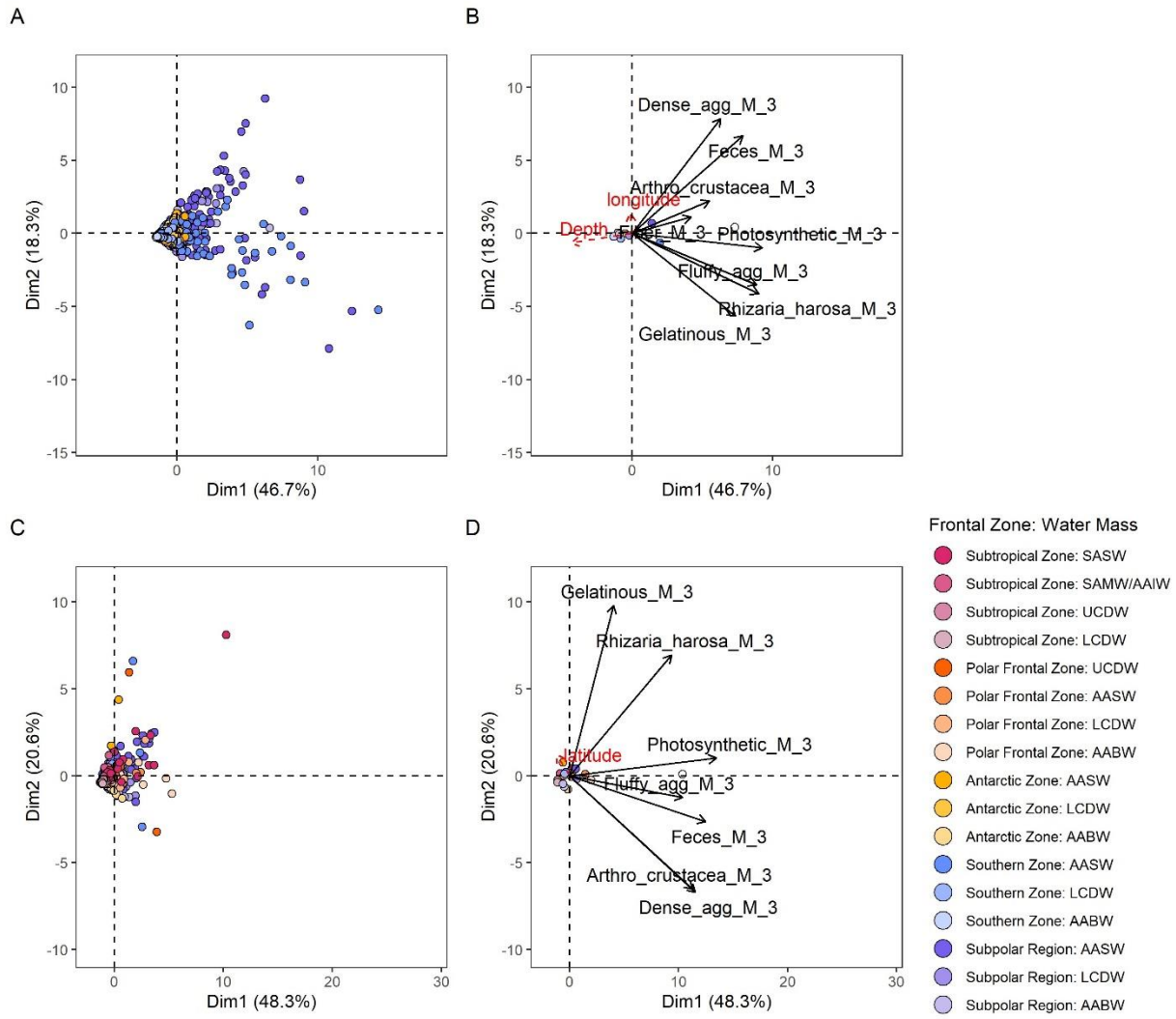

Figure B.4: Effect of fronts and water mass on marine particle communities. Principle components analysis (PCA) on the marine particle communities from each water mass/frontal zone pair in (a and b) the Pacific sector of the Southern Ocean (SO4P) and (c and d) the African sector of the Southern Ocean (IO6S). Each super-category of marine particles is shown in solid black lines. The mean of each marine particle community in each water mass/frontal zone pair, or the individuals, is shown in a colored circle. Quantitative supplementary variables are shown in a red dashed line. The mean marine particle community is shown as a circle colored by water mass. AASW- Antarctic Surface Water; LCDW - Lower Circumpolar Deep Water; AABW - Antarctic Bottom Water; SASW - Subantarctic Surface Water; SAMW - Subantarctic Mode Water; AAIW - Antarctic Intermediate Water; UCDW - Upper Circumpolar Deep Water.

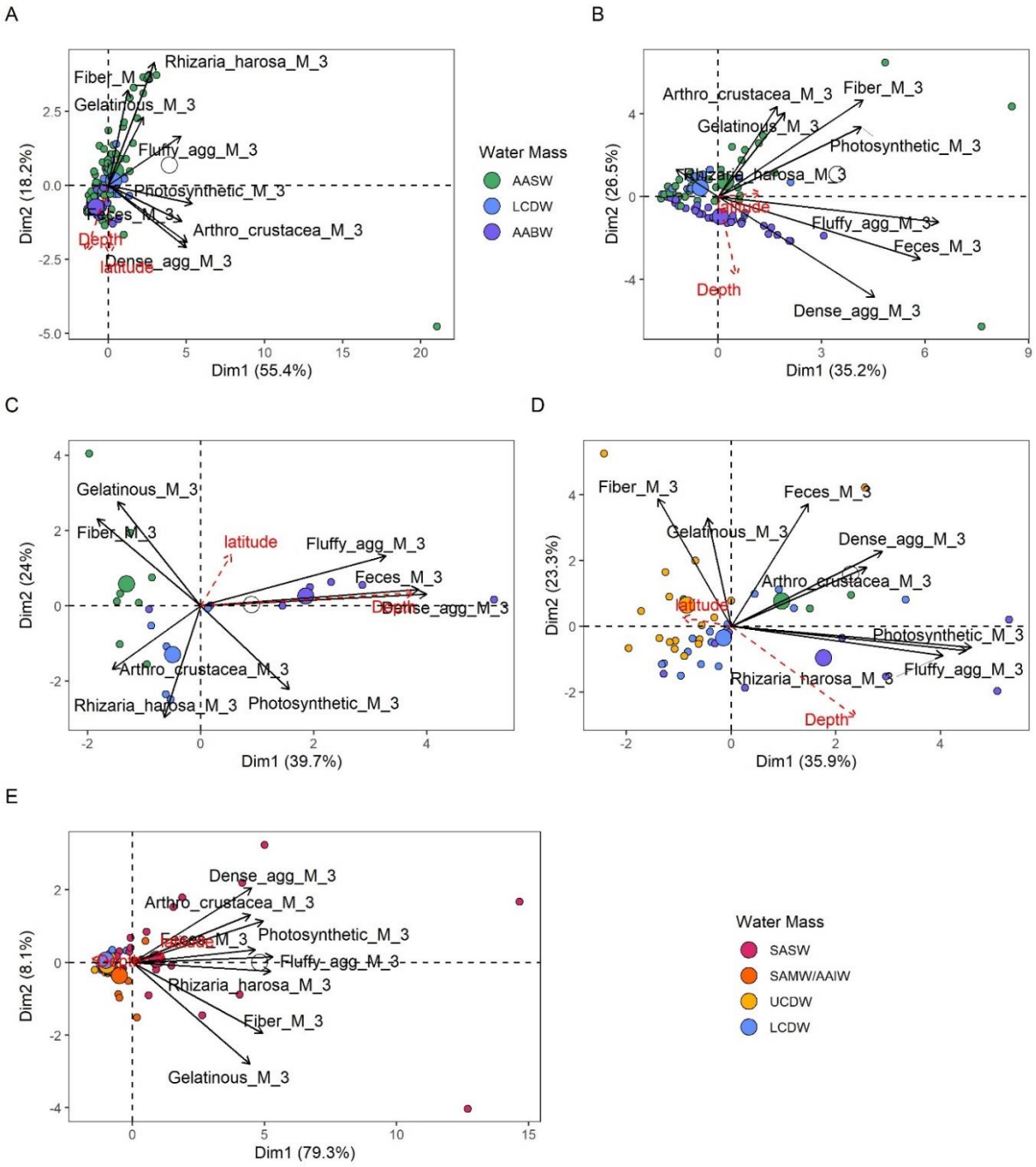

Figure B.5: Effect of water mass on marine particle communities within each frontal zone in the African Sector. (a) Subpolar Region, (b) Southern Zone, (c) Antarctic Zone, (d) Polar Frontal Zone, (e) Subtropical Zone. Each super-category of marine particles is shown in solid black lines. Quantitative supplementary variables are shown in a red dashed line. Individual marine particle communities are shown as small circles colored by water mass, with the mean of each marine particle community for each water mass in a large colored circle. AASW- Antarctic Surface Water; LCDW - Lower Circumpolar Deep Water; AABW - Antarctic Bottom Water; SASW - Subantarctic Surface Water; SAMW - Subantarctic Mode Water; AAIW - Antarctic Intermediate Water; UCDW - Upper Circumpolar Deep Water.

Table B.1: Particle categories.

Category Name	Super-category	# Validated	# Predicted	Total # Images	Percent Validated
'Crustacean'	Arthro_crustacea	2418	4711	7129	0.339178
'Eumalacostraca'	Arthro_crustacea	5	2	7	0.7142857
'Hyperia'	Arthro_crustacea	37	74	111	0.3333333
'like_Amphipoda'	Arthro_crustacea	62	131	193	0.3212435
'shrimp_like'	Arthro_crustacea	373	455	828	0.4504831
'Copepoda_Maxillopoda'	Arthro_crustacea	3314	7838	11152	0.2971664
'Eucalanidae'	Arthro_crustacea	4	6	10	0.4
'like_Copepoda'	Arthro_crustacea	846	2553	3399	0.2488967
'Ostracoda'	Arthro_crustacea	332	2573	2905	0.1142857
'badfocus_to_small_aggregates'	Bad_focus	95179	1986	97165	0.9795605
'badfocus_to_turbid'	Bad_focus	1809	564	2373	0.7623262
'mc_badfocus_aggregate_elongated'	Bad_focus	20064	1773	21837	0.9188075
'mc_badfocus_aggregate_fluffy'	Bad_focus	411553	961	412514	0.9976704
'mc_badfocus_aggregate_fluffy_to_badfocus_rhizaria'	Bad_focus	10114	273	10387	0.9737171
'mc_aggregate_dense_amorphous_to_detritus_dense_round'	Dense_agg	109120	2333	111453	0.9790674
'mc_aggregate_dense_dark_round_to_rhizaria'	Dense_agg	1501	3809	5310	0.2826742
'mc_aggregate_dense_elongated_to_aggregate_fluffy'	Dense_agg	15717	2470	18187	0.8641887
'mc_aggregate_dense_elongated_two_elements_to_bubbles'	Dense_agg	294	539	833	0.3529412
'mc_aggregate_dense_to_aggregate_fluffy_dark'	Dense_agg	253522	2937	256459	0.9885479
'mc_aggregate_dense_to_crustacea'	Dense_agg	2941	10971	13912	0.2114002
'mc_aggregate_dense_to_feces'	Dense_agg	16946	9724	26670	0.6353956
'mc_aggregate_dense_2_black_to_aggregate_fluffy_dark'	Dense_agg	1230	1437	2667	0.4611924
'feces_little_fluffy'	Feces	33114	597	33711	0.9822906
'mc_feces_bent_circular_fluffy'	Feces	738	1316	2054	0.3592989
'mc_feces_bent_thin'	Feces	6182	5033	11215	0.551226
'mc_feces_bent_to_crustacea'	Feces	4108	6393	10501	0.3912008
'mc_feces_dark_roundish'	Feces	89403	916	90319	0.9898582
'mc_feces_dark_small_irregular_shape'	Feces	139178	1905	141083	0.9864973
'mc_feces_short_straight'	Feces	20339	4773	25112	0.8099315
'mc_feces_small_round_grey'	Feces	3597	327	3924	0.9166667
'mc_feces_straight_to_feces_bent'	Feces	3832	895	4727	0.8106622
'mc_feces_straight_fluffy'	Feces	2576	8383	10959	0.2350579

'mc_feces_straight_fluffy_to_trichodesmium_tuff'	Feces	29720	948	30668	0.9690883
'mc_feces_straight_thin'	Feces	15589	1959	17548	0.8883633
'mc_feces_to_copepoda'	Feces	8633	3623	12256	0.7043897
'mc_feces_to_fiber'	Feces	4862	6533	11395	0.4266784
'mc_feces_straight_thin_to_fiber'	Feces	16637	2796	19433	0.856121
't006'	Feces	37	0	37	1
'mc_fiber_fluffy_to_feces'	Fiber	4339	2863	7202	0.6024715
'mc_fiber_thin_to_fiber_fluffy'	Fiber	16195	1989	18184	0.8906181
'mc_fiber_thin_straight'	Fiber	143289	856	144145	0.9940615
'mc_fiber_thin_straight_with_black_element'	Fiber	6461	3855	10316	0.6263086
'Phaeocystis'	Fluffy_agg	123983	23750	147733	0.839237
'mc_aggregate_fluffy'	Fluffy_agg	403127	35688	438815	0.9186719
'mc_aggregate_dark_round_to_puff'	Fluffy_agg	1318	510	1828	0.7210066
'mc_aggregate_fluffy_dark_to_aggregate_dense'	Fluffy_agg	131251	14040	145291	0.9033663
'mc_aggregate_fluffy_elongated'	Fluffy_agg	627048	4328	631376	0.9931451
'mc_aggregate_fluffy_elongated_to_aggregate_dense_elong'	Fluffy_agg	23311	5990	29301	0.7955701
'mc_aggregate_fluffy_grainy'	Fluffy_agg	15327	30050	45377	0.3377702
'mc_aggregate_fluffy_grainy_elongated'	Fluffy_agg	303033	16079	319112	0.9496133
'mc_aggregate_fluffy_grainy_to_aggregate_dense'	Fluffy_agg	518121	15258	533379	0.9713937
'mc_aggregate_fluffy_grey'	Fluffy_agg	112091	4893	116984	0.9581738
'mc_aggregate_fluffy_grey_elongated'	Fluffy_agg	11117	9602	20719	0.5365606
'mc_aggregate_fluffy_grey_to_aggregate_badfocus'	Fluffy_agg	779031	10191	789222	0.9870873
'mc_aggregate_fluffy_grey_to_rhizaria'	Fluffy_agg	3955	21758	25713	0.1538132
'house'	Gelatinous	105	385	490	0.2142857
'Doliolida'	Gelatinous	5	23	28	0.1785714
'Salpida'	Gelatinous	928	2074	3002	0.3091272
'Cnidaria_Metazoa'	Gelatinous	706	1701	2407	0.2933112
'Hydrozoa'	Gelatinous	585	1528	2113	0.2768575
'Siphonophorae'	Gelatinous	199	553	752	0.2646277
'Narcomedusae'	Gelatinous	28	30	58	0.4827586
'Solmundella_bitentaculata'	Gelatinous	18	70	88	0.2045455
'tentacle_Cnidaria'	Gelatinous	11673	8863	20536	0.5684164
'Ctenophora_Metazoa'	Gelatinous	137	247	384	0.3567708
't005'	Gelatinous	28	65	93	0.3010753
'Annelida'	Metazoa	123	225	348	0.3534483
'Polychaeta'	Metazoa	9	0	9	1

'Poeobius'	Metazoa	52	45	97	0.5360825
'Chaetognatha'	Metazoa	991	3145	4136	0.2396035
'Teleostei'	Metazoa	53	48	101	0.5247525
egg_Teleostei'	Metazoa	4	0	4	1
'fish_egg'	Metazoa	191	19	210	0.9095238
‘Appendicularia'	Metazoa	3	1	4	0.75
'Mollusca'	Metazoa	213	572	785	0.2713376
'Cephalopoda'	Metazoa	23	0	23	1
'bubble'	Not_relevant	1126	1304	2430	0.4633745
'not_relevant_duplicate'	Not_relevant	42940	522	43462	0.9879895
'like_Trichodesmium'	Photosynthetic	11551	2699	14250	0.8105965
'puff'	Photosynthetic	3010	6241	9251	0.3253702
'tuff'	Photosynthetic	7578	4910	12488	0.6068225
't020'	Photosynthetic	155	0	155	1
'Rhizaria'	Rhizaria_harosa	242	349	591	0.4094755
'Phaeodaria'	Rhizaria_harosa	23	21	44	0.5227273
'Castanellidae'	Rhizaria_harosa	17	25	42	0.4047619
'Circoporidae'	Rhizaria_harosa	30	0	30	1
'Tuscaroridae'	Rhizaria_harosa	19	16	35	0.5428571
'Aulacantha'	Rhizaria_harosa	4074	1181	5255	0.7752617
'Aulographis'	Rhizaria_harosa	17	8	25	0.68
'mc_aulacantha_to_foraminifera'	Rhizaria_harosa	34	5	39	0.8717949
'Coelodendrum'	Rhizaria_harosa	93	94	187	0.4973262
'Coelographis'	Rhizaria_harosa	128	180	308	0.4155844
'leg_Coelodendridae'	Rhizaria_harosa	117	215	332	0.3524096
'Medusettidae'	Rhizaria_harosa	102	733	835	0.1221557
'Aulosphaeridae'	Rhizaria_harosa	5057	3534	8591	0.5886393
'Aulatractus'	Rhizaria_harosa	28	8	36	0.7777778
'colonial_Aulosphaeridae'	Rhizaria_harosa	40	62	102	0.3921569
'mc_aulosphaeridae_to_cannosphaeridae'	Rhizaria_harosa	1899	2277	4176	0.4547414
'Cannosphaeridae'	Rhizaria_harosa	239	771	1010	0.2366337
'colonial_Cannosphaeridae'	Rhizaria_harosa	54	253	307	0.1758958
'unknown_Phaeodaria'	Rhizaria_harosa	282	1086	1368	0.2061404
'Acantharea'	Rhizaria_harosa	991	3334	4325	0.2291329
'Foraminifera'	Rhizaria_harosa	49	91	140	0.35
'Collodaria'	Rhizaria_harosa	1100	235	1335	0.82397
'colonial_Collodaria'	Rhizaria_harosa	157	261	418	0.3755981
'mc_solitary_black_to_puff'	Rhizaria_harosa	10670	4104	14774	0.7222147
'solitaryblack'	Rhizaria_harosa	11205	4325	15530	0.7215068
't001'		384	2237	2621	0.146509
't003'		51	0	51	1
Summary		**4668459**	**366892**	**5035351**	0.9271368

Appendix C: Supplemental Material for Chapter 4

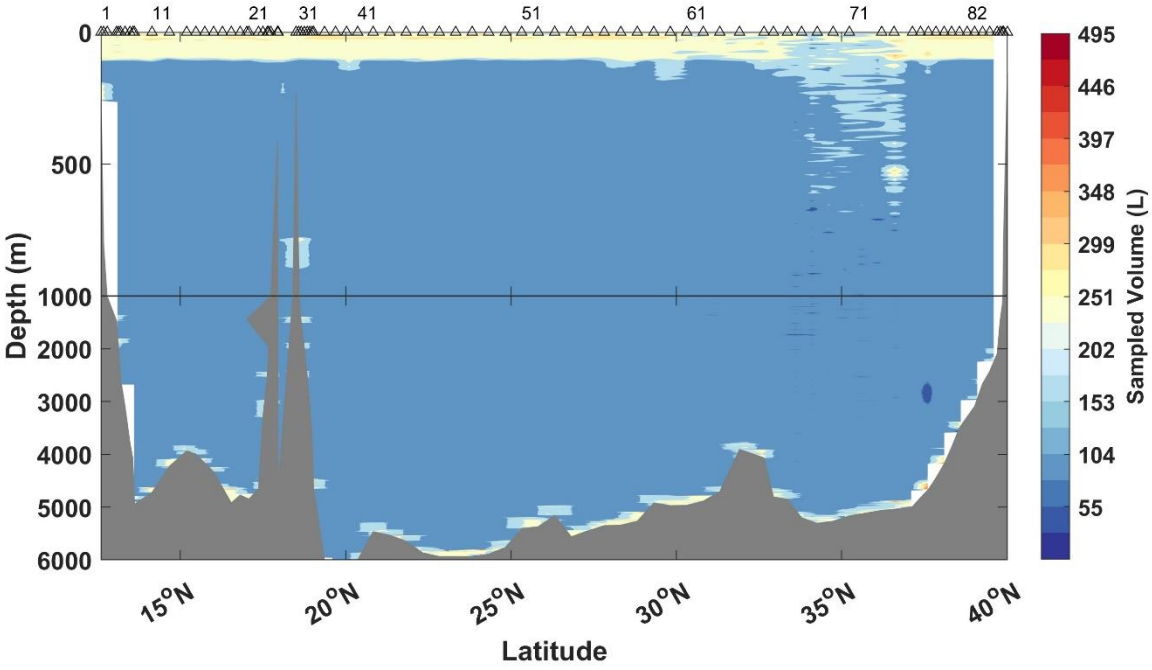

Figure C.1: Section plot of sampled volume in liters for the Atlantic Ocean cruise (A22). The volume of water sampled by the Under Water Vision profiler is displayed. The volume sampled is slightly higher in the upper 100m while the CTD rosette is lowered slower. The volume sampled is slightly higher close to the seafloor as the downcast speed is reduced to avoid a collision with the seafloor.